

CONFERENCE PROCEEDINGS

International Student Conference

“Science and Progress”

DAAD

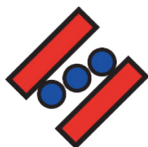


**Санкт-Петербургский
государственный
университет**

Freie Universität



Berlin



German-Russian
Interdisciplinary
Science Center

**St. Petersburg – Peterhof
November, 10-14
2014**

CONFERENCE PROCEEDINGS

International Student Conference “Science and Progress-2014”

SPb.: SOLO, 2014 – 116 pp.

Organizing committee

Prof. Dr. A.M. Shikin, G-RISC Coordinator, SPSU

E. Serova, G-RISC office, SPSU

T. Zaliutdinov, G-RISC office, SPSU

M. Rusinova, G-RISC office, SPSU

Program Committee

Prof. Dr. A.M. Shikin, G-RISC Coordinator, SPSU

Prof. Dr. E. Ruehl G-RISC Coordinator, Freie University Berlin

Dr. A.A. Manshina, Faculty of Chemistry, SPSU (Section A - Chemistry)

Prof. Dr. V.N. Troyan, Faculty of Physics, SPSU (Section B – Geo- and Astrophysics)

Prof. Dr. V.G. Nagnibeda, Faculty of Mathematics and Mechanics, SPSU (Section B – Geo- and Astrophysics)

Prof. Dr. S. Yu. Pelyugin, Faculty of Mathematics and Mechanics, SPSU (Section C – Mathematics and Mechanics)

Prof. Dr. A.P. Baraban, Faculty of Physics, SPSU (Section D – Solid State Physics)

Dr. A.S. Chirtsov, Faculty of Physics, SPSU (Section E – Applied Physics)

Prof. Dr. N.A. Timofeev, Faculty of Physics, SPSU (Section F – Optics and Spectroscopy)

Prof. Dr. Yu.M. Pismak, Faculty of Physics, SPSU (Section G – Theoretical, Mathematical and Computational Physics)

Prof. Dr. N.A. Kasyanenko, Faculty of Physics, SPSU (Section H - Biophysics)

Prof. Dr. V.I. Chizhik, Faculty of Physics, SPSU (Section I – Resonance Phenomena in Condensed Matter)

Contacts

Faculty of Physics, Saint-Petersburg State University

Ulyanovskaya ul. 1,

Peterhof, St. Petersburg, Russia

198504

Tel/Fax. +7 (812) 428-46-55

E-mail: g-risc@phys.spbu.ru

Website: www.g-risc.org

B.Geo- and Astrophysics

Gydra — GPU-based code for astrophysical SPH simulations

Korsunov Igor
elquendi@yandex.ru

Scientific supervisor: Prof. Dr. Kholtygin A.F., Department of Astronomy, Faculty of Mathematics and Mechanics, Saint-Petersburg State University

1 Motivation

Smooth Particle Hydrodynamics (SPH) [1, 2] is a numerical technique used in many fields of astrophysics [3], e.g., for a simulation of cosmological structure formation or star and planet formation. There are some widespread and mature program packages that use this technique for astrophysical simulations (e.g., GADGET [4, 5] and FI [6-9]). These packages are well developed, optimized and parallelized and could be run on a single machine as well as on a cluster of computers, but there is a area that still unemployed by such codes: computations with graphics processing units (GPUs).

Computational ability of the modern GPUs goes far beyond the processing of graphics to the field of general purpose computations. They could be used for speeding up many types of computations, providing that parallel algorithms exist for such computations. In astrophysics GPUs could be used, for example, for speeding up N-body and SPH simulations. While there are GPU-based N-body codes for astrophysics (e.g., PhiGRAPE [10], Octgrav [11] and Bonsai [12]), niche for astrophysical GPU-based SPH code is still vacant. We are presenting Gydra, our code (currently in development) that aims to fill this niche.

2 Method

2.1 Introduction to SPH

The idea behind SPH is relatively simple: take hydrodynamical equations, construct integral smoothed approximations of these equations (so called *kernel* approximations), construct discretized (or *particle*) approximations and solve derived equations (possibly, taking into account external forces like gas self-gravity or Lorentz force). Particle approximations should be reconstructed on every timestep.

For example, if we have function $f(\mathbf{x})$ representing some physical quantity at the position \mathbf{x} , kernel approximation of this function and its derivative would take the following form

$$f(\mathbf{x}) = \int_{\Omega} f(\mathbf{x}') W(\mathbf{x} - \mathbf{x}', h) d\mathbf{x}' \quad (1)$$

$$\nabla f(\mathbf{x}) = - \int_{\Omega} f(\mathbf{x}') \nabla W(\mathbf{x} - \mathbf{x}', h) d\mathbf{x}' \quad (2)$$

where $W(r,h)$ is a so called *smoothing function* or *kernel* (h is a parameter of this function, so called *smoothing length*). Smoothing should satisfy several properties, one of which is a compact support, i.e., smoothing function should drop to zero if $r > nh$, where n is a small number, usually around 2 or 3. This property essentially means that the state of particle is affected only by it's nearest neighbours.

One of the most widely used smoothing functions is a cubic spline of the following form:

$$W(r,h) = \alpha_d \begin{cases} \frac{2}{3} - \left(\frac{r}{h}\right)^2 + \frac{1}{2}\left(\frac{r}{h}\right)^3 & \text{if } 0 \leq \frac{r}{h} < 1, \\ \frac{1}{6}\left(2 - \frac{r}{h}\right)^3 & \text{if } 1 \leq \frac{r}{h} < 2 \end{cases} \quad (3)$$

Particle approximation of the f and it's derivative would take the following form:

$$f(x_i) = \sum_{j=1}^N \frac{m_j}{\rho_j} f(x_j) W_{ij} \quad (4)$$

$$\nabla f(x_i) = \sum_{j=1}^N \frac{m_j}{\rho_j} f(x_j) \nabla_i W_{ij} \quad (5)$$

where

$$W_{ij} = W(|x_i - x_j|, h) \quad (6)$$

$$\nabla_i W_{ij} = \frac{x_i - x_j}{r_{ij}} \frac{\partial W_{ij}}{\partial r_{ij}} \quad (7)$$

So, if we take Navier-Stokes equations in the following form

$$\begin{aligned} \frac{D\rho}{Dt} &= -\rho \nabla \cdot \mathbf{v} \\ \frac{Dv^\alpha}{Dt} &= \frac{1}{\rho} \frac{\partial \sigma^{\alpha\beta}}{\partial x^\beta} \\ \frac{De}{Dt} &= -\frac{p}{\rho} \frac{\partial v^\beta}{\partial x^\beta} + \frac{\mu}{2\rho} \epsilon^{\alpha\beta} \epsilon^{\alpha\beta} \end{aligned} \quad (8)$$

where $\sigma^{\alpha\beta}$ is a total stress, μ is a dynamic viscosity and $\epsilon^{\alpha\beta}$ is a strain rate, particle approximation would look like

$$\begin{aligned}
\frac{Dp_i}{Dt} &= -p_i \sum_{j=1}^N \frac{m_j}{\rho_j} v_j^\beta \frac{\partial W_{ij}}{\partial x_i^\beta} \\
\frac{Dv_i^\alpha}{Dt} &= \sum_{j=1}^N m_j \frac{\sigma_i^{\alpha\beta} + \sigma_j^{\alpha\beta}}{\rho_i \rho_j} \frac{\partial W_{ij}}{\partial x_i^\beta} \\
\frac{De_i}{Dt} &= \frac{1}{2} \sum_{j=1}^N m_j \frac{p_i + p_j}{\rho_i \rho_j} v_{ij}^\beta \frac{\partial W_{ij}}{\partial x_i^\beta} + \frac{\mu_i}{2\rho_i} \epsilon_i^{\alpha\beta} \epsilon_j^{\alpha\beta}
\end{aligned} \tag{9}$$

As can be seen, Navier-Stokes equations are turned from PDE to ODE and now could be easily solved using any numerical technique for ODE integration like leapfrog or Runge-Kutta methods

2.2 High-level algorithm

General outline of the Gydra's algorithm is following:

1. Construct octree from particle positions
2. Calculate gas self-gravity via Barnes-Hat algorithm [13]
3. Construct particle approximation of Navier-Stokes equations
4. Solve ODEs for one step
5. Adjust particle properties
6. Repeat

Octree is a spatial data structure that enables efficient queries for all particles in the given volume and for N nearest neighbours of the given particle. Octree allows us to utilize compact nature of SPH (due to the compact support of the smoothing function) and to replace summation by all particles in the discretized form of Navier-Stokes equations with summation by the particles inside support domain of the given particle.

3 Notes about implementation

3.1 Tools and technologies used

We choose to implement our code in NVidia CUDA for GPU part and C++ for host (CPU) part. Also we use some libraries like Thrust (collection of parallel algorithms for CPU and GPU) and Boost (collection of general purpose tools for C++).

Author believes that code without tests either broken right now or would be broken soon by future changes, so he uses Google Test and Google Mock frameworks for testing and tries to keep test coverage as high as reasonable.

3.2 Peculiarities of GPU programming

GPU programming model has some significant differences from the traditional CPU model. First of all, GPUs are massively parallel devices with the ability to run several thousands of threads simultaneously. Second important feature of GPU programming model is a separate memory of host (CPU) and device (GPU) and relatively low speed of host-to-device (and vice versa) memory transfers.

Therefore, in order to fully utilize computational power of GPUs, one should use parallel algorithms and data structure representations, even in the cases where serial implementations seems more natural. For example, natural algorithm for

octree are recursive serial procedure and natural representation of octree is also recursive (node with pointers to the child nodes/subtrees). But for GPU we should take another approach and construct pointerless representation of octree with the help of space-filling curves [14]. We also trying to keep the number of host-to-device and device-to-host memory transfers as low as possible, moving all significant computations to the GPU side.

4 Current status and conclusions

Currently, Gydra could not be called full-fledged SPH solver. Now we are working on the parallel octree construction [14] and there is a plenty of thing that should be done, like implementing parallel nearest neighbour search or parallel Barnes-Hut algorithm [12]. But the results obtained so far show that the idea of implementing SPH for GPU is reasonable and feasible task.

References

1. L.B. Lucy // *Astronomical Journal*, 82:1013–1024, December 1977.
2. 2.A. Gingold and J.J. Monaghan. // *Monthly Notices of the Royal Astronomical Society*, 181:375–389, November 1977.
3. Volker Springel. *Smoothed Particle Hydrodynamics in Astrophysics*. 2011, 0707.3168.
4. V. Springel, N. Yoshida, and S.D.M. White. // *New Astronomy*, 6:79–117, April 2001, astro-ph/0003162.
5. V. Springel // *Monthly Notices of the Royal Astronomical Society*, 364:1105–1134, December 2005, astro-ph/0505010.
6. L. Hernquist and N. Katz // *Astrophysical Journal, Supplement*, 70:419–446, June 1989.
7. J.P.E. Gerritsen and V. Icke // *Astronomy and Astrophysics*, 325:972–986, September 1997.
8. F.I. Pelupessy, P.P. van der Werf, and V. Icke // *Astronomy and Astrophysics*, 422:55–64, July 2004, astro-ph/0404163.
9. F.I. Pelupessy. *Numerical studies of the interstellar medium on galactic scales*. PhD thesis, Leiden Observatory, Leiden University, the Netherlands, 2005.
10. S. Harfst, A. Gualandris, D. Merritt, R. Spurzem, S. Portegies Zwart, and P. Berczik // *New astronomy*, 12:357–377, July 2007, astro-ph/0608125.
11. E. Gaburov, J. B’edorf, and S. Portegies Zwart // *Procedia Computer Science*, volume 1, p. 1119–1127, 1:1119–1127, May 2010, 1005.5384.
12. Jeroen B’edorf and Evghenii Gaburov and Simon Portegies Zwart // *Journal of Computational Physics*, 231(7):2825–2839, 2012.
13. J. Barnes and P. Hut // *Nature*, 324:446–449, December 1986.
14. Tero Karra s. *Maximizing Parallelism in the Construction of BVHs, Octrees, and k-d Trees*. *High Performance Graphics 2012*, 2012.

Photometry and polarimetry of supernovae performed on telescopes LX200 and AZT-8

Mokrushina Anna
hobbitenka1608@rambler.ru

Scientific supervisor: Dr. Larionov V.M., Department of Astrophysics, Saint-Petersburg State University; The Central (Pulkovo) Astronomical Observatory of the Russian Academy of Sciences

Introduction

Supernovae are an important object of research, because in the process of thermonuclear synthesis they form the diversity of the chemical elements that make up the rest of the objects in the universe. Their study helps to understand better the evolution of matter in the universe. The relevance of the study of these objects supports the recent discovery of the accelerated expansion of the universe, made as a result of the study of supernovae.

Two supernovae, 2013ej (type IIP) and 2014J (type Ia), were taken for present work. Observations, processing and analysis of the data obtained were made of these supernovae. As a result of observations there were made plots the light curves, the analysis of which allowed to calculate the following physical parameters: bolometric luminosity, bolometric correction, the mass ejected in the explosion of a nickel, the explosion energy, the mass of the ejected shell radius of the star - the progenitor, the temperature distribution and the radius of the photosphere, depending on the time, estimate of the distance to the supernova. Both supernovae have shown a fairly high degree of polarization, which may indicate a large asymmetry of the explosion.

Results and Discussion

Observational data were obtained, employing two telescopes: LX200 and AZT-8. LX200 (D = 0.4 m, F = 4064 mm, field of view: 14.3' x 9.5', optical scheme is Schmidt-Cassegrain) is located at St. Petersburg State University, in Peterhof, 50 m above sea level. AZT-8 (D = 0.7 m, F = 2820 mm, field of view: 8.1' x 5.4', camera is situated in the main focus of a parabolic mirror) is located at the Crimean Astrophysical Observatory, in settlement Nauchny, 600 m above sea level.

Observations were carried out using identical CCD cameras ST-7 XME equipped with CCDs based on the crystal KAF-0402ME. Its sensitivity maximum is near the line H α . Dimensions of the matrix is 765 x 510 pixels (pixel size is 9 x 9 mkm). For polarimetric observations used two plates Savar.

Photometry of summed frames was made at package PHOT. This package was developed by Larionov V.M. based program SExtractor (author E. Bertin).

SN2013ej

Supernova 2013ej flushed on July 25 in the galaxy M 74 with the following coordinates: R.A. = 01^h36^m48^s.16, Decl. = +15^o45'31".0.

After the data processing the light curve in four filters (B,V,R,I) was constructed. It is shown in Fig. 1(a) with color dots. Black dots denote the data from the article [1].

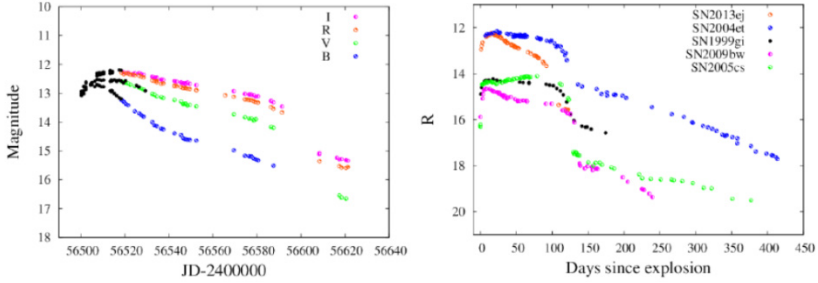


Fig. 1. a) Light curve of SN2013ej in four filters; b) Light curves of type IIP supernovae in the filter R.

As seen from the figure, colored and black dots are in good agreement with each other. Fig. 1(b) shows a comparison of the light curves in the filter R of studied supernova and other supernovae of the same type. As typical for type II supernovae, the forms of light curves are markedly different from each other. The plateau phase of SN2013ej ends much earlier than other supernovae. It is usually associated with a relatively small size of the progenitor star [1].

Bolometric light curve (Fig. 2a) was constructed [2]. It characterized the total radiation of the star at all of the bands with the absorption, also was calculated the bolometric correction $BC \approx -1.92 \pm 0.13$ mag.

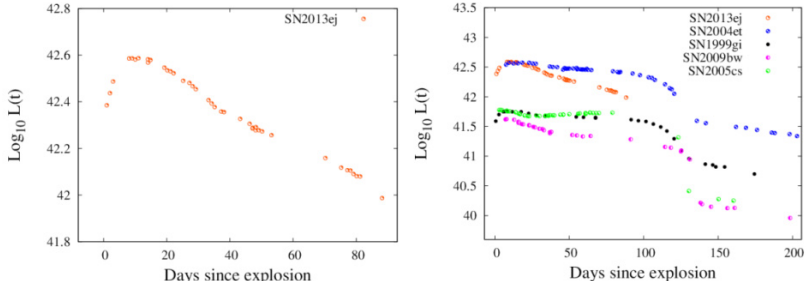


Fig. 2. a) The bolometric light curve of SN2013ej; b) A comparison of bolometric curves SN2013ej with other supernovae of the same type.

The bolometric luminosity peak of SN2013ej reached on the 11th day after the explosion, $L_{bol} = 10^{42.59 \pm 0.05}$ erg/s (which is typical for SNe IIP [2]).

The ^{56}Ni mass ejected in the explosion was calculated, $M(^{56}\text{Ni}) = 0.041 \pm 0.001 M_{\odot}$. For SN2004et $M(^{56}\text{Ni}) = 0.057 \pm 0.03 M_{\odot}$ [2].

Estimation of the energy of the explosion was found as $E = 1.15 \pm 0.4 \times 10^{51}$ erg, also estimation of the mass of the ejected shell in the explosion, $M = 13.96 \pm 4.47 M_{\odot}$, and radius of the progenitor star, $R = 164 \pm 34 R_{\odot}$. The method is described in article [3].

Changes of temperature and photosphere radius were calculated (Fig. 3).

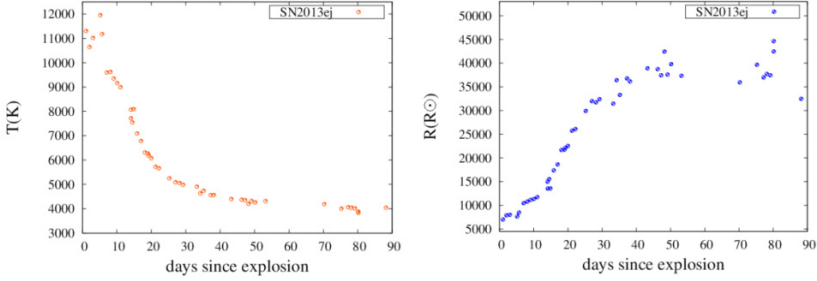


Fig. 3. a) Temperature change of SN2013ej; b) Photosphere radius change of SN2013ej.

Distance to the supernovae was calculated by the method proposed in [4]. $D = 9.77 \pm 0.88$ Mpc.

Results of polarimetric data processing are shown in Fig. 4.

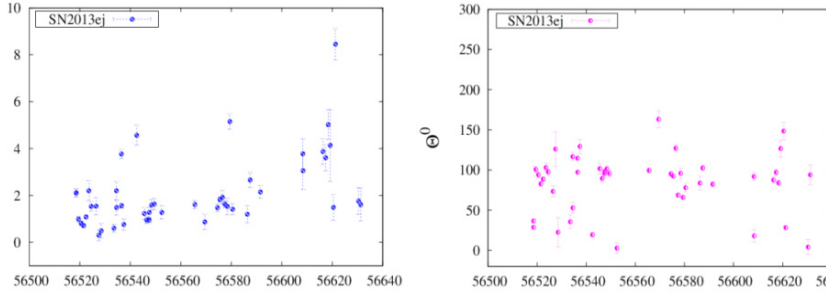


Fig. 4. The polarization parameters for SN2013ej: a) The degree of polarization; b) Direction of preferred oscillations of the electric vector.

To the emergence of polarization can lead non-sphericity [6] and large emissions of matter overlapping from us scatter electrons, as well as radiation scattering by inhomogeneities of previously discarded the shells.

SN2014J

Supernova 2014J flushed on January 16 in the galaxy M 82 with the following coordinates: R.A. = $09^h55^m42^s.14$, Decl. = $+69^{\circ}40'26''.0$.

Light curve in four filters is shown in Fig. 5.

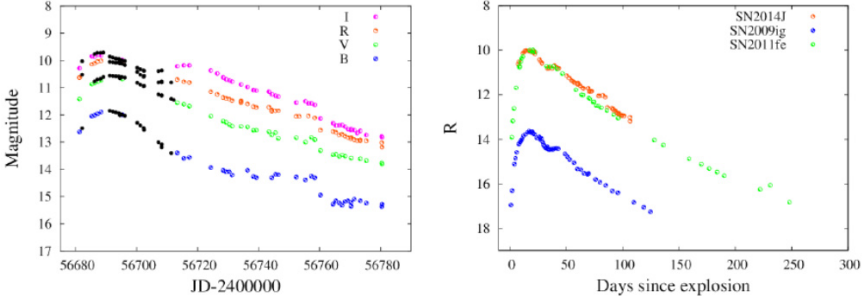


Fig. 5. a) Light curve of SN2014J in four filters; b) Light curves of Ia SNe in filter R.

Similar to the previous SN, processing results and data from the article [7] are shown with color and black dots, respectively. Very good agreement between these data is observed again. SN2014J has a typical light curve of type Ia.

Bolometric correction for this SN was found $BC \approx -1.79 \pm 0.31$ mag. Bolometric light curve is shown in Fig. 6.

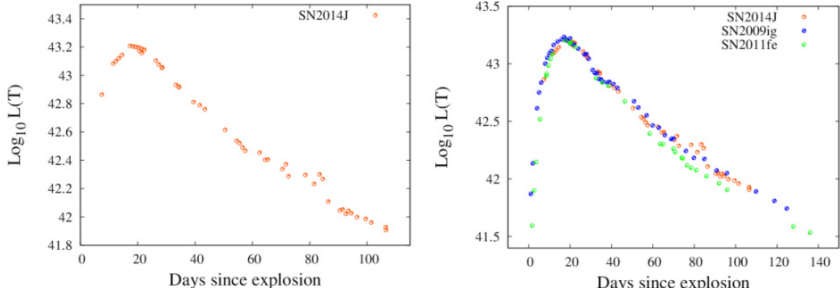


Fig. 6. a) Bolometric light curve of SN2014J; b) Comparison of bolometric light curves SN2014J and other SNe of the same type.

Maximum of Bolometric luminosity reached on the $\sim 17^{\text{th}}$ day, $\text{Lg}L(t) = 43.24 \pm 0.12$ erg/s, which is typical for SNe Ia.

Dependence of temperature from time (Fig. 7a) and the change of photosphere radius (Fig. 7b) were estimated.

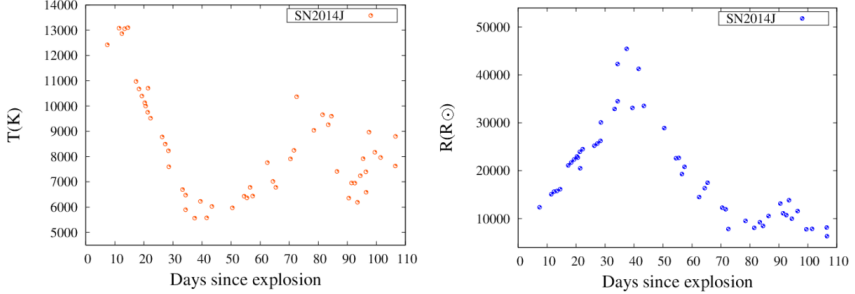


Fig. 7. a) Temperature change of SN2014J; b) Photosphere radius change of SN2014J.

Estimation of the distance to the photometric formula [5] showed the result $D = 3.83 \pm 1.15$ Mpc. Distance to the galaxy M82 in the database NED is 3.777 Mpc.

Ia supernovae in most cases have a small polarization. Polarization of SN2014J was much greater than the average values for other SNe, it reaches 6-7% at the maximum (Fig. 8a).

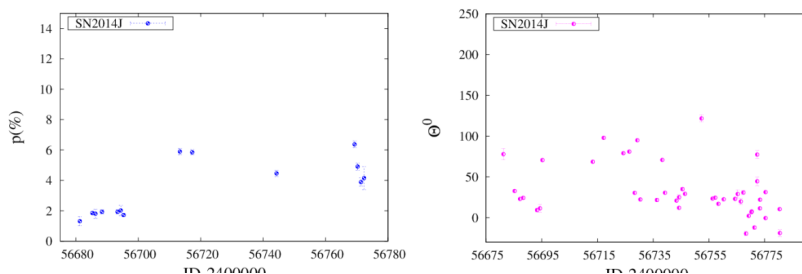


Fig. 8. The polarization parameters for SN2014J: a) The degree of polarization; b) Direction of preferred oscillations of the electric vector.

A large degree of polarization indicates a large asymmetry and heterogeneity of the structure of the inner layers.

Conclusion

Observational data on SN2013ej and SN2014J have been received, processed and analyzed. Processing showed results consistent with those data obtained earlier for other SNe. Data analysis made it possible to determine the following physical parameters of SNe:

For the SN2013ej: $L_{bol}(\max) = 10^{42.59 \pm 0.05}$ erg/s, $BC \approx -1.92 \pm 0.13$ mag, $M(^{56}\text{Ni}) = 0.041 \pm 0.001 M_{\odot}$, Energy of the explosion = $1.15 \pm 0.4 \times 10^{51}$ erg, Mass of the ejected shell = $13.96 \pm 4.47 M_{\odot}$, Radius of the progenitor star = $164 \pm 34 R_{\odot}$, Distance to the SN = 9.77 ± 0.88 Mpc. Distribution of temperature and photosphere radius versus time was obtained.

For the SN2014J: $L_{bol}(\max) = 10^{43.24 \pm 0.12}$ erg/s, $BC \approx -1.79 \pm 0.31$ mag, $D = 3.83 \pm 1.15$ Mpc. Distribution of temperature and photosphere radius versus time was obtained.

Both supernovae showed a fairly high degree of polarization. This may indicate a large asymmetry of explosion [6].

References

1. Valenti S. // Monthly Notices of the Royal Astr. Society: Letters, 1:101-105 (2013).
2. K. Maguire, E. Di Carlo // Notices of the Royal Astronomical Society, 2:981-1004 (2010).
3. Litvinova I.Yu., Nadezhin D.K. // Soviet Astronomy Letters, 11:145-147 (1985).
4. Mario Hamuy. // The Astrophysical Journal, 2:63-65 (2002).
5. Pskovsky Y.P. New and Supernovae.- Moscow, Science, 1985.
6. D. Andrew Howell, Peter Hoflich // The Astrophysical Journal, v.556, 1:302-321 (2001).
7. Tsvetkov D.Yu. // Contrib. Astron. Obs. Skalnat'e Pleso, 43:94-109 (2013).

Correlation of radial fluctuations in deep galaxy redshift surveys

Shirokov Stanislav
arhath.sis@yandex.ru

*Scientific supervisor: Dr. Baryshev Yu. V., Department of Astronomy,
Faculty of Mathematics & Mechanics, Saint-Petersburg State
University*

Introduction

One of the most important problems in modern observational cosmology is to determine the maximal size of large-scale inhomogeneities in distribution of galaxies in the Universe. As it is known the Sloan Digital Sky Survey shows that at small redshifts there are inhomogeneous structures, for example, Sloan Great Wall with a size of 400 Mpc/h. Today the background exists that there are similar and larger structures at large redshifts. In addition, if we really see inhomogeneous structures at large redshifts then there should be correlation of these structures between independent surveys of different research groups. For these purposes a comparison of radial fluctuations in two deep galaxy redshift surveys (COSMOS [1] and UVISTA [2]) that are belong to one field is considered.

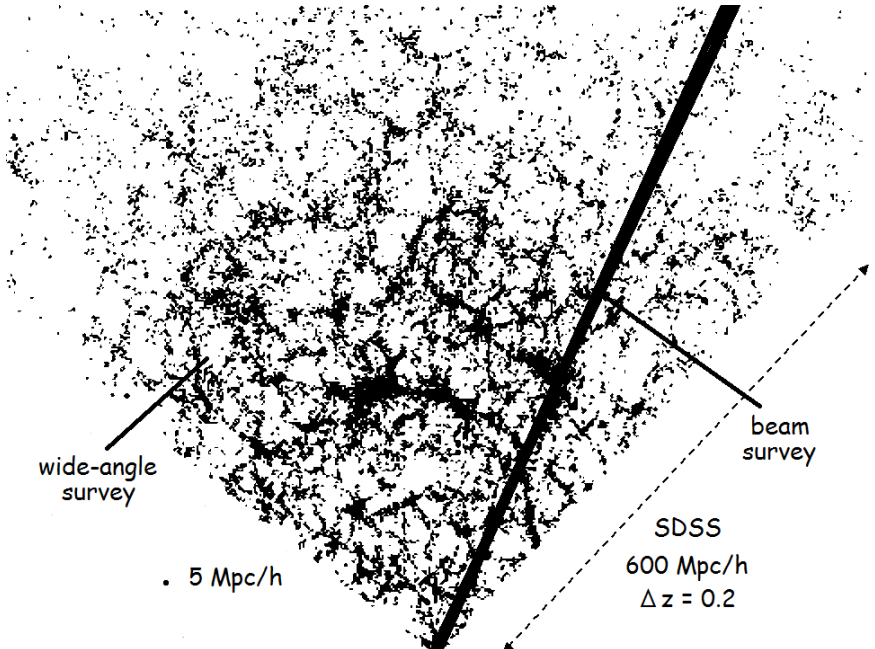


Fig. 1. The galaxy distribution of Sloan Digital Sky Survey. The COSMOS deep field with the size of one square degree marked as the black beam In the picture.

Methods

A cosmic variance is a possible estimate of inhomogeneity structures. The method first proposed in [3] of estimation of sizes and amplitudes of radial fluctuations for different redshift bins was used.

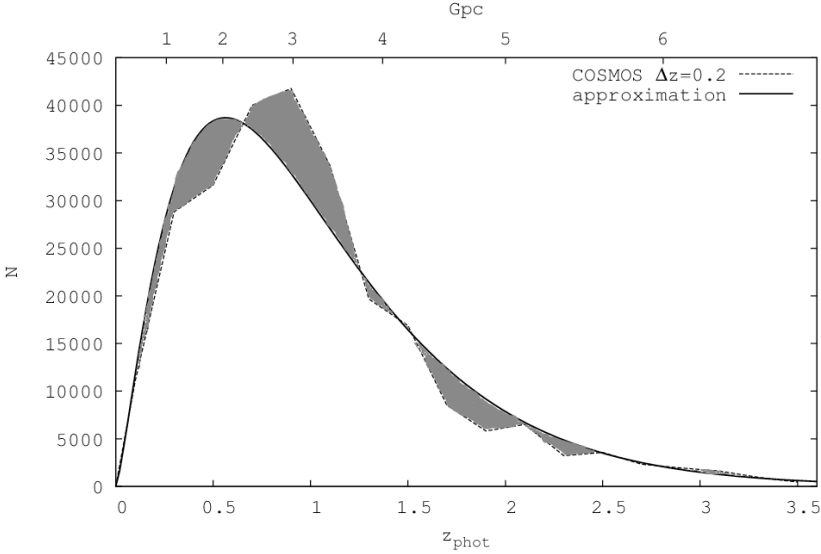


Fig. 2. The approximation of the real radial distribution of the number of galaxies by a uniform (homogeneity) distribution is shown. The gray areas are regions of deficiency or excess of the number of galaxies.

The following uniform distribution approximation formula was used

$$\Delta N_{mod}(z) = A z^\alpha \exp\left(-\frac{z}{z_0}\right)^\beta \Delta z, \quad (1)$$

where A is a normalization parameter and α, β, z_0 – the free parameters for least squares. The deviation of the observed number of galaxies from the model,

$$\delta_{obs}(z, \Delta z) = \frac{\Delta N_{obs} - \Delta N_{mod}}{\Delta N_{mod}}, \quad (2)$$

provides an estimate of the total fluctuation dispersion, $\sigma = |\delta_{obs}|$, that is a cosmic variance. The theoretically expected relative fluctuations variance of the number of galaxies [4-6] is given by

$$\sigma^2(z, \Delta z) = \sigma_{corr}^2 + \sigma_p^2, \quad (3)$$

where σ_p is Poisson's noise ($\sigma_p \sim 1/N^{0.5}$) and σ_{corr} is a cosmic variance of correlation structures given by

$$\sigma_{corr}^2(V, r_0, \gamma) = \frac{1}{V^2} \int_V dV_1 \int_V dV_2 \xi(|r_1 - r_2|, r_0, \gamma), \quad (4)$$

where $\xi(r) = (r_0/r)^\gamma$ is a density correlation function of a spatial galaxy distribution, r_0 and γ are its parameters. The shape of the correlation function determines observed inhomogeneities [4].

For a comparison of radial fluctuations of the different galaxy samples the Pearson's correlation coefficient was used

$$r_{corr} = \frac{cov_{XY}}{\sigma_X \sigma_Y} = \frac{\sum (X - \bar{X})(Y - \bar{Y})}{\sqrt{\sum (X - \bar{X})^2 \sum (Y - \bar{Y})^2}}, \quad (5)$$

where X, Y – the sample's means. The correlation coefficient error in the case of $n < 50$,

$$\sigma_r = \frac{\sqrt{1 - r^2}}{\sqrt{n - 2}}, \quad (6)$$

and its authenticity P according to Student's table were calculated.

Results and Discussion

Table 1. The correlation coefficient, r_{corr} , its error, σ_r , and its authenticity, P , for the red-shift bins $\Delta z = 0.3, 0.2, 0.1$.

Δz	rcorr	σ_r	P
0.1	0.54	0.12	0.999
0.2	0.59	0.16	0.99
0.3	0.79	0.12	0.999

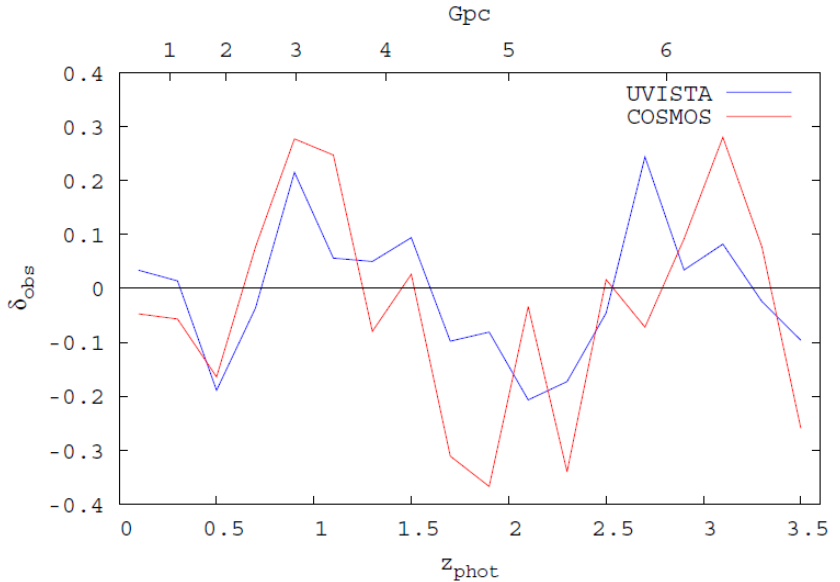


Fig. 3. The relative number density fluctuation of COSMOS and UVISTA for $\Delta z = 0.2$ is shown (for computation of correlation coefficient all graph's points were used).

Conclusion

We can make the following conclusions:

a) In the deep COSMOS field there are fluctuation of the number of galaxies at redshift $z \sim 2$ with amplitude 20% and the linear dimension ~ 1000 Mpc.

b) The independent surveys of the COSMOS field are consistent in the amplitudes and the linear dimension of inhomogeneities with the correlation coefficient $r_{\text{corr}} \sim 0.7$.

c) The observed fluctuations of the number of galaxies may be explained by the power-law correlation function $\xi = (r_0/r)^\gamma$ with parameters $r_0 = 10$, $\gamma = 1$.

References

1. Ilbert O., Capak P. et al. // *Astrophys. J.*, 690, 1236 (2009).
2. Muzzin A. et al. // *Astrophys. J. Suppl.*, 206, 19 (2013).
3. Nabokov N.V., Baryshev Yu.V. // *Astrophysics*, 53, 101 (2010).
4. Gabrielli A., Sylos Labini F., Joice M., Pietronero L. // *Statistical Physics for Cosmic Structures*, Springer, Berlin (2005).
5. Somerville R. et al. // *Astrophys. J.*, 600, L171 (2004).
6. Moster B. et al. // *Astrophys. J.*, 731, 113 (2011).

C. Mathematics and Mechanics

Andronov-Hopf bifurcation of one or more cycles in the Mackey-Glass type delay differential equation

Ignatenko Vera
veraignatenko93@gmail.com

Scientific supervisor: Prof. Dr. Reitmann V., Faculty of Mathematics and Mechanics, Saint-Petersburg State University

1. The Mackey-Glass model

We consider the parameter-dependent model of Mackey-Glass with time-delay nonlinearity [1]. Such a model describes the process of blood cell production and can be written as

$$\frac{dx(t)}{dt} = -ax(t) + \frac{\beta_0 \vartheta^m x(t-\tau)}{\vartheta^m + x^m(t-\tau)}, \quad (1)$$

Where β_0 , ϑ , m , a are positive constants. Here $x(t)$ is the density of mature circulating cells in blood, $ax(t)$ is the mortality rate,

$$\frac{\beta_0 \vartheta^m x(t-\tau)}{\vartheta^m + x^m(t-\tau)}$$

is the blood cell reproduction rate. There is a significant delay $\tau > 0$ between the initiation of cellular production in the bone marrow and the release of mature cells into the blood. Periodic solutions in (1) are associated with chronic and acute human diseases, for example, chronic myelogenous leukemia. The existence of periodic solutions for time-delay systems based on bifurcation theory was considered in [2, 3]. In difference to these papers we consider the degenerate Andronov-Hopf bifurcation in (1).

2. Standard Andronov-Hopf bifurcation

At first we give a short review of the standard Andronov-Hopf bifurcation. Let us consider the system with bifurcation parameter α

$$\dot{x} = f(x, \alpha). \quad (2)$$

Assumptions:

(A1) $f: \mathbb{R}^n \times \mathbb{R} \rightarrow \mathbb{R}^n$ is a real-analytic function;

(A2) $x=0 \in \mathbb{R}^n$ is a stationary point at $\alpha=0$ for (2), i.e. $f(0,0)=0$;

(A3) $\frac{\partial f}{\partial x}(0,0)$ has a pair of complex conjugate eigenvalues $\lambda_1 = \bar{\lambda}_2 = i$ and $n-2$ eigenvalues λ_j with $\text{Re } \lambda_j \neq 0$.

The normal form of system (2) in polar coordinates is given by

$$\begin{cases} \dot{r} = \alpha r + \sigma_1(\alpha) r^3 + \dots, \\ \dot{\theta} = 1 + \text{Im} A_{21}(\alpha) r^2 + \dots \end{cases}$$

Here we assume that the first Lyapunov number $\sigma_1(0) \neq 0$. The coefficient $ImA_{2l}'(\alpha)$ can be computed from equation (2). The description of the standard Andronov-Hopf bifurcation is given in [2, 4] and other books.

3. The first Lyapunov number for the Mackey-Glass equation

Using center manifold theory and the reduction principle [4, 2] we can get conditions for bifurcation parameters and can compute the first Lyapunov number and some coefficients g_{ij} which are used for the Poincaré normal form for the Mackey-Glass equation (1):

$$x_* = \vartheta \left(\frac{\beta_0 - a}{a} \right)^{\frac{1}{m}} \text{ (stationary point);} \quad (3)$$

$$\tau_* = \frac{\arccos\left(-\frac{a}{b}\right)}{\sqrt{b^2 - a^2}} \text{ (critical value of parameter } \tau); \quad (4)$$

$$\sigma_1(0) = \frac{1}{2(\arccos(-\frac{a}{b}))^2} Re \left[ig_{20}g_{11} + \arccos\left(-\frac{a}{b}\right)g_{21} \right], \quad (5)$$

where

$$b = a \left(m \frac{\beta_0 - a}{\beta_0} - 1 \right), \quad (6)$$

$$g_{20} = \frac{1 - i \arccos\left(-\frac{a}{b}\right)}{1 + \left(\arccos\left(-\frac{a}{b}\right) \right)^2} \frac{ma^2 \left(\frac{\beta_0 - a}{a} \right)^{\frac{m-1}{m}}}{\vartheta \beta_0} * \quad (7)$$

$$* \left(-1 - m + 2m \left(\frac{\beta_0 - a}{\beta_0} \right) \right) \frac{\arccos\left(-\frac{a}{b}\right)}{\sqrt{b^2 - a^2}} \exp\left(-2i \arccos\left(-\frac{a}{b}\right)\right),$$

$$g_{11} = \frac{1 - i \arccos\left(-\frac{a}{b}\right)}{1 + \left(\arccos\left(-\frac{a}{b}\right) \right)^2} \frac{ma^2 \left(\frac{\beta_0 - a}{a} \right)^{\frac{m-1}{m}}}{\vartheta \beta_0} * \quad (8)$$

$$* \left(-1 - m + 2m \left(\frac{\beta_0 - a}{\beta_0} \right) \right) \frac{\arccos\left(-\frac{a}{b}\right)}{\sqrt{b^2 - a^2}},$$

$$\begin{aligned}
g_{21} = & \frac{1 - i \arccos\left(-\frac{a}{b}\right)}{1 + \left(\arccos\left(-\frac{a}{b}\right)\right)^2} \left\{ \frac{ma^2}{\vartheta \beta_0} \left(\frac{\beta_0 - a}{a}\right)^{\frac{m-1}{m}} * \right. \\
& * \left(-1 - m + 2m \left(\frac{\beta_0 - a}{\beta_0}\right) \right) \frac{\arccos\left(-\frac{a}{b}\right)}{\sqrt{b^2 - a^2}} * \\
& * [w_{20}(-1) \exp(i \arccos(-\frac{a}{b})) + 2w_{11}(-1) \exp(-i \arccos(-\frac{a}{b}))] + \\
& + \frac{ma^2}{\vartheta^2 \beta_0} \left(\frac{\beta_0 - a}{a}\right)^{\frac{m-2}{m}} \left(1 - m^2 + 6m^2 \left(\frac{\beta_0 - a}{\beta_0}\right) - 6m^2 \left(\frac{\beta_0 - a}{\beta_0}\right)^2 \right) * \\
& * \frac{\arccos\left(-\frac{a}{b}\right)}{\sqrt{b^2 - a^2}} \exp\left(-i \arccos\left(-\frac{a}{b}\right)\right) \left. \right\}.
\end{aligned} \tag{9}$$

Here we have

$$\begin{aligned}
w_{20}(-1) = & E_1 \exp\left(-2i \arccos\left(-\frac{a}{b}\right)\right) + \\
& + \frac{ig_{20} \exp\left(-i \arccos\left(-\frac{a}{b}\right)\right)}{\arccos\left(-\frac{a}{b}\right)} + \frac{i \overline{g_{02}} \exp\left(i \arccos\left(-\frac{a}{b}\right)\right)}{3 \arccos\left(-\frac{a}{b}\right)},
\end{aligned} \tag{10}$$

$$\begin{aligned}
w_{11}(-1) = & \frac{-ig_{11} \exp(-i \arccos(-\frac{a}{b}))}{\arccos(-\frac{a}{b})} + \\
& + \frac{i \overline{g_{11}} \exp(i \arccos(-\frac{a}{b}))}{\arccos(-\frac{a}{b})} + E_2.
\end{aligned} \tag{11}$$

In analogous form we can compute E_1 and E_2 .

Conditions for parameters which guarantee the spectral properties:

- 1) $\beta_0 > a$,
- 2) $(m-2) \beta_0 - m a > 0$.

Theorem: Assume that the coefficients in the Mackey-Glass equation (1) β_0 , ϑ , m , a are such that the first Lyapunov number is zero, i.e. $\sigma_1(0)=0$. Then a degenerate Andronov-Hopf bifurcation in (1) may occur.

4. Degenerate Andronov-Hopf bifurcation

Now we discuss the principal properties of the degenerate Andronov-Hopf bifurcation. We consider system (2) under the following additional assumptions: the first Lyapunov number is zero, i.e. $\sigma_1(0)=0$; the second Lyapunov number is nonzero, i.e. $\sigma_2(0)\neq 0$ (for example $\sigma_2(0)=-1$).

The reduced system in polar coordinates is given by

$$\begin{cases} \dot{r} = \alpha_1 r + \alpha_2 r^3 - r^5 + \dots, \\ \dot{\theta} = 1 + b_1 r^2 + b_2 r^4 + \dots \end{cases}$$

Here $b_1, b_2 \in \mathbb{R}$ are fixed parameters, $(\alpha_1, \alpha_2) \in \Omega \subset \mathbb{R}^2$ are the bifurcation parameters, Ω is a neighborhood of $(0, 0)$. Note that a second parameter is introduced in order to describe the degenerate bifurcation.

We consider limit cycles, which are determined by the relation

$$0 = \alpha_1 r + \alpha_2 r^3 - r^5 + \dots$$

We have two schemes for the creation of limit cycles:

1) $r > 0$, r is small and $\alpha_2 \neq 0$:

$$r^2 = -\frac{\alpha_1}{\alpha_2} + \dots$$

2) $r > 0$ and r is large:

$$r^2 = \frac{\alpha_2}{2} + \sqrt{\frac{\alpha_2^2}{4} + \alpha_1} + \dots$$

Now we can investigate the decomposition of Ω :

$$(i) \infty (\alpha_1, \alpha_2) \in \Omega_1 = \{(\alpha_1, \alpha_2) \in \Omega \mid \alpha_1 > 0\}.$$

a) $\alpha_2 < 0$. A limit cycle exists according to the first scheme (Fig. 1).

b) $\alpha_2 \geq 0$. A limit cycle exists according to the second scheme (Fig. 1).



Fig. 1. Supercritical Andronov-Hopf bifurcation.

$$(ii) \infty (\alpha_1, \alpha_2) \in \Omega_2 = \left\{ (\alpha_1, \alpha_2) \in \Omega \mid \alpha_2 > 0, \alpha_1 < 0, \frac{\alpha_2^2}{4} + \alpha_1 > 0 \right\}.$$

The limit cycle γ_1 exists according to the first scheme, the limit cycle γ_2 exists according to the second scheme (Fig. 2).

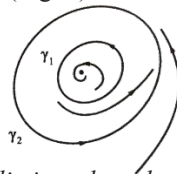


Fig. 2. Two limit cycles – large and small.

$$(iii)^\infty(\alpha_1, \alpha_2) \in \Omega_3 = \left\{ (\alpha_1, \alpha_2) \in \Omega \mid \alpha_2 < 0, \alpha_1 < 0 \right\} \cup \left\{ (\alpha_1, \alpha_2) \in \Omega \mid \alpha_2 \geq 0, \alpha_1 < -\frac{\alpha_2^2}{4} \right\}.$$

There exists only a stationary point (Fig. 3).



Fig. 3. Stable focus.

(iv) $^\infty(\alpha_1, \alpha_2) \in S_1 = \{(\alpha_1, \alpha_2) \in \Omega \mid \alpha_1 = 0\}$. In this domain a super critical Andronov-Hopf bifurcation occurs (Fig. 4).



Fig. 4. Super critical Andronov-Hopf bifurcation.

$\alpha_2 < 0$

$\alpha_2 > 0$

$$(v)^\infty(\alpha_1, \alpha_2) \in S_2 = \left\{ (\alpha_1, \alpha_2) \in \Omega \mid \alpha_1 = -\frac{\alpha_2^2}{4} \right\} \quad \text{Here a semi stable limit cycle is created (Fig. 5).}$$

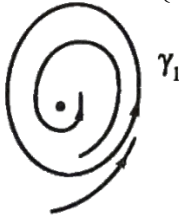


Fig. 5. Semi stable limit cycle.

5. Conclusions

- The standard Andronov-Hopf bifurcation for the Mackey-Glass equation is considered.
- Conditions for the Andronov-Hopf bifurcation in the degenerate case are discussed. This degenerate case leads to the bifurcation of two cycles in the system.

References

1. M.C. Mackey, L. Glass // Science, New Series, v. 197, № 4300, p. 287-289 (1977).
2. B.D. Hassard, N.D. Kazarinoff, Y.-H. Wan // Theory and Applications of Hopf Bifurcation. London Mathematical Society Lecture Note Series 41, Cambridge University Press (1981).
3. J.K. Hale // Journal of Differential Equations, v. 15, p. 278-294 (1974).
4. V. Reitmann // Dynamical systems, attractors and estimates of their dimension. Saint-Petersburg State University Press (2013).

Numerical probabilistic approach to solution of the Cauchy problem for quasilinear parabolic equations

Nemchenko Ekaterina
nemchenko_ekaterina@mail.ru

Scientific supervisor: Prof. Dr. Belopolskaya Y.I., Department of Mathematics, Civil Engineering faculty, Saint-Petersburg State University of Architecture and Civil Engineering

Introduction

Nonlinear parabolic equations arise as mathematical models of various phenomena in physics, biology, financial mathematics and other fields. The problem to solve nonlinear parabolic equations is one of the most difficult and at the same time interesting problems of computational mathematics. There exists no single universal algorithm for solving this type of problems. As a rule, each of these problems requires its own unique approach. Simple problems for partial differential equations in some cases can be solved by analytical methods, discussed in the relevant sections of mathematics. However, in most cases such problems can't be solved analytically and hence needs numerical schemes to solve them, in particular, the probabilistic numerical schemes.

To construct a required scheme to get a solution of the Cauchy problem for a nonlinear parabolic equation one can use at least two different approaches to obtain the probabilistic representation of its solution based on the solution of the corresponding stochastic differential equations.

The problem statement

Consider the Cauchy problem for a quasilinear parabolic equation

$$\frac{\partial u}{\partial t} + \frac{1}{2} A^2(x) \nabla^2 u + a(x) \nabla u + g(x, u, \nabla u) = 0, \quad (1)$$

$$u(T, x) = u_0(x) \quad (2)$$

where

$$x \in R^1, t \in [0, T] \quad u(t, x) \in R^1, a(x) \in R^1, A(x) \in R^1, g(x, u, \nabla u) \in R^1, \nabla u = \frac{\partial u}{\partial x}$$

We aim to construct and implement a numerical algorithm for solving (1) with the Cauchy data (2) based on a probabilistic representation of its solution.

Probabilistic approach to solution of the Cauchy problem

Consider a Cauchy problem for a semilinear parabolic equation

$$\frac{\partial u}{\partial t} + \frac{1}{2} A^2(x) \nabla^2 u + a(x) \nabla u + g(x, u) = 0 \quad (3)$$

$$u(T, x) = u_0(x). \quad (4)$$

It is known [1] that we can use a system

$$\begin{cases} d\xi(\theta) = a(\xi(\theta))d\theta + A(\xi(\theta))dw(\theta), \xi(t) = x, \\ u(t, x) = E[u_0(\xi_{t,x}(T)) + \int_t^T g(\xi(\theta), u(\theta, \xi(\theta)))d\theta] \end{cases} \quad (5)$$

to construct $u(t, x)$. Here $w(\theta)$ is a standard Wiener process.

This approach can be extended to construct a solution of the Cauchy problem (1), (2). To this end we have to consider a system of the form

$$\begin{cases} d\xi(\theta) = a(\xi(\theta))d\theta + A(\xi(\theta))dw(\theta), \xi(t) = x, \\ u(t, x) = E[u_0(\xi_{t,x}(T)) + \int_t^T g(\xi(\theta), u(\theta, \xi(\theta)), \nabla u(\theta, \xi(\theta)))d\theta] \end{cases} \quad (6)$$

since we can get a system of the form (5) from system (6), using the method of differential prolongation.

To explain an alternative approach [3] we assume that u is a classical solution of the Cauchy problem (1), (2). Then we can apply Ito's formula and compute a stochastic differential of the process $u(\theta, \xi(\theta))$

$$du(\theta, \xi(\theta)) = \left[\frac{\partial u}{\partial \theta} + \frac{1}{2} A^2(\xi(\theta)) \nabla^2 u(\theta, \xi(\theta)) + a(\xi(\theta)) \nabla u(\theta, \xi(\theta)) \right] d\theta + A(\xi(\theta)) \nabla u(\theta, \xi(\theta)) dw(\theta).$$

Since u solves (1), we get

$$du(\theta, \xi(\theta)) = -g(\xi(\theta), u(\theta, \xi(\theta)), \nabla u(\theta, \xi(\theta)))d\theta + A(\xi(\theta)) \nabla u(\theta, \xi(\theta))dw(\theta). \quad (7)$$

Let us introduce new processes

$$y(\theta) = u(\theta, \xi(\theta)), \quad z(\theta) = A(\theta) \nabla u(\theta, \xi(\theta))$$

and rewrite (7) in the form

$$dy(\theta) = -f(\xi(\theta), y(\theta), z(\theta))d\theta + z(\theta)dw(\theta), \quad y(T) = u_0(\xi(T)).$$

A couple

$$\begin{cases} d\xi(\theta) = a(\xi(\theta))d\theta + A(\xi(\theta))dw(\theta), \xi(t) = x, \\ dy(\theta) = -f(\xi(\theta), y(\theta), z(\theta))d\theta + z(\theta)dw(\theta), y(T) = u_0(\xi(T)) \end{cases} \quad (8)$$

is called a weakly coupled FBSDE (forward and backward stochastic differential equation). Here

$$f(x, y, z) = \tilde{g}(x, u, A \nabla u) = g(x, u, A^{-1} A \nabla u)$$

By definition a solution of (8) is a triple of F_{t_1} – measurable stochastic processes $(y(t_1), z(t_1), \xi(t_1))$ such that with probability 1

$$\xi(t_1) = x + \int_t^{t_1} a(\xi(\theta))d\theta + \int_t^{t_1} A(\xi(\theta))dw(\theta), \quad t \leq t_1 \leq T,$$

$$y(t_1) = u_0(\xi(T)) + \int_{t_1}^T f(\xi(\theta), y(\theta), z(\theta))d\theta - \int_{t_1}^{T_1} z(\theta)dw(\theta), \quad t \leq t_1 \leq T, \quad a.s.$$

Consider a condition C.1.

Assume that $f: \Omega \times R^1 \times R^1 \rightarrow R^1$ possesses the properties

1). $f(y, z)$ is progressively measurable and square integrable for all $(y, z) \in R^1 \times R^1$;

2). There exist constant μ and K_1, L_1 such that

$$|f(y, z)| \leq K_1[|y| + |z|], \quad y \in R^1, \quad z \in R^1, \quad P - a. s.;$$

3). $|f(y, z) - f(y, z_1)| \leq L_1 |z - z_1|, \quad \forall y \in R^1, \quad z, z_1 \in R^1, \quad P - a. s.;$

4). $(y - y_1)(f(y, z) - f(y_1, z)) \leq \mu |y - y_1|^2, \quad \forall y, y_1 \in R^1, \quad z \in R^1 \quad P - a. s.;$

5). The map $y \rightarrow f(y, z)$ is continuous for any $z \quad P - a. s.$

Under these assumptions the solution of the system (8) is known to exist and the function $u(t, x) = y(t)$ stands for a viscosity solution of the problem (1), (2).

Theorem [3]. Assume C.1. holds and (y, z) is a unique solution of FBSDE (8). Then $u(t, x) = y(t)$ is a unique continuous viscosity solution to (1), (2).

Numerical solution of FBSDEs

One can discretize FBSDE (8) and obtain the following relations [4]

$$\begin{cases} X_0^{n,m} = x, \\ X_{i+1}^{n,m} = X_i^{n,m} + a(X_i^{n,m})h + A(X_i^{n,m})\Delta w_{i+1}, \\ Y_n^{n,m} = u_0(X_n^{n,m}), \\ Z_i^{n,m} = \frac{1}{h} E_{t_i} [Y_{i+1}^{n,m} \Delta w_{i+1}], \\ Y_i^{n,m} = E_{t_i} [Y_{i+1}^{n,m} + f(X_i^{n,m}, Y_{i+1}^{n,m}, Z_i^{n,m})h], \\ u_i^{n,m}(X_i^{n,m}) = Y_i^{n,m}. \end{cases} \quad (9)$$

Here (X, Y, Z) is a discrete solution of (8),

$$h = \frac{T}{n}, \quad y t_i = i h, \quad i = 0, 1, \dots, n,$$

m is a number of iterations and

$$\Delta w_{i+1} = w_{i+1} - w_i.$$

Here E_{t_i} denotes the conditional expectation $E[\cdot | F_{t_i}]$ and F_{t_i} is natural filtration, generated by Wiener process. In this way we construct an approximate solution of the system (8).

To simplify this scheme we approximate a Wiener process

$$w_t^n := \sqrt{h} \sum_j^{\lfloor t/h \rfloor} \varepsilon_j^n, \quad 0 \leq t \leq T,$$

by a sequence i. i. d $\{\varepsilon_j^n\}_{j=1}^n$ valued in $\{-1, 1\}$ with Bernoulli distribution

$$P\{\epsilon_j^n = 1\} = P\{\epsilon_j^n = -1\} = 0.5.$$

Then a discretized form of FBSDE (8) can be rewritten as follows

$$\begin{cases} X_0^{n,m} = x, \\ X_{i+1}^{n,m} = X_i^{n,m} + a(X_i^{n,m})h + A(X_i^{n,m})\epsilon_{i+1}^n\sqrt{h}, \\ Y_n^{n,m} = u_0(X_n^{n,m}) \\ Z_i^{n,m} = \frac{1}{2\sqrt{h}}[Y_+ - Y_-] \\ Y_i^{n,m} = \frac{1}{2}[Y_+ + Y_-] + f(X_i^{n,m}, \frac{1}{2}[Y_+ + Y_-]Z_i^{n,m})h. \end{cases} \quad (10)$$

Here $Y_+ = Y_{i+1}^{n,m} |_{\epsilon_{i+1}^n = 1}$ and $Y_- = Y_{i+1}^{n,m} |_{\epsilon_{i+1}^n = -1}$.

Simulation of BSDE solutions

For simplicity set $\xi(\theta) \equiv w(t) \in R^1$ and $T=1$. To obtain numerical results we choose $u_0(x) = \cos(x)$, $g(t, y, z) = -yz$, where $x \in R^1$.

The numerical results are presented in Figs. 1-2.

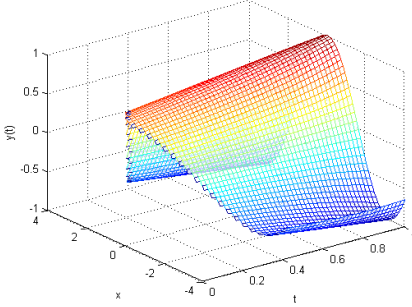


Fig. 1. BSDE solution $y(t)$.

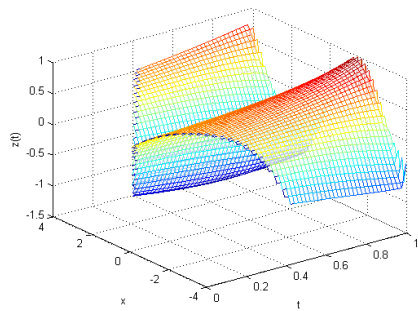


Fig. 2. BSDE solution $z(t)$.

References

1. Ya.I. Belopolskaya., Yu.L. Dalecky // Stochastic equations and differential geometry. Kluwer, p. 295 (1990).
2. Ya. Belopolskaya // Global and Stochastic Analysis, v. 1, № 1, p. 3-402 (2011).
3. E. Pardoux, S. Peng // Backward Stochastic Differential equations and Quasilinear Parabolic Partial Differential Equations, Lecture Notes in CIS 176, Springer, p. 200-217 (1992).
4. S. Peng, M. Xu // ESAIM: Mathematical Modelling and Numerical Analysis, v. 45, Issue: 2, p. 335 – 360 (2011).

Monte Carlo Simulation for Stochastic Differential Equations

Pogosian Anna
anna.a.pogosian@gmail.com

Scientific supervisor: Prof. Dr. Ermakov S.M., Department of Statistical Modelling, Faculty of Mathematics and Mechanics, Saint-Petersburg State University

Introduction

Differential equations as well as stochastic differential equations and their variants appear in many scientific fields including mathematical finance, physics and chemistry, more precisely high-dimensional systems of such equations, which is why numerical solutions for them are of a significant practical use. The proposed method includes technique as follows:

- Let us convert a system of differential equations into an integral one
- Apply Monte Carlo Method to a system of integral equations (using a scheme based on a branching process for a non-linear case and using collision estimate for a linear case)

- Obtain numerical estimation of a solution

In this report the introduced technique is going to be applied to a Riccati equation.

Method

Let us consider a system of differential equations

$$\frac{dX}{dt} = F(t, x_1, \dots, x_m),$$

where $X(t) = (x_1(t), \dots, x_m(t))$ – vector of variables and $F(t, x_1, \dots, x_m) = (f_1, \dots, f_m)$ – vector function

Consequently,

$$\frac{dX}{dt} + \Sigma X = \Sigma X + F(t, x_1, \dots, x_m), \quad (1)$$

Σ – matrix $m \times m$.

Inverse of the system (1) by using a formula with the integrating factor

$$X(t) = e^{-\int_0^t \Sigma d\tau} \int_0^t e^{\int_0^\tau \Sigma d\tau} F(\tau, x_1, \dots, x_m) d\tau$$

Assuming that F is a smooth function of x_1, \dots, x_m and computing a first-order Taylor series expansion we could obtain a polynomial nonlinear system which has been examined thoroughly and in accordance to [1] and [2] is solved by simulating a vector branching process.

We have

$$X(t) = \sum_{m=1}^M \int_0^t K(\tau, x_1, \dots, x_m) \prod_{j=1}^m x_j d\tau + f(t), \quad (2)$$

or

$$X = \mathcal{K}X^{(m)} + f, \quad X^{(m)} = \prod_{j=1}^m x_j$$

Suppose that fixed-point iteration converges

$$X_{n+1} = \mathcal{K}X_n^{(m)} + f, \quad X_0 = f$$

converges for both the equation (2) and the following equation

$$\bar{X} = \bar{\mathcal{K}}\bar{X}^{(m)} + |f|$$

where $\bar{\mathcal{K}}$ is obtained by swapping kernel K for $|K|$.

Conditions necessary for Monte Carlo Method require that majorant process converges, and according to existence theorem for solution of system of ODE this is true in case the interval of integration Δt chosen for time is sufficiently small. Thus, we can find the solution in any interval $[0, T]$ by splitting it up consequently in intervals of length Δt .

Numerical example

In order to explain this algorithm in detail let us provide a simple example.

We want to find a solution of

$$\begin{cases} y' - 2y = x^2 \\ y(0) = 1 \end{cases}$$

In $x_0=0.2$ using a collision estimate.

We have

$$y(x) = \int_0^x 2y(t)dt + \frac{x^3}{3}$$

Therefore,

$$y(0.2) = \int_0^{0.2} E(x-t)2y(t)dt + \frac{x^3}{3}$$

where $E(x-t) = \begin{cases} 0, & x < t \\ 1, & x \geq t \end{cases}$

We are going to simulate N Markov paths $w_{1:\tau}^{(i)}$, each would end in absorption at $t=\tau$ or in case the argument of y is in an ε - neighbourhood of an initial point 0 and therefore the value of y in that point can be changed for $y(0)=1$. At each step of the Markov path we simulate a random variable α that has the uniform distribution on the interval $[0,1]$. Absorption happens when α becomes less than the probability of absorption which is defined by the constant number of 0.25.

$$\begin{aligned} y(0.2) &\approx 2 \frac{0.2}{0.75} y(0.2\alpha_0) + \frac{0.2^3}{3} \\ y(0.2\alpha_0) &\approx 2 \frac{0.2}{0.75} y(0.2\alpha_0 \cdot \alpha_1) + \frac{0.2^3}{3} \end{aligned}$$

$$y(0.2\alpha_{\tau-1}) \approx 2 \frac{0.2}{0.75} y(0.2\alpha_0 \cdot \dots \cdot \alpha_{\tau}) + \frac{0.2^3}{3}$$

Collision estimate

$$J_{\varepsilon} = \left(2 \frac{0.2}{0.75} \right)^{\tau-1} \frac{0.2^3}{3}$$

$$y(0.2) \approx \frac{\sum_{i=1}^N J_{\varepsilon}(w^{(i)})}{N}$$

After solving the equation analytically we have $y(0.2)=1.4947$.

N	Collision est
25	1.3807
50	1.4961
100	1.5013
1000	1.4941
$y(0.2)$	1.4947

Considering that the standard deviation doesn't exceed 30% in all of the investigated cases we are satisfied with the algorithm.

Conclusion

Although the theory concerning Monte Carlo Methods for polynomial nonlinear equations is quite well-studied in the works of Ermakov S.M. [1, 2], no applications for differential equations have been introduced yet. In this report we have attempted to provide such. The far-reaching plan is to try to apply the aforementioned technique to the case of a system of a stochastic differential equations.

References

1. Ermakov S.M. Method Monte Carlo in numerical mathematics. Introductory course. - Saint Petersburg: Nevskiy Dialekt; Moscow: Binom, 2009. – 143 p.
2. Ermakov S.M., Mikhailov G.A. Statistical modelling. -Moscow: Nauka, 1982. -251 p.

Simulations of high-velocity star motions in the Galactic gravitational field

Shirokova Kseniia
xebusk@mail.ru

Scientific supervisor: Prof. Dr. Orlov V.V., Department of Celestial Mechanics, Faculty of Mathematics & Mechanics, Saint-Petersburg State University

Introduction

The first hypervelocity star was opened in 2005 by W. Brown et al. Now there are known about twenty such objects but their origin still remains unclear. The most probable scenario of their origin was proposed long before their observations: in 1988 by J. Hills [1]. He suggested that as a result of interaction between a close binary system and the supermassive black hole: one of the components can fly away at high speed (about several thousand kilometers per second).

In the present work the motions of a star after this interaction were studied. 1 000 variants of the initial velocities were considered for three different initial approaches of a binary system with a black hole, star motion equations were integrated by Runge-Kutta method of fourth order.

Results and Discussion

The aim of the work was to study the motions of the stars in the regular field of the Galaxy after the escape from the central region. A star was placed at the distance of 1 pc from the Galactic center; a speed and an angle of the initial velocity to the Galactic plane were fixed. The system of the star motion equations

$$\ddot{x} = -\partial \Phi(x, y, z) / \partial x,$$

$$\ddot{y} = -\partial \Phi(x, y, z) / \partial y$$

$$\ddot{z} = -\partial \Phi(x, y, z) / \partial z$$

was numerically integrated by the Runge-Kutta fourth-order method. Calculations achieved 150 million years (due to the characteristic lifetime of the B stars on the main sequence – such objects are often observed as high-speed) or departure from the center of the Galaxy at 120 kpc (the approximate size of the Galactic halo) were performed.

Three different form of the gravitational field potential of the Galaxy were considered: Irrgang et al. [2], Fellhauer et al. [3], and Gardner et al. [4] models.

For example, model [3]:

$$\Phi = \Phi_d + \Phi_b + \Phi_h$$

$$\Phi_d = -G \times M_d / \sqrt{x^2 + y^2 + \left(b + \sqrt{z^2 + c^2}\right)^2}$$

$$\Phi_b = -G \times M_b / \sqrt{x^2 + y^2 + z^2 + a}$$

$$\Phi_h = v_0^2 / 2 \times \ln \left(x^2 + y^2 + z^2 / q_0^2 + d^2 \right)$$

In all models the potential is represented by the sum of three galactic component potentials: disk, bulge, and halo; in [4] the disk is separated into stellar and gas-dust components and those consist of several terms. The potentials of all three models have a rotational symmetry. Since the star departs almost from the center of the galaxy, its orbit will be in the plane perpendicular to the Galactic plane.

The results of numerical modeling (Table 1) show that model [2] allocates at higher speeds: lift height and maximum distance from the galactic axis of rotation several times more than in other models.

Table 1. The maximum height and maximum distance from the axis of rotation of orbits in units $d=10$ kpc for initial speeds 300 and 600 km/s and angles of initial velocity inclination with respect to the galactic plane 0° , 30° , 60° , and 90° .

		Height				Distance			
Model	v_0	0°	30°	60°	90°	0°	30°	60°	90°
[2]	300	0	0.014	0.023	0.027	0.02	0.027	0.027	0.026
[3]	300	0	0.010	0.016	0.018	0.018	0.018	0.018	0.018
[4]	300	0	0.018	0.032	0.037	0.038	0.037	0.035	0.034
[2]	600	0	0.499	1.000	1.166	1.265	1.265	1.265	1.265
[3]	600	0	0.214	0.205	0.216	0.276	0.274	0.249	0.274
[4]	600	0	0.297	0.297	0.311	0.616	0.616	0.616	0.616

The next step is the addition of the point potential of the central black hole of 10^7 solar masses to the model [3]. The potential gets the new part:

$$\begin{aligned}\Phi &= \Phi_d + \Phi_b + \Phi_h + \Phi_{BH} \\ \Phi_d &= -G \times M_d / \sqrt{x^2 + y^2 + \left(b + \sqrt{z^2 + c^2}\right)^2} \\ \Phi_b &= -G \times M_b / \sqrt{x^2 + y^2 + z^2} + a \\ \Phi_h &= v_0^2 / 2 \times \ln \left(x^2 + y^2 + z^2 / q_\square^2 + d^2 \right) \\ \Phi_{BH} &= -G \times M_{BH} / \sqrt{x^2 + y^2 + z^2}\end{aligned}$$

As you can see from the Fig. 1, the black hole significantly affects the star movement: an orbit that was lying in the galactic plane becomes chaotic – this is due to calculation errors during close encounters of a star with a black hole. Orbits become more compact.

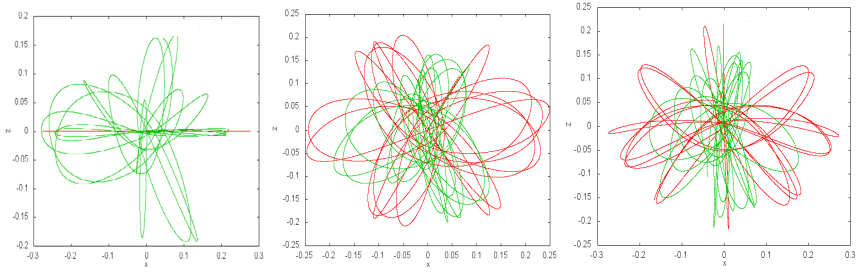


Fig. 1. Orbits in red color are in the model without black hole, green – with it. Initial conditions: speed is 600 km/s, angles between initial velocities and the galactic plane are 0, 60 and 90 degrees.

Motions of stars ejected from the Galactic center as a result of the interaction of a close binary system and the supermassive black hole have also been simulated according to calculations made in [5]. The sample of departure velocities for different approaches of double star and the black hole were taken from [5], ejection angles were chosen randomly.

Fig. 2 shows the distribution of a tangent of orbit initial inclination angle and the star initial velocity for three encounter options: 100, 500 and 3000 solar radii. Red color means escaping stars, green corresponds to remaining stars. It is seen that with increasing distance of approach the points cloud moves to the left that means rising the number of remaining stars. The boundary value between outgoing and remaining stars equals about 1200 km/s in all three cases. The proportions of escaping from the Galaxy stars are approximately 80, 70 and 50 percent.

The following graphs are shown for remaining stars only.

In the Fig. 3 for all three options is clearly visible the rapprochement dependence: at the beginning the graph is flat, and then it rises sharply. Most likely this is due to the galactic disk influence.

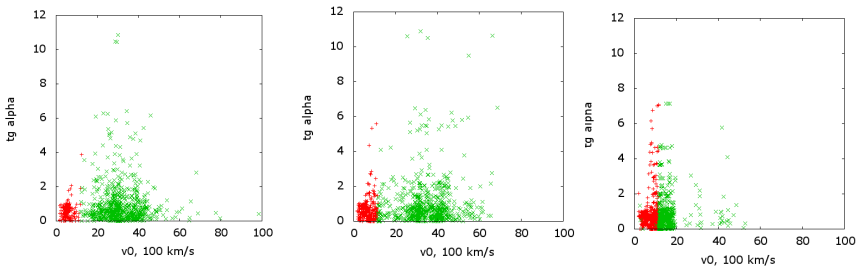


Fig. 2. The dependence of the initial orbit inclination tangent on the initial speed of stars (in units $v=100$ km/s) for approach distances of 100, 500 u 3000 solar radii. Red color means escaping stars, green color means remaining stars.

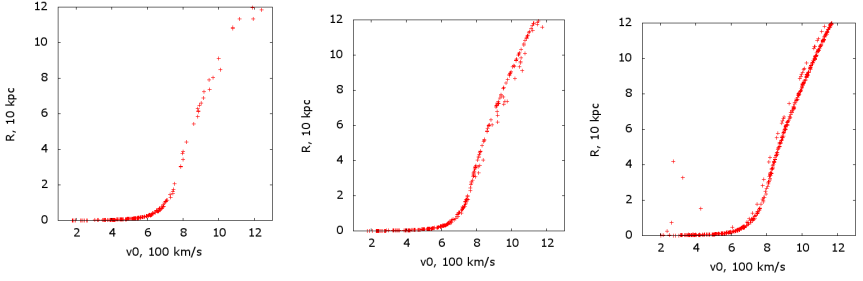


Fig 3. The dependence of maximum galactocentric distances on initial speeds for approach distances 100, 500 u 3000 solar radii .

Fig. 4 shows the dependence of the orbit flattening on the initial speed. For speeds smaller than 600 km/s is the clear upper boundary equals to unity, it is also most likely due to the galactic disk influence. With increasing distance of approach relative orbit heights rise.

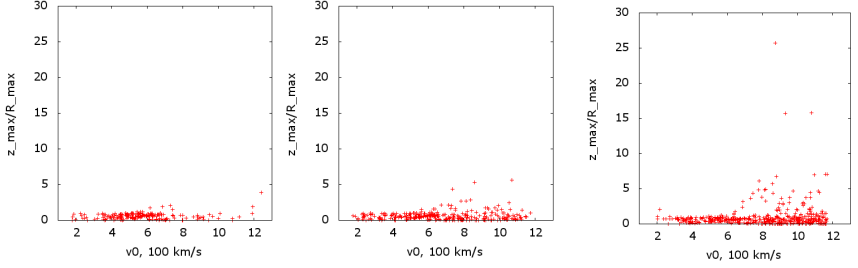


Fig. 4. The dependence of the orbit flattening on initial speeds for approach distances of 100, 500 u 3000 solar radii.

Let's consider the dependence of the maximum lift of the orbit on the initial speed (Fig. 5). There is a general pattern for all occasions: for the initial velocities of less than 600 km/s the plot is flat, then it increases with the overall envelope on the left, it is also probably explained by the influence of the galactic disk.

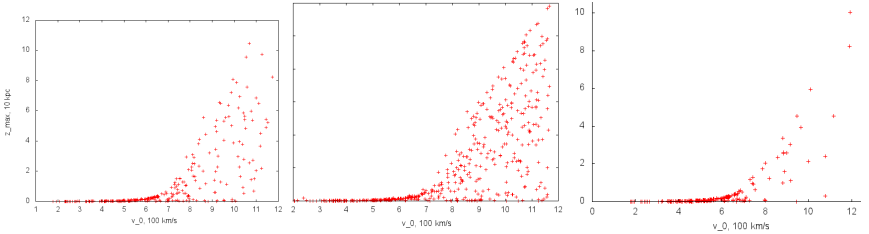


Fig. 5. The dependence of the maximum height of the orbit on the initial speed of the star for the approach distances of 100, 500 u 3000 solar radii.

Conclusions

We can make the following conclusions:

a) The type of orbit of a star ejected from the Galactic center essentially depends on two parameters: the ejection speed and the angle between the initial velocity and the galactic plane.

b) The central supermassive black hole has a strong effect on the motion of stars in the central region; the orbits become more compact.

c) The percent of stars escaping from the Galaxy rises with decreasing the distance of approach between a binary system and a black hole.

d) The boundary value between the ejecting speeds of escaping vs. remaining stars is approximately equal to 1200 km/s and does not depend on the angle between the initial velocity and the Galactic plane.

References

1. J.G. Hills // Nature 331, 687 (1988).
2. A. Irrgang et al. // Astron. Astrophys. 549, id. A137, 13 pp. (2013).
3. M. Fellhauer et al. // Astrophys. J. 651, 167 (2006).
4. E. Gardner et al. // Monthly Not. Roy. Astron. Soc. 411, 947 (2011).
5. G.N. Dremova, V.V. Dremov, and A.V. Tutukov // Astronomy Reports 58, 291 (2014).

Caratheodory dimension of invariant sets for dynamical systems with multiple time

Voynov Dmitriy
voynov@math.spbu.ru

Scientific supervisor: Prof. Dr. Reitmann V., Faculty of Mathematics and Mechanics, Saint Petersburg State University

Introduction

A dynamical system with multiple time (DSMT) is a generalization of a standard dynamical system, i.e. a system with one dimensional time. Such DSMT may be generated by partial differential equations and Pfaffian systems. They have applications in differential geometry, mathematical physics and other fields [1].

For standard dynamical systems special outer Caratheodory measures are constructed in [2, 3]. These outer measures give the opportunity to estimate Hausdorff measures and the Hausdorff dimension of attractors for standard dynamical systems.

We use analogous methods for the construction of a Caratheodory structure in the form of so called containers for dynamical systems with multiple time [4].

Dynamical systems with multiple time

Let us involve some definitions. Let (M, p) be a metric space. We will consider $T = R^k$ as set of time parameters.

Definition 1: Let $\{\phi^t\}_{t \in R^k}$ be a set of continuous maps $\phi^t: M \rightarrow M$. The pair $(\{\phi^t\}_{t \in R^k}, (M, p))$ is called *dynamical system with multiple time* on the metric space (M, p) if the following conditions are satisfied [1]:

1. $\phi^0(p) = p$ for any $p \in M$.
2. $\phi^s(\phi^t(p)) = \phi^{t+s}(p)$ for any $t, s \in R^k, p \in M$.

Definition 2: For any $p \in M$ the set

$$\gamma(p) := \{\phi^t(p) | t \in R^k\}$$

is the *orbit* of the dynamical system with multiple time through the point p .

Definition 3: The set $A \subset M$ is called [*positively*] [*negatively*] *invariant* if $\phi^t(A) \subset [A] \supset A$ for any $t \in R^k$.

Generators for systems with multiple time

Let $M = R^n$ and $X \subset R^n$. $\text{Hom}(R^k, R^n)$ is the vector space of bounded linear maps, $f: X \rightarrow \text{Hom}(R^k, R^n)$ continuous map. We consider the equation

$$dx_t = f(t, x(t)) \quad (1)$$

Where dx_t is the differential of the smooth map $x: R^k \rightarrow X$ at the point t . The following criteria of complete integrability are given by the Frobenius theorem [1].

Theorem 1: Equation (1) is completely integrable if and only if for any $x \in X$ the bilinear operator

$$df(x)f(x) \in \text{Hom}(R^k, \text{Hom}(R^k, R^n)) \quad (2)$$

is symmetric.

Thus the existence of the dynamical system $(\{\varphi^t\}_{t \in \mathbb{R}^k}, (R^n, \|\cdot\|))$ is equivalent to the completely integrability of equation (1) [5].

Caratheodory dimension

Let X be an arbitrary set, F be some set of subsets of X , P be a parameter set (if d_* is finite, then $P := [d^*, +\infty)$, else $P = \mathbb{R}$), and let the following three functions be given $\xi: F \times P \rightarrow R_+$, $\eta: F \rightarrow R_+$ and $\psi: F \rightarrow R_+$. We shall suppose that the following conditions are satisfied [2], [6]:

$$(A) \emptyset \in F, \psi(\emptyset) = 0, \xi(\emptyset, d) = 0, \forall d \in P.$$

$$(B) \xi(A, d + s) = \eta(A, s) \xi(A, d), \forall A \in F, \forall d, s \in P.$$

(C) For any $\varepsilon > 0$ there exists $\delta > 0$ such that for any $A \in F$ with $\psi(A) \leq \delta$ it holds $\eta(A, d) \leq \varepsilon$ if $d > 0$, $d \in P$ and $\eta(A, d) \leq \varepsilon^{-1}$ if $d < 0$, $d \in P$.

(D) For any $\varepsilon > 0$ there exists $A \in F$ for which $\psi(A) = \varepsilon$.

We say that $Z \subset X$ is an admissible set if for any $\varepsilon > 0$ there can be found some finite or countable set U of subsets from F , forming a cover of Z .

(E) Any subset $Z \subset X$ is admissible.

A collection (F, P, ξ, η, ψ) which satisfies (A)-(E) is called a *Caratheodory (dimension) structure* on X . Let Z be an arbitrary subset of X and $d \geq d^*$, $\varepsilon > 0$ numbers. Define the *Caratheodory d -measure at level ε of Z with respect to (F, P, ξ, η, ψ)* by

$$\mu_c(Z, d, \varepsilon) := \inf_{A \in U} \xi(A, d) \quad (3)$$

where infimum is taken over all finite or countable sets U of subsets from F covering Z and such that $\psi(A) \leq \varepsilon$ for all $A \in U$.

Definition 5: The function $\mu_c(Z, d) := \lim_{\varepsilon \rightarrow 0} \mu_c(Z, d, \varepsilon)$ is called *Caratheodory d -measure with respect to (F, P, ξ, η, ψ)* .

Definition 6: For a fixed $Z \subset X$ the value

$$\dim_c = \sup_{\mu_c(Z, d) = +\infty} d = \inf_{\mu_c(Z, d) = 0} d$$

is called *Caratheodory dimension* of the set Z with respect to the structure (F, P, ξ, η, ψ) .

Caratheodory structure for dynamical systems with multiple time

Let the metric space (M, p) be $(R^n, \|\cdot\|)$. We assume that $(\{\varphi^t\}_{t \in \mathbb{R}^k}, (R^n, \|\cdot\|))$ is a dynamical system with multiple time. We can determine a partial order on R^k using a convex pointed cone $C \subset R^k$, assuming that $x \leq y$ if $y - x \in C$. Thus C is a filter of sections on R^k . This structure helps us to define the limits of sequences. Let us generalize the notion of an interval on R^k . If $C \in R^k$ is a convex pointed cone then $[a, b]_C := \{a \leq x \leq b | x \in R^k\}$ is an interval on R^k with respect to C . For a fixed cone let us write $[a, b]$ and call it interval. Let $[a, b] \subset R^k$ be an interval, $c: [a, b] \rightarrow R^n$ be a smooth map. We define the ε -container $\Omega(c, \varepsilon)$ as

$$\Omega(c, \varepsilon) = \bigcup_{p \in c([a, b])} B(p, \varepsilon), \quad (4)$$

where $B(p, \varepsilon) = \{u \in R^n \mid \|u - p\| < \varepsilon\}$ is an ε -ball centered at the point p .

Consider intersections of straight lines with an interval $[a, b]$ in R^k . The restriction of the smooth map c for each non-empty such segment defines a curve inside of the orbit. We will define the parameter l_0 as the maximal length of the curves generated by c . For a some compact set $K \in R^k$ and a number $l_0 > 0$ consider a set of images of continuous maps $\Gamma(l_0) = \{c([a, b])\}$ for which the maximal length of curves for every domain is l_0 and for every $\varepsilon > 0$ the following covering property is satisfied:

The union of ε -containers $\Omega(c, \varepsilon)$ where $c \in \Gamma(l_0)$ is a covering of K . We will construct a Caratheodory structure of ε -containers with length l_0 on K using methods analogous to [3].

Suppose the following:

$$F = \{\Omega(c, \varepsilon) \cap K : c \in \Gamma(l_0), \varepsilon > 0\} \cup \{\emptyset\}, P = [1, +\infty), \\ \xi(\Omega(c, \varepsilon) \cap K, d) = \varepsilon^{d-k}, \eta(\Omega(c, \varepsilon) \cap K, s) = \varepsilon^s, \psi(\Omega(c, \varepsilon) \cap K) = \varepsilon \quad (5)$$

For $c \in \Gamma(l_0)$ with $\Omega(c, \varepsilon) \cap K \neq \emptyset$ and $\xi(\emptyset, d) = \psi(\emptyset) = 0$, $\eta(\emptyset, s) = 1$ for all $d \in P$, $s \in R$.

Proposition 1: The container structure constructed above is a Caratheodory structure on K .

Proof: We should check conditions (A)-(E).

(A) Follows from the definition.

$$(B) \xi(\Omega(c, \varepsilon) \cap K, d) \eta(\Omega(c, \varepsilon) \cap K, s) = \varepsilon^{d-k} \varepsilon^s = \varepsilon^{(d+s)-k} = \\ = \xi(\Omega(c, \varepsilon) \cap K, d+s), d, s \in P \text{ where } \varepsilon > 0 \text{ is arbitrary.}$$

(C) Since $\eta(\Omega(c, \varepsilon) \cap K, d) = \psi(\Omega(c, \varepsilon) \cap K)^d$ we can take $\delta = \varepsilon^{-d}$.

(D) Follows from the definition.

(E) Since K is a compact set, we can choose for any $\varepsilon > 0$ a finite subcover of ε -containers.

Conclusion

We have considered dynamical systems with multiple time. For invariant sets of such systems the construction of a Caratheodory structure is described. This structure can be used for the estimation of a Hausdorff dimension.

References

1. Gaishun I.V. Completely Integrable Multidimensional Differential Equations. (In Russian). -Moscow: Nauka i tehnika, 1983, -258 p.
2. Boichenko V.A., Leonov G.A., Reitmann V. Dimension Theory for Ordinary Differential Equations. -Wiesbaden: Teubner, 2005, -405 p.
3. Leonov G.A. // Vestnik of Saint Petersburg State University (in Russian), v.1, №4, pp. 24-31 (1995).

4. Voynov D.A. // Caratheodory dimension structure for general dynamical systems (in Russian). Year project, Saint Petersburg State University, pp. 1-10 (2014).
5. Amelkin V.V. Autonomous and Linear Multidimensional Differential Equations. (In Russian). –Moscow: Editorial URSS, 2003, -142 p.
6. Pesin Ya.B. // Uspekhi Matematicheskikh Nauk (in Russian) v.43, №4, pp. 95-128 (1988).

D. Solid State Physics

Magnetic-field induced variation of energy dispersion of exciton in CdTe

Bodnar Stanislav
stasbodnar@mail.ru

Scientific supervisor: Dr. Loginov D.K., Department of Solid State Physics, Faculty of Physics, Saint-Petersburg State University

Introduction

Variation of exciton dispersion in magnetic field is extensively studied since 2007. In papers [1, 2], optical reflection spectra for nanostructures with the CdTe/CdZnTe quantum well (QW) in magnetic field (Voigt geometry) were measured and discussed. It has been shown that the application of magnetic field to the sample leads to the change of exciton dispersion. These changes are described in framework of the perturbation theory considering operator [1]:

$$\hat{V} = \frac{2a_B \hbar e}{cM} \mathbf{K} \mathbf{B}_x \mathbf{I} \quad , (1)$$

where e is the electron charge, c is the velocity of light; $M = m_e + m_h$ is the exciton mass, where m_e and m_h the electron and hole effective masses; \mathbf{K} is the exciton wave vector, \mathbf{B}_x is the magnetic field, \hbar is the Planck constant, a_B is the Borh radius, $I = 0.68 a_B$.

The change of exciton dispersion was treated contradictory. In papers [1, 2], it was treated as an increase of effective exciton mass. At the same time, in papers [3, 4] it was attributed to the magnetic-field-induced non-parabolic exciton dispersion. In present work, we compare contributions of the non-parabolicity and of the effective mass change to the exciton dispersion.

Theoretical model

Authors of Refs. [3, 4] investigated a QW, which width is much greater than the Borh exciton radius. In such a wide QW, the exciton states can be described in framework of the hydrogen-like model.

We consider an exciton moving along z axis in a crystal with cubic symmetry. The z -axis coincides with direction [001]. This direction is also the axis of quantization of the exciton angular and spin momenta. Magnetic field is applied along the x -axis coinciding with crystallography axis [100]. For calculation of exciton dispersion in magnetic field, we use the stationary perturbation theory.

Solutions of the unperturbed problem are the hydrogen-like wave functions. Basis of eigenfunctions is composed of the $1s$ ground state and of the $2p^{\pm 1}$ excited states of the exciton. The superscript denotes the projection of orbital angular momentum on the z axis. The excited $2p^0$ state does not noticeable affect the phenomenon under consideration. We do not consider other states because they are moved by perturbation (1) in the zone of the continuous spectrum of states at the magnetic fields of 7 T used in papers [1, 2].

Energy of the pure 1s-ground state, E_{1s} , and of the 2p-excited state, E_{2p} , of exciton in cross magnetic field are given by:

$$E_{1s} = E_g - R + \frac{\hbar^2 K^2}{2M} + DB^2, \quad (2')$$

$$E_{2p} = E_g - \frac{R}{4} + \frac{\hbar^2 K^2}{2M} + 6DB^2, \quad (2'')$$

where

$$D = \frac{1}{8} a_B \left(\frac{e}{c} \right)^2 \frac{1}{M^2} \left(\frac{m_h^2}{m_e} + \frac{m_e^2}{m_h} \right).$$

Here E_g is the bandgap, R is the exciton binding energy (exciton Rydberg), D is a parameter of diamagnetic shift.

Matrix element of perturbation (1) describes the mixing of 1s and 2p states. It is nonzero between these state due to symmetry of 1s and 2p wave functions. The matrix of exciton Hamiltonian in this basis reads:

$$H = \begin{pmatrix} E_{1s} & V & V \\ V^* & E_{2p}^+ & 0 \\ V^* & 0 & E_{2p}^- \end{pmatrix} \quad (3)$$

For simplicity, we do not consider Zeeman splitting, which is described by operator $V_b = 0.5 \mu_B$. In our case, this operator leads to a light mixing of optically active and optically inactive exciton states [3, 4]. This mixing insignificantly affects the non-parabolicity and the change of effective exciton mass. We also neglect the mixing of $2p^+$ -states and $2p^-$ -states. Calculations show that this mixing gives rise to relatively small effects.

For calculation of dispersion dependence, one should solve the Schrödinger equation and find eigenvalues for every wave vector K . The problem is reduced to solution of secular equation:

$$\det[H - IE] = 0, \quad (4)$$

where I is the unit matrix. Variation of dispersion caused by own non-parabolicity is determined by the matrix elements of operator (1).

At the same time, mixing of 1s and 2p states leads to change of effective exciton mass in these states. This effect described within the second order of perturbation using the follow matrix element:

$$V_2 = \frac{\langle s|V|p \rangle \langle p|V|s \rangle}{E_{1s} - E_{2p}} \quad (5)$$

Results

We solved the secular equation (4), using additional in the first (1) and in the second (5) order of perturbation theory. In calculation were used next value of material constant of CdTe: permittivity $\epsilon = 9.7$, bandgap $E_g = 1600$ meV, electron mass $m_e = 0.096m_0$, heavy hole mass $m_h = 0.66m_0$, parameter of diamagnetic shift $D = 1.2449 \cdot 10^{-2}$ meV/T. Fig. 1 presents dispersion curves calculated in the first and in the second order of perturbation theory.

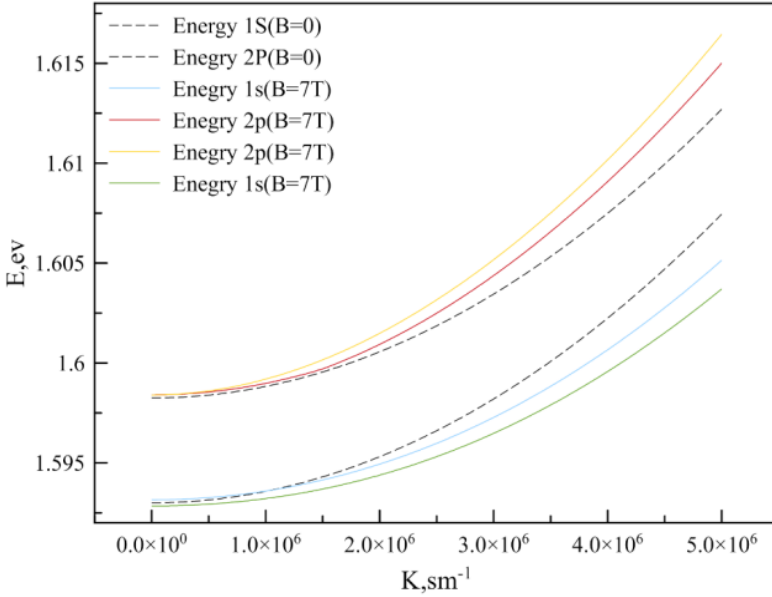


Fig. 1. Dispersion of exciton states. Dashed curves demonstrate dispersion of 1s and 2p states in zero magnetic field. Red curve shows dispersion of 2p-state calculated taking into account only the contribution of non-parabolicity, yellow curve calculated taking into account non-parabolicity and the change of effective mass in magnetic field 7T. Blue curve shows dispersion of 1s state, calculated taking into account non-parabolicity, green curve shows dispersion of 1s-state, taking into account non-parabolicity and change of effective exciton mass in magnetic field 7T.

Fig. 1 shows component which takes into account non-parabolicity, leads to a significant change in curvature of the dispersion to increasing in magnetic field for 2p states and to decreasing in magnetic field for 1s states. In other words dispersion curves diverge proportionally of wave vector K . Correction responsible for change of effective exciton mass leads to additional splitting of dispersion of ground and excited states.

In order to compare the effect of non-parabolicity and the effect of effective exciton mass change we calculated change dependency of exciton energy in magnetic field on wave vector K .

These changes were calculated using the following equation:

$$\Delta E_{2p} = E_{2p,(B=7T)} - E_{2p,(B=0T)} \text{ for 2p states,}$$

$$\Delta E_{1s} = E_{1s,(B=7T)} - E_{1s,(B=0T)}, \text{ for 1s states, where } E_{2p,(B=7T)}, E_{1s,(B=0T)} - \text{energy of exciton states calculated in zero magnetic field, } E_{2p,(B=7T)}, E_{1s,(B=7T)} - \text{energy of exciton}$$

states calculated in magnetic field 7T in view of effective exciton mass change and non-parabolicity.

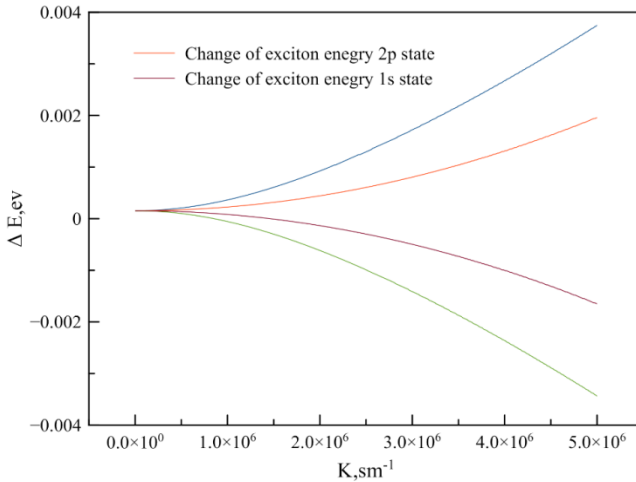


Fig. 2. Change of exciton states dispersion. Red curve shows change of exciton dispersion for 2p states calculated in view of non-parabolicity, blue curve shows exciton dispersion for 2p states in view of non-parabolicity and change of effective exciton mass. Purple curve shows change of exciton dispersion for 1s states calculated in view of non-parabolicity, green curve shows exciton dispersion for 1s states in view of non-parabolicity and change of effective exciton mass.

As it can be seen from Fig. 2, change of exciton dispersion at the expense of the second order of perturbation theory has the same order of magnitude, as the change caused by non-parabolicity. Additive parabolic in K responsible for the effect of the effective exciton mass change, is about half of linear in K additive, responsible for effect of own non-parabolicity. In this way, both of these contributions in spectra of QW reflection in cross magnetic field should be taken into count.

Conclusion

Comparative evaluation of magneto-field-induced non-parabolice additive and parabolic additive to dispersion of exciton was carried out. Both contributions give the same order of magnitude as the values, which makes it necessary to include both magnetic field contributions into the calculation of the dispersion dependences.

References

1. D. Loginov, V.P. Kochereshko, A. Litvinov, L. Besombes, H. Mariette, J.J. Davies, L.C. Smith and D. Wolverson // *Acta Phys. Pol. A*, 112, N2, 381-386 (2007).
2. D.K. Loginov, V.P. Kochereshko, R.T. Cox, L. Besombes, H. Mariette, J.J. Davies, D. Wolverson, and L.C. Smith // *Phys. Status Solidi B*, 247, No. 6, 1528-1530 (2010).
3. D.K. Loginov // *Physics of the Solid State*, 52, No. 1, 70-78 (2010).
4. D.K. Loginov and A.D. // *JETP*, 113, No.3, 502-509 (2011).

Direct numerical solution of Schroedinger equation for excitons in quantum wells

Khramtsov Evgeniy, Belov Pavel, Grigoryev Philipp
xes2608@mail.ru

Scientific supervisor: Prof. Dr. Verbin S.Yu., Department of Solid State Physics, Faculty of Physics, Saint-Petersburg State University

Introduction

The binding energy of a free exciton is easily calculated for various types of semiconductors. For example, in the case of bulk GaAs semiconductor, this energy is: $R_x = 4.2$ meV [1]. The simplicity of the calculation originates from the fact that the free exciton is described by the hydrogen-like one-dimensional Schroedinger equation (SE) with the Coulomb potential [2]. On the contrary, study of the exciton in the quantum well (QW) requires consideration of the three-dimensional SE. In addition to the Coulomb potential, this equation contains two square QW potentials [3]. For the infinite QW potentials, the very narrow QW can be approximated by the two-dimensional SE and the exciton binding energy approaches $4 R_x$ as the width of QW goes to zero [5]. This is not valid for QW of finite thickness.

In the case of the finite QW potentials, an additional complication of the problem appears since the wave function penetrates under the potential barriers. When the QW width approaches zero, the three-dimensional SE is reduced to the one-dimensional SE, but not to two-dimensional one. As a result, the exciton binding energy becomes equal to R_x , the same as for the free exciton.

Precise calculation of the exciton energy for QWs of intermediate widths remains a complicated computational problem although, during the last three decades, the exciton binding energy has been calculated several times for various semiconductors. Calculations has been done using various approximations generally based on variational calculations with prescribed assumptions on the wave function [3-5, 8]. The development of numerical methods [6] as well as the computational facilities made it possible to accurately solve the three dimensional SE without preconceived approximations [7]. As a result, the exciton binding energy can be precisely calculated.

This paper is devoted to solving of the three dimensional SE for the exciton in QW and the determination of the exciton ground state. To our knowledge, the direct numerical solution of the SE for the exciton in QW is reported for the first time. The applied numerical method shows the convergence of the results and consequently a very good precision of the obtained exciton binding energy for the wide range of QW widths. The uncertainties of binding energy are also estimated.

Numerical solution of Schroedinger equation

In the simplest case, the exciton in QW is described by the six-dimensional SE with the Hamiltonian [4]

$$\hat{H} = \frac{\hat{k}_e^2}{2m_e} + \frac{\hat{k}_h^2}{2m_h} + V(z_e) + V(z_h) - \frac{e^2}{\epsilon|\vec{r}|}, \quad (1)$$

Where m_e and m_h are the effective masses of the electron and the hole in semiconductor, $V(z_e)$, $V(z_h)$ are the square QW potentials, $|\vec{r}|$ is the relative distance and

$$\hat{k}_{e,h} = -i\hbar\nabla_{e,h}$$

We separate the center of mass motion and represent the Laplace operator in cylindrical coordinates. We represent the unknown function as

$$\Psi(z_e, z_h, \rho) / \rho$$

in order to guarantee its zero value at $\rho=0$, that in turn avoids singularity of the second derivative of the wave function at $\rho=0$. As a result, the original SE is reduced to the three-dimensional one [3]

$$\left(K + V(z_e) + V(z_h) - \frac{e^2}{\epsilon\sqrt{\rho^2 + (z_e - z_h)^2}} - \frac{E_\phi}{\rho^2} \right) \Psi(z_e, z_h, \rho) = E_x \Psi(z_e, z_h, \rho), \quad (2)$$

where

$$K = -\frac{\hbar^2}{2m_e} \frac{\partial^2}{\partial z_e^2} - \frac{\hbar^2}{2m_h} \frac{\partial^2}{\partial z_h^2} - \frac{\hbar^2}{2\mu} \left[\frac{\partial^2}{\partial \rho^2} - \frac{1}{\rho} \frac{\partial}{\partial \rho} + \frac{1}{\rho^2} \right].$$

The center of mass motion along the QW layer is expressed by the analytical part of the original SE wave function, whereas the relative motion of the electron and the hole is given by the solution of Eq. (2). The studied boundary value problem (BVP) is formed by the equation (2) and the zero boundary conditions at some large values of the modules of the variables. For simplicity, we consider only the s-states, for which $E_\phi = 0$.

Since SE (2) is the standard three-dimensional partial differential equation, the direct numerical solution of the BVP is feasible using available computational facilities. In our study, we use the finite difference approximation of the derivatives in equation (2) due to the sparse and relatively simple form of the matrix equation. We employ the central fourth order finite difference formulas for the first and second derivatives:

$$\frac{\partial}{\partial z_e} \Psi \rightarrow \frac{\Psi_{-2} - 8\Psi_{-1} + 8\Psi_1 - \Psi_2}{12h},$$

$$\frac{\partial^2}{\partial z_e^2} \Psi \rightarrow \frac{-\Psi_{-2} + 16\Psi_{-1} - 30\Psi_0 + 16\Psi_1 - \Psi_2}{12h^2}.$$

as well as non-central differences at the equidistant grid with the step h . They define the uncertainty of the numerical solution of the order of h^4 . The exponential decrement of the wave function at large values of variables allows us to define wave function exactly zero beyond some rectangular domain. The size of this domain varies from dozens QW widths (for small widths) down to several QW widths (for large widths). The equidistant grid of the knots has been chosen over each variable. The grid step h has been taken the same for all variables and multiply associated with the QW width. The QW is in the center of the domain over z_e and z_h .

The nonzero solution of the homogeneous matrix equation can be obtained by the diagonalization of the matrix. Due to the large structure of the matrix, only the part of the spectrum can be obtained. Using the Arnoldi algorithm [6], we have calculated the lowest eigenvalue of the matrix and corresponding eigenfunction. As a result, the ground state energy, E_x , and the wave function of SE (2) have been obtained for various widths of QW. The exciton binding energy, R_x , is defined with respect to the energies of the free electron, E_e , and free hole, E_h , in QW by the formula:

$$R_x = E_e + E_h - E_x.$$

Energies E_e and E_h are obtained by solution of the corresponding one-dimensional SE for the electron and hole in the QW [7].

Model parameters and results

We apply the proposed numerical algorithm for solving SE with parameters for the GaAs/Al_{0.3}Ga_{0.7}As QWs, which are more popular in experimental studies. In the calculation, the following model parameters have been used [9]:

$$m_e = 0.0665m_0, m_h = 0.353m_0, \mu = 0.0414m_0, \epsilon = 12.53, \\ V_e = 0.66V_0, V_h = 0.33V_0, V_0 = 1155x + 370x^2 \text{ (meV)}, x = 0.3,$$

where x is the concentration of aluminum in the AlGaAs alloys in QW barriers, m_0 is the free electron mass. The calculations have been carried out for various widths of QW.

The convergence of the ground state energy at some widths of QW as $h \rightarrow 0$ is shown in Fig. 1. The calculated energies are denoted by points. They show the quadratic behavior on h for small h . The extrapolation of the energies to $h = 0$ by a parabolic fit allows us to obtain the precise exciton ground state energy. The uncertainty of such extrapolation is chosen to be the difference between the most precisely calculated energy and the extrapolated one. The typical grid step appropriate for the calculations with QW widths comparable with the Bohr radius is $h = 0.2$ nm.

The calculated exciton binding energy and the extrapolated energy values for various widths together with the correspondent interpolating curves are presented in Fig. 2. The uncertainty bars show the uncertainty estimated from the extrapolation. The figure shows that the maximum energy of 9.66 meV is achieved at the QW width equal to 3 nm. For smaller widths the energy decreases and tends to the binding energy of the three-dimensional exciton.

Additionally, the study of QW with large widths allows us to estimate the free exciton binding energy. From Fig. 2, we can see that, for our case, this energy is $R_x = 4.10 \pm 0.03$ meV that is slightly less than reported in [1]. Further calculations with different parameters will make it possible to compare our results with the results of other authors.

Conclusion

We calculated, to our knowledge, for the first time, the exciton binding energy in QWs of various widths without any prescribed approximations. The results of the high order finite difference calculations show a very good stability and con-

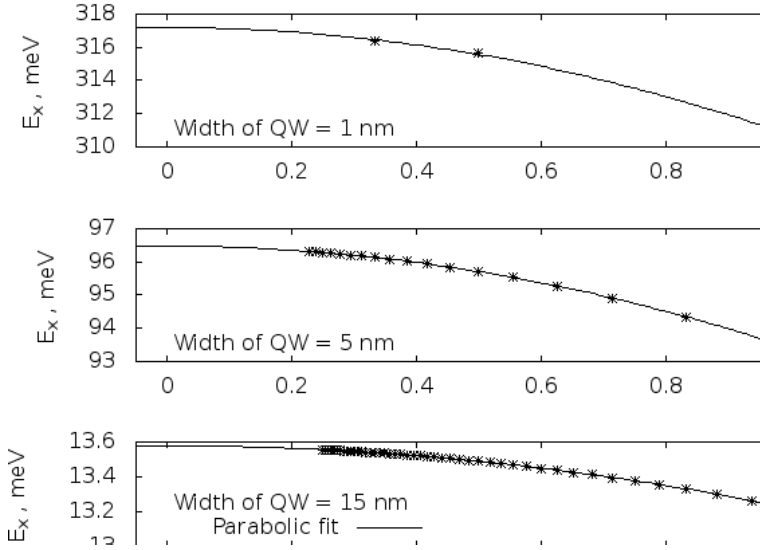


Fig. 1. The calculated exciton ground state energies as a function of the grid step. The parabolic fit which enables the extrapolation of the energy is shown. Various panels correspond to different widths of the quantum well.

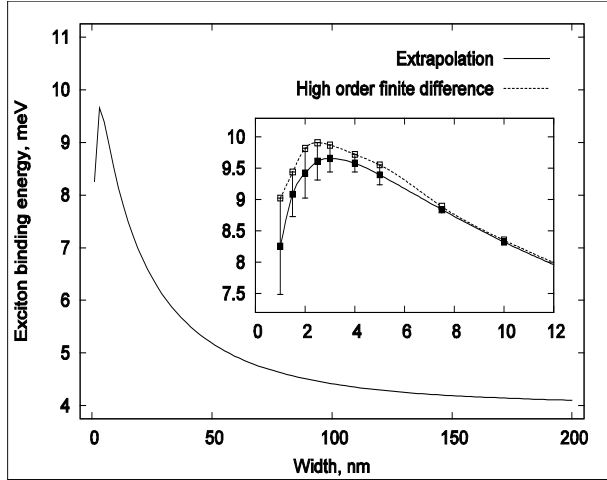


Fig. 2. The exciton binding energy as a function of the width of the quantum well. The inset shows the binding energy for QWs of small widths. The transparent points show the calculated values of energy and the dashed curve interpolates them. The solid points show the extrapolated energies. The solid curve interpolates the solid points. The uncertainties are estimated as the difference between calculated and extrapolated points.

verge as the grid stem goes to zero. The extrapolation of the calculated energies allowed us to obtain the precise exciton binding energy.

References

1. A. Baldereschi, C. Nunzio Lipari // Phys. Rev. B 2, 439 (1971).
2. L.D. Landau and E.M. Livshits. Quantum mechanics. Nonrelativistic theory.- M.: Nauka, 2004.
3. R.L. Greene, K.K. Bajaj, and D.E. Phelps // Phys. Rev. B 29, 1807 (1984).
4. G. Bastard et al. // Phys. Rev. B 26, 1974 (1982).
5. B. Gerlach et al. // Phys. Rev. B 58, 10568 (1998).
6. R. Lehoucq, J.A. Scott, An evaluation of software for computing eigenvalues of sparse nonsymmetric matrices., Preprint MCS-P547-1195, ANL, 1996.
7. J.H. Davies. The physics of low-dimensional semiconductors.- Cambridge University Press, 1998.
8. D. Schiumarini et al. // Phys. Rev. B 82, 075303, (2010).
9. I. Vurgaftman et al. // J. Appl. Phys. 89, 5815 (2001).

E. Applied Physics

Research of consequences of the accidents at nuclear power plants and impact on the environment of Leningrad region

Merzlaya Anastasia
stummeworte@mail.ru

Scientific supervisor: Dr. Torilov S.Yu., Department of Nuclear-Physics Research Methods, Faculty of Physics, Saint-Petersburg State University

Introduction

The most adverse consequences of nuclear power engineering are catastrophes happened at nuclear power plants (NPP) and the distribution of released radionuclides and environmental pollution. As a result of these accidents released radionuclides from discarded nuclear reactor materials spread around the world. For example, after the accidents occurred in the Chernobyl (1986) and the Fukushima (2011) released more than 10 thousand PBq [1]. Residual radiation affects on the level of pollution of the environment of St. Petersburg and Leningrad region.

The purpose and the tasks of work

The aim of the work was study of the influence of radiation precipitation from the accident at the nuclear power plant on radiation contamination of the territory of Saint-Petersburg and Leningrad region on the example of the accident at the Chernobyl NPP and NPP Fukushima.

Tasks of the work:

1. Choose radionuclides, which can identify contamination from each of the two accidents;
2. Investigate the background gamma-spectrum of environment;
3. Optimally choose the environmental object of research for a more detailed analysis;
4. Analyze the studied samples to find out impact of residual radiation from accidents;
5. Determinate impact of the accidents on the environment of the Leningrad region and compare it with the radiation safety rules and norms.

The method of investigation

Soon after the Chernobyl accident the investigation was carried out to notify the pollution of Europe by gamma-spectrometric survey from planes using scintillation detectors. Although this method gives uncertain data of radionuclide activity in the study area, it allows obtaining an overall picture of the contamination. Thus, according to research in the Leningrad region was found ^{137}Cs from Chernobyl accident in Kingisepp and Lomonosov districts with an estimated activity 1–5 Ci/km² [2].

Another method of investigation of the contaminated territories is the collection of samples of some objects of an environment (in this case, topsoil) and measuring them in the laboratory using semiconductor HPGe gamma-detector CANBERRA GC2018, that was surrounded by a lead shield, with the relative efficiency 20% and energy resolution 1.8 KeV at the peak of ^{60}Co 1333 KeV. This method of registration of radioactivity requires a longer time, but gives much more reliable information.

As the calibration source was used one with ^{152}Eu distributed throughout the volume of filler (sand). After measuring its spectrum formulas for the energy and efficiency of the registration were determined (Fig. 1):

$$E = (0,100 \pm 0,001) \cdot \text{Channel}$$

$$\varepsilon(E) = (0,046 \pm 0,003) - (0,059 \pm 0,004) \cdot \ln(E + (-87 \pm 8))$$

where E – energy, Channel – number of the channel, ε – efficiency of the registration.

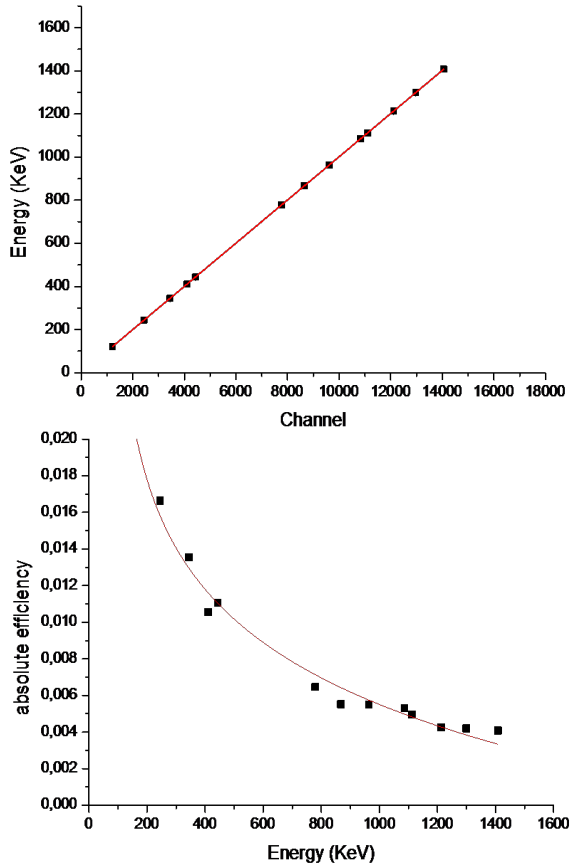


Fig. 1. Graphs of association energy from channel and efficiency from energy.

Spectrum of the background

Measurement of the background in the Old Peterhof (Leningrad region) (Fig. 2) showed that in the spectrum except for the lines of primordial single radionuclides (such as ^{40}K) and radioactive series: uranium (^{238}U with $T_{1/2}=4.47\cdot 10^9$ y), thorium (^{232}Th with $T_{1/2}=1.4\cdot 10^{10}$ y) and uranium-actinium (^{235}U with $T_{1/2}=7.04\cdot 10^8$ y), observed peak of artificial radionuclide ^{137}Cs , which was identified as having the Chernobyl origin according its half-decay period; the peak of ^{134}Cs , which can identify the Fukushima trace, doesn't exceed 0.01 Bq.

The studied radionuclides

Artificial radionuclides can track their movement and accumulation in different environmental objects and can indicate the sources of the pollution. The degree of pollution in the study area is determined by the number of these radionuclides in the environment.

In order to characterize the studied accidents radionuclides, which released in the accidents, were selected. Isotopes of caesium ^{134}Cs and ^{137}Cs is optimally done for the consideration of the impact of accidents on Fukushima and Chernobyl as they have half-decay periods close to the time that past from the moment of the accidents ($T_{1/2}(^{134}\text{Cs})=2$ years, $T_{1/2}(^{137}\text{Cs})=30$ years).

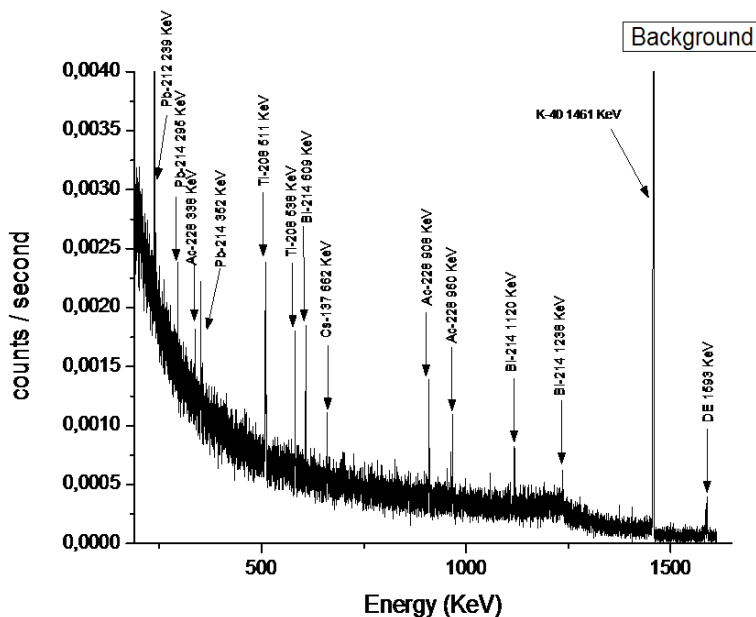


Fig. 2. Gamma-spectrum of the background.

Activity of the radionuclide in sample is determinate as:

$$A = \frac{S - S_B}{t \cdot \varepsilon(E) \cdot p(E)}$$

where time $t=24h=86400s$, S – area of the peak, p - the probability of emission, ε – efficiency of the registration

The observed results

Table 1. Experimental data.

	A (^{137}Cs)(Bq/kg)
Viborg	45±6
Orechvo	11,3±2,9
Svetloe	7,9±1,7
Losevo	290±30
Gruzino	10,3±1,7
Petyayarvi	<0,1
Saint Petersburg	19±3
Universitet	14,3±2,7
Kronshtadt	33±4
Gatchina	13±3
Pavlovsk	1,1±0,6
Sablino	<0,1
Kobralovo	2,4±0,3
Velkoto	120±10
Kotelski	180±20
Luga	430±50

The observed results for ^{137}Cs presented in Table 1. Samples in the polluted zones according to the old map have ^{137}Cs activity of about 200 Bq/kg, however, some places outside of the contaminated areas were detected with radioactivity of ^{137}Cs more than 400 Bq/kg. That means that soil analysis showed a significant expansion of the radioactive spots ^{137}Cs .

The radioactivity of ^{134}Cs , which can identify the Fukushima trace, doesn't exceed 0.01 Bq/kg, thus Leningrad region is not appreciably affected by the contamination from Fukushima.

Conclusions

- The Chernobyl accident effected on the pollution of Saint-Petersburg and Leningrad region;
- Samples from the polluted zones according to the old map have ^{137}Cs activity higher than in other places, but some samples from places outside of the contaminated areas were detected with higher radioactivity of ^{137}Cs . So the spots of

contamination after the accident at the Chernobyl NPP is larger than it was established earlier;

- The accident at Fukushima did not have a significant impact on the environment of Leningrad region;
- Comparing radioactivity with the radiation safety norms show that the activity is less than maximum permissible dose (740 Bq/kg) [4];

References

1. J.T. Smith and N.A. Chernobyl – Catastrophe and Consequences. - Beresford. UK, Chichester, Praxis Publishing Ltd., 2005.
2. Leningrad region. Ecological map. SPb, «Discus Media», 2009.
3. A.O. Merzlaya. Migration of the radionuclides from nuclear accidents in the forest ecosystem // Proceedings of the Conference «Science and Progress 2013», SPb, 2013, pp. 16-19.
4. Basic sanitary rules for radiation safety – 99/2010.

Velocity spread in quantum hydrodynamics

Zippa Andrey
andreyzippa@yandex.ru

Scientific supervisor: Prof. Dr. Ivlev L.S., Department of Atmosphere Physics, Faculty of Physics, Saint-Petersburg State University

Wavelength equation

The quantum hydrodynamics as a convenient method for solving the Schrödinger equation has been developed E. Madelung, D. Bohm, T. Takabayasi and others [1–4]. Main feature of this method is definition of quantum velocity

$$\vec{v} = \nabla S / m$$

via phase of wave function

$$\Psi = R \cdot \exp(iS / \hbar).$$

In case of a potential field, 3rd order linear equation for a wave length

$$\lambda = \frac{2\pi\hbar}{mv}$$

a particle can be derived [5]:

$$\frac{d^3\lambda}{dx^3} + \frac{8m}{\hbar^2}(\mathcal{E} - V)\frac{d\lambda}{dx} - \frac{4m}{\hbar^2}\frac{dV}{dx}\lambda = 0,$$

Where \mathcal{E} is total energy, V is classical potential. An electric force affecting the particle is

$$-\frac{dV}{dx} = eE,$$

where E — strength of the field.

Model and method of solution

In this work a bounded constant electric field is considered. According potential is $V = 0$ in the area $x \leq 0$ and $V = -eEx$ in the area $x > 0$ (Fig. 1). Protons with initial velocity enter from the left side in the area of electric field. A general solution of 3rd order linear equation of this kind [6] can be obtained as sum of products of two fundamental solutions of equation

$$\frac{d^2u}{dx^2} + \frac{2m}{\hbar^2}(\mathcal{E} - V)u = 0,$$

So $\lambda = C_1 \cdot u_1^2 + C_2 \cdot u_1 u_2 + C_3 \cdot u_2^2$.

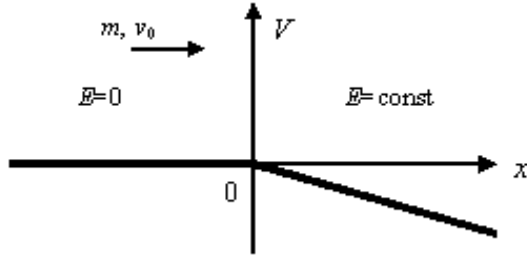


Fig. 1. The model potential.

In our case $\varepsilon = mv_0^2/2$ and the general solution in the area $x > 0$ is expressed via the Airy functions Ai and Bi :

$$\begin{aligned} \lambda(x) = & C_1 \cdot Ai^2 \left[-\left(\frac{2meE}{\hbar^2}\right)^{1/3} \cdot x - \left(\frac{2meE}{\hbar^2}\right)^{-2/3} \cdot \frac{m^2 v_0^2}{\hbar^2} \right] + \\ & C_2 \cdot Ai \left[-\left(\frac{2meE}{\hbar^2}\right)^{1/3} \cdot x - \left(\frac{2meE}{\hbar^2}\right)^{-2/3} \cdot \frac{m^2 v_0^2}{\hbar^2} \right] \cdot \\ & Bi \left[-\left(\frac{2meE}{\hbar^2}\right)^{1/3} \cdot x - \left(\frac{2meE}{\hbar^2}\right)^{-2/3} \cdot \frac{m^2 v_0^2}{\hbar^2} \right] + \\ & C_3 \cdot Bi^2 \left[-\left(\frac{2meE}{\hbar^2}\right)^{1/3} \cdot x - \left(\frac{2meE}{\hbar^2}\right)^{-2/3} \cdot \frac{m^2 v_0^2}{\hbar^2} \right]. \end{aligned}$$

Hence quantum velocity is

$$v_{quantum}(x) = \frac{2\pi\hbar}{m\lambda(x)}.$$

In the area $x \leq 0$ wavelength is constant. Coefficients were obtained by stitching of wavelength and its derivatives at $x=0$. Classical velocity is expressed as

$$v_{classic}(x) = \sqrt{\frac{2eE}{m}x + v_0^2}.$$

Results

Using quantum hydrodynamics and classical mechanics, calculations were made (Fig. 2–4) for protons (mass m , charge e) with initial velocity $v_0 = 450$ km/s (mean one of the solar wind, energy ~ 5 keV) and $v_0 = 10000$ km/s (energy ~ 500 keV) passing through homogeneous electric field of strength $|E| = 130$ V/m, like the natural electric field of the Earth. The velocity spread is the difference of the quantum and classical velocities

$$v_{quantum}(x) - v_{classic}(x).$$

At first glance $v_{quantum}(x)$ is identical with $v_{classic}(x)$ (Fig. 2). However two unusual features have appeared (Fig. 3, 4): 1) splitting up quantum and classical velocity

components, besides over-moderation (Fig. 3) or over-acceleration (Fig. 4) can take place; 2) spread, or dispersion (similar to thermal noise), of velocity which increases with distance.

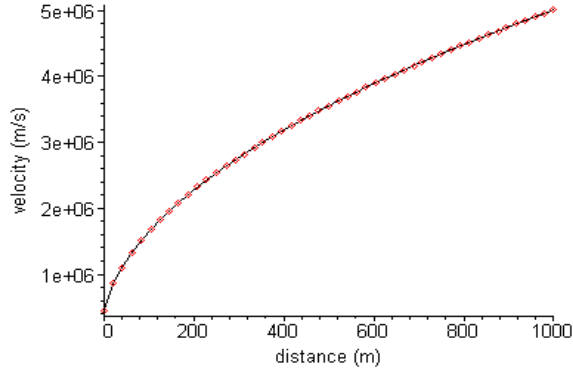


Fig. 2. Movement of the protons in the homogeneous electric field: velocity of protons in quantum hydrodynamics (points) and classical mechanics (line).

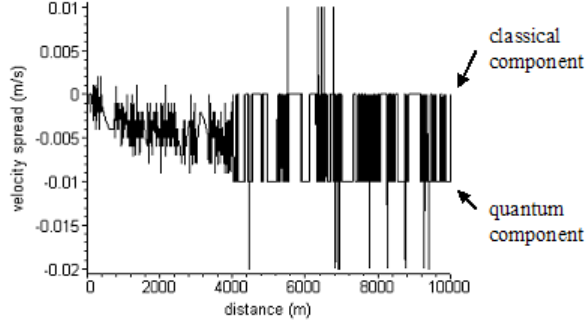


Fig. 3. Velocity spread of protons in the homogeneous electric field. Initial velocity 450 km/s (~ 5 keV).

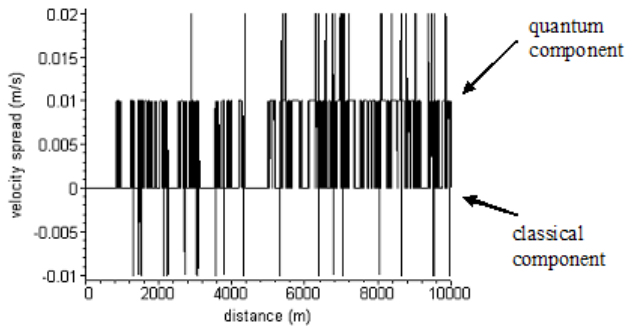


Fig. 4. Velocity spread of protons in the homogeneous electric field. Initial velocity 10000 km/s (~ 500 keV).

References

1. Madelung E. // Z. Phys., Bd. 40, H. 3–4, pp. 322–326 (1927).
2. Bohm D. // Phys. Rev., vol. 85, N 2, pp. 166–179 (1952).
3. Takabayasi T. // Prog. Theor. Phys., vol. 8, № 2, pp. 143–182 (1952).
4. Wyatt R. Quantum dynamics with trajectories: introduction to quantum hydrodynamics. – New York: Springer, 2005, – 428 pp.
5. Zipa A.I. // Vestnik SPbGU (in Russian), ser. 4, № 3, pp. 21–26 (2011).
6. Kamke E. Differentialgleichungen. I. Gewöhnliche Differentialgleichungen. – Leipzig: Teubner, 1983, – 670 p.

G. Theoretical, Mathematical and Computational Physics

Special splints and their types

Kakin Polina
megachi@yandex.ru

Scientific supervisor: Prof. Dr. Lyakhovsky V.D., Department of High Energy and Elementary Particles Physics, Faculty of Physics, Saint-Petersburg State University

Introduction

Since the term "splint" was introduced by D. Richter [1] in relation to classical root systems the attempts were made to apply it to other types of algebraic objects with varying degrees of success [2, 3]. Being a new tool of the representation theory splint allows to simplify calculation of some relations [4] while also yielding the new ones [2]. Thus generalization of splint continues to be a relevant problem.

In the present work injection fan reduction technique and "special" properties of special subalgebras are used to define splint in the case of special embedding. Decomposition of the main algebra's singular element into combination of "stem's" singular elements is found and used to study properties of the new splints. Discovered special splints are studied and organized into several types. Among them the types that allow to simplify calculation of branching rules are found. To study splints where one of the stems does not have the properties of a root system new definition of singular element is suggested and together with the injection fan extension it might serve as a base for representation theory for such systems.

Methods, Results and Discussion

A root system Δ_g of algebra g is said to be splintered if it is a disjoint union of the images of two root systems regularly embedded into it. These embedded root systems are called stems. If a - the algebra of one of the stems - is in fact a subalgebra of algebra g then the splint is called "injective" [4] and it can be used to simplify calculation of branching coefficients for reduction $g \downarrow a$. Special embedding differs from a regular one in the sense that the embedded root system Δ_a is not a part of the root system Δ_g . This feature at the first glance makes it impossible to define splint in the case of special embedding. However, special subalgebras have some unique qualities [5] that together with injection fan reduction technique and universal method of special embedding construction [6] allows us to successfully redefine splint.

As it turns out [5], if one is to project the root system Δ_g onto special subalgebra root space the resulting projection Δ' will include the subalgebra root system Δ_a and another vector system called Δ_s . Moreover, all vectors of Δ_s will be linear combination of the roots of Δ_a with integer coefficients. These two facts allow us to define special splint as a splint of the projection of a root system: $\Delta' = (\Delta_a, \Delta_s)$. However, stem Δ_s will be a root system only in some cases. This issue can be re-

solved by using injection fan extension on special embeddings: known branching coefficients can be used to find singular elements for such systems.

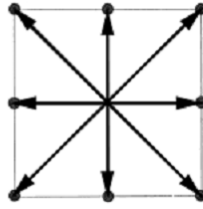
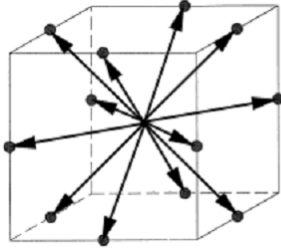


Fig. 1. Root system of algebra A_3 and its projection onto the root space of subalgebra B_2 .

The group of reflections W_s analogues to the Weyl group can also be defined for Δ_s . The group of reflections in hyperplanes orthogonal to the roots from Δ_g that already lie in the root space of special subalgebra will be called W_{inv} . Both of these groups govern the symmetry of singular element of Δ_s and thus define the part of the singular element to which the study can be reduced.

To help the process of finding and studying special splints further the universal method of special embedding construction [6] can be used. The method gives the exact algorithm of constructing special embedding and finding the expression of simple roots of Δ_s via roots of Δ_g which simplifies the process of projecting one root system onto the root space of another.

As one can regard singular element as a polyhedron with edges parallel to the algebra roots, relations between W_a , W_s and W_{inv} define the behavior of singular elements. Thus, the following propositions can be made:

If in special splint $\Delta' = (\Delta_a, \Delta_s)$, $\Delta_s \subset \Delta_a$ then:

$$\Phi_g^{(\mu)'} = \sum_{\omega \in W_{inv}} \varepsilon(\omega) \omega (1 + \sigma_1 + \dots) (e^{\hat{\mu} + \hat{\rho}_g - \tilde{\mu} - \tilde{\rho}_s} \Phi_s^{(\tilde{\mu})}),$$

where $\Phi_g^{(\mu)'}$ is a singular element of Δ' ; $(1 + \sigma_1 + \dots)$ are elements of W_s which place $\Phi_s^{(\tilde{\mu})}$ into neighboring Weyl chamber of subalgebra a (one needs as many elements as the times Weyl chamber of algebra a can be put into Weyl chamber of W_{inv}); $\varepsilon(\omega)$ is a sign of Weyl group element; $\hat{\mu} + \hat{\rho}_g$ is the longest vector of $\Phi_g^{(\mu)'}$ with positive singular multiplicity.

If in special splint $\Delta' = (\Delta_a, \Delta_s)$, $\Delta_a \subset \Delta_s$ and $W_{inv} \subset \Delta_a$ then:

$$\Phi_g^{(\mu)'} = \sum_{\omega \in W_{inv}} \varepsilon(\omega) \omega (1 + \sigma_1 + \dots) (e^{\hat{\mu} + \hat{\rho}_g - \tilde{\mu} - \tilde{\rho}_s} \Phi_s^{(\tilde{\mu})}),$$

if there is no W_{inv} or $W_{inv} \not\subset \Delta_a$ then:

$$\Phi_g^{(\mu)'} = \sum_{\omega \in W_{inv}} (2 - \sum_{\omega \in W_a} \varepsilon(\omega) \omega) (e^{\hat{\mu} + \hat{\rho}_g - \tilde{\mu} - \tilde{\rho}_s} \Phi_s^{(\tilde{\mu})}).$$

If singular element of the stem s $\Phi_s^{(\tilde{\mu})}$ can be placed into the main Weyl chamber \bar{C}_a of subalgebra a , then the action of injection fan $V_{a \rightarrow g}$ on $\Phi_s^{(\tilde{\mu})}$ will yield:

$$M_{s(\tilde{v})}^{(\tilde{\mu})} = b_{s(\mu - \tilde{\mu} + \tilde{v})}^{(\mu)}.$$

Otherwise,

$$b_{s(\mu - \tilde{\mu} + \tilde{v})}^{(\mu)} = N_{(\tilde{v})},$$

where $M_{s(\tilde{v})}^{(\tilde{\mu})}$ is multiplicity of the weight \tilde{v} of representation of s with the highest weight $\tilde{\mu}$ if Δ_s is a root system; $b_{s(\mu - \tilde{\mu} + \tilde{v})}^{(\mu)}$ is a branching coefficient; $N_{(\tilde{v})}$ is coefficient such as:

$$V_{a \rightarrow g}((1 + \sigma_1 + \dots)(e^{\hat{\mu} + \hat{\rho}_s - \tilde{\mu} - \hat{\rho}_s} \Phi_s^{(\tilde{\mu})})) = \sum_{\tilde{v}} N_{(\tilde{v})} e^{\tilde{\mu}}.$$

In both cases $\tilde{v} \in \bar{C}_a$ and the main Weyl chamber \bar{C}_a should be constructed from the point $\tilde{\mu} - \mu$.

According to these propositions, all special splints can be organized into six types:

Table 1. Types of special splints.

Type	s	$W_a \subset W_s$	$W_s \subset W_a$	W_{inv}	Examples
1	root system	no	yes	yes	$B_2 \rightarrow D_3$, $G_2 \rightarrow B_3$
2	root system	yes	yes	no	$A_1 \rightarrow A_1 + A_1$
3	root system	yes	no	no	$A_1 + A_1 \rightarrow D_3$
4	not a root system	yes	no	yes	$A_1 \rightarrow A_2$, $A_1 \rightarrow B_3$
5	not a root system	yes	no	no	$A_1 \rightarrow B_2$
6	$W_a \not\subset W_s$ and $W_s \not\subset W_a$				$B_2 \rightarrow D_4$

Let's look at some examples:

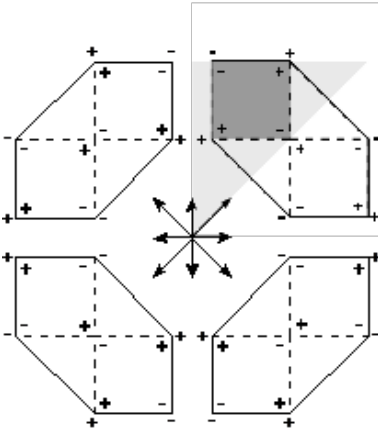


Fig. 2. Splint $D_3 = (B_2, A_1 + A_1)$ of the Type 1: projection of the singular element $\Phi_{D_3}^{((1,1,2))'}$ can be made from singular elements $\Phi_{A_1+A_1}^{((1,1))}$. Light-grey area is the fundamental Weyl chamber of subalgebra B_2 . This splint allows to calculate branching rules more easily.

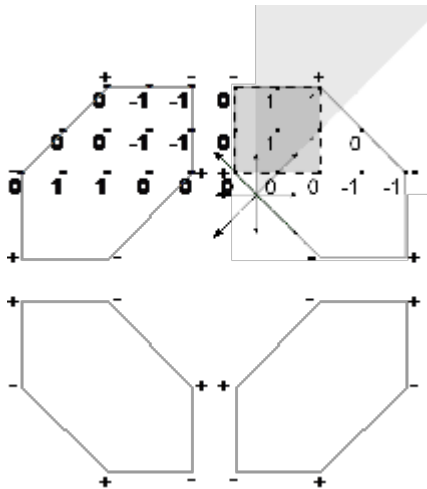


Fig. 3. Action of injection fan on the singular element $\Phi_{A_1+A_1}^{(1,1)}$ yields branching coefficients. The example shows Gelfand-Zetlin rules for branching $so(2n) \rightarrow so(2n+1)$: according to stated propositions branching coefficients $so(5) \rightarrow so(6)$ are equal to weight multiplicities of stem $A_1 + A_1$ representations which are always equal to 1.

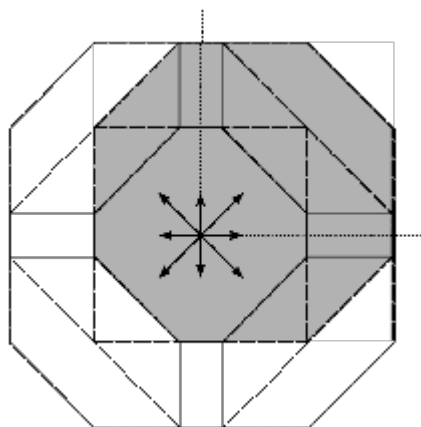


Fig. 4. Splint $D_3 = (A_1 + A_1, B_2)$ of the Type 1: projection of the singular element $\Phi_{D_3}^{(1,1,2)}$ can be made from singular elements $\Phi_{B_2}^{(1,2)}$. Light-grey area is the fundamental Weyl chamber of subalgebra B_2 (one of them is marked with grey colour).

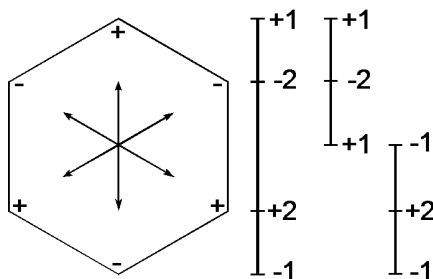


Fig. 5. Splint for embedding $A_1 \rightarrow A_2$ of the Type 4: projection of the singular element $\Phi_{A_2}^{(1,1)}$ can be made from two singular elements $\Phi_{BC_1}^{(ii)}$.

Conclusion

It was found that the concept of splint can be generalized on the case of special embedding and that decomposition of the projection of the singular element of splintered algebra exists for both the case when one of the stems is not a root system and the case when it is. The latter quality is unique for special splints. Calculation of branching coefficients can be simplified for the splints of the first three types.

1. The new definition of singular element for the vector system that is not a root system together with the extension of injection fan might serve as the base for representation theory of such systems.

2. The type of special splints where neither of stems contains the other requires further research.

References

1. D. Richter // J. Geom. 103 (2012), p.103-117.
2. V.D. Lyakhovsky, A.A. Nazarov // Physics of Particles and Nuclei (September 2012), Volume 43, Issue 5, p.676-678.
3. B. Ransingh, K.C. Pati // arXiv:1305.7189v4 (2013).
4. V.D. Lyakhovsky, A.A. Nazarov // Journal of Mathematical Sciences (New York) (2013), 192:1, p. 91–100.
5. E.B. Dynkin // Mat. Sb., N. Ser. 30(72), (1952) p. 349-462.
6. V.D. Lyakhovsky, D.V. Vasilevich. Special injections for Unified Model Building // Preprint L696/86. Leipzig (1986).

Anomalous scaling of passive scalar fields advected by the Navier-Stokes velocity ensemble: Effects of strong compressibility and large-scale anisotropy

Kostenko Mariia
kontramot@mail.ru

Scientific supervisor: Prof. Dr. Antonov N.V., Department of High Energy and Elementary Particles Physics, Faculty of Physics, Saint Petersburg State University

Introduction

In a few past decades, intermittent interest has been attracted to the problem of intermittency and anomalous scaling in fluid turbulence. The phenomenon manifests itself in singular (arguably power-like) behaviour of various statistical quantities as functions of the integral turbulence scales, with infinite sets of independent anomalous exponents [1]. In spite of considerable success, the problem remains essentially open: no regular calculational scheme, based on an underlying dynamical model and reliable perturbation expansion was ever constructed for the anomalous exponents of the turbulent velocity field. A most efficient way to study anomalous scaling is provided by the field theoretic renormalization group (RG) and operator product expansion (OPE). In the RG+OPE scenario of the anomalous scaling in turbulence the singular dependence on the integral scales emerges as a consequence of the existence in the corresponding models of composite fields (“composite operators” in the quantum-field terminology) with negative scaling dimensions; termed as “dangerous operators”.

In the present paper, we adopt the approach [2] where the standard field theoretic RG was applied to the problem of stirred hydrodynamics of a compressible fluid, and the resulting stationary scaling regime was associated with the IR attractive fixed point of the corresponding multiplicatively renormalizable field theoretic model.

Models and results

There are two diffusion-advection models for compressible fluid: density (for example, density of a pollutant) is described by the equation:

$$\partial_t \theta + \partial_i (v_i \theta) = \kappa_0 \partial^2 \theta + f,$$

and tracer (for example, temperature or entropy) is described by:

$$\partial_t \theta + (v_i \partial_i) \theta = \kappa_0 \partial^2 \theta + f,$$

Where k_0 is the molecular diffusivity coefficient, $v(x)$ is the velocity field and $f=f(x)$ is a Gaussian noise with zero mean and given covariance.

$$\langle f(x) f(x') \rangle = \delta(t - t') C(r / L), \quad r = x - x'.$$

The Navier–Stokes equation for a viscid compressible fluid and continuity equation have the forms:

$$\nabla_i v_i = v_0 [\delta_{ik} \partial^2 - \partial_i \partial_k] v_k + \mu_0 \partial_i \partial_k v_k - \partial_i \varphi + f_i,$$

$$\nabla_t \phi = -c_0^2 \partial_i v_i, \text{ where } \phi = c_0^2 \ln(\rho / \bar{\rho}), \nabla_t = \partial_t + \partial_k v_k.$$

In those equations, ρ is the mass density and c_0 is the speed of sound.

The correlation function is:

$$\langle f_i(x) f_j(x') \rangle = \delta(t-t') \int_{k>m} \frac{dk}{(2\pi)^d} D_{ij}^f(k) \exp\{ikx\},$$

$$D_{ij}^f(k) = g_0 v_0^3 k^{4-d-y} \left[P_{ij}^T(k) + \alpha P_{ij}^L(k) \right].$$

All these quantities depend on $x = \{t, \mathbf{x}\}$ with $\mathbf{x} = \{x_i\}$, $i = 1 \dots d$. $\bar{x} = \{x_i\}$, $i = 1 \dots d$ where d is an arbitrary (for generality) dimensionality of space. The constants v_0 and μ_0 are two independent molecular viscosity coefficients, P_{ij}^T and P_{ij}^L are the transversal and longitudinal projectors and g_0 is the coupling constant. Summations over repeated vector indices are always implied.

According to the general theorem, the stochastic problem is equivalent to the field theoretic model of the doubled set of fields. The field theoretic formulation means that various correlation functions and response (Green) functions of the original stochastic problem are represented by functional averages over the full set of fields with weight $e^{S(\Phi)}$, where S is the action functional and Φ is doubled set of fields.

It turns out that our model (with an insignificant addition) is multiplicatively renormalizable.

It is well known that possible IR asymptotic regimes of a renormalizable field theoretic model are associated with IR attractive fixed points of the corresponding RG equations. In our model there is one IR attractive fixed point and it governs the IR asymptotic behaviour of density and tracer models. Using its value, we got critical dimensions for fields θ , θ' :

$$\Delta_\theta = -1 + y/6, \quad \Delta_{\theta'} = d + 1 - y/6,$$

Where θ' is the auxiliary response field. These expressions are exact due to the absence of renormalization of the fields.

The key role in the following will be played by certain composite fields (“composite operators” in quantum-field terminology). A local composite operator is a monomial or polynomial constructed from the primary fields and their finite-order derivatives at a single space-time point $x = \{t, \mathbf{x}\}$.

The simplest case of the operators is:

$$F(x) = \theta^n(x).$$

We calculated their critical dimensions for two cases:
density model:

$$\Delta[\theta^n] = -n + \frac{ny}{6} - \frac{n(n-1)\alpha dy}{6(d-1)} + O(y^2),$$

tracer model:

$$\Delta[\theta^n] = n\Delta_\theta = -n + ny/6 \text{ (exact)}.$$

Then we considered the equal-time pair correlation function of two UV finite quantities $F_{1,2}(x)$ with definite critical dimensions, namely, the correlation function $\theta^n(x)$. By means of operator product expansion one can get the expression for the density field:

$$\langle \theta^p(t, x_1) \theta^k(t, x_2) \rangle = \mu^{-(p+k)} (\mu r)^{-\Delta_p - \Delta_k} (mr)^{\Delta_{p+k}}.$$

It is worth noting that the set of operators θ^n is closed with respect to the fusion in the sense that the leading term in the OPE for the pair correlator of two such operators is given by the operator from the same family with the summed exponent.

Our consideration of effects of the large-scale anisotropy gives quantitative support for Kolmogorov's hypothesis of the local isotropy restoration and appears rather robust, being observed for the real fluid turbulence.

Conclusion

We have studied two models of passive scalar advection: the case of the density of a conserved quantity and the case of a tracer. The advecting velocity field is described by the Navier--Stokes equations for a compressible fluid with an external stirring force. The full stochastic problems can be formulated as field theoretic models. Their inertial-range behavior was studied by means of the OPE; existence of anomalous scaling (singular power-like dependence on the integral scale L) was established.

Thus we removed two important restrictions of the previous treatments of the passive compressible problem: absence of time correlations and Gaussianity of the advecting velocity field. We stress that in contrast to previous studies that combined compressibility with finite correlation time, the present model is manifestly Galilean covariant, and this fact holds in all orders of the perturbation theory. In a few respects, however, the results obtained here are very similar to those obtained earlier for the compressible version of Kraichnan's rapid-change model and the Gaussian model with finite correlation time.

Although the anomalous exponents are independent of the specific choice of the noise, they do depend on the exponent y , the dimension of space d and n the parameter α , that measures the degree of compressibility. In this respect, our results are also similar to those obtained for simpler models. More detailed presentation of our work can be found in [3].

In the following, the combination of the RG techniques and the energy balance equation seems promising. This work remains for the future and is partly in progress.

References

1. U. Frisch. *Turbulence: The Legacy of A. N. Kolmogorov*, Cambridge University Press, Cambridge, 1995.
2. N. V. Antonov, M. Yu. Nalimov and A. A. Udalov // *Theor. Math. Phys.* 110, 305 (1997).
3. N. V. Antonov, M. M. Kostenko // arXiv:1410.1262 (accepted to *Phys. Rev. E*).

Constraint algebra for embedding theory with partial gauge fixing

Semenova Elizaveta
derenovacio@mail.ru

Scientific supervisor: Dr. Paston S.A., Department of High Energy and Elementary Particle Physics, Faculty of Physics, Saint-Petersburg State University

Introduction

Research is focused on the problems related to description of gravitation. We consider a formulation of gravitation theory in which it is supposed that space-time is 4-dimensional surface in 10-dimensional flat space is considered (first this idea was proposed by T. Regge and C. Teitelboim [1]). In this approach, the embedding function of the space-time into the flat 10-dimensional space is an independent variable for description of gravity. Canonical formalism for embedding theory with partial gauge fixing that matches time of the surface and one of the ambient space is developed. The exact form of the first-class constraint algebra is obtained. The results are compared with the constraint algebra for Regge-Teitelboim formulation of gravity [2]. The results obtained will be used for developing the canonical formalism for formulation of gravity as a field theory in the ambient space. In the future, it may help to avoid some problems arising in attempts to quantize the gravity.

The Embedding Theory

The Einstein's General Relativity is a common theory of gravity. It works well for classical physics, however all attempts to construct the quantum theory of gravity have failed. Nearly forty years ago, in 1975 T. Regge and C. Teitelboim suggested a formulation of gravity similar to the formulation of string theory. They assumed that our space-time is a four-dimensional surface in ten-dimensional Minkowski space $R^{1,9}$ with one timelike and nine spacelike dimensions. In this case, the variables describing the gravity are the embedding function of this surface into the ambient space

$$y^a(x^\mu): R^4 \rightarrow R^{1,9}, \quad (1)$$

where $a=0,\dots,9, \mu, \nu\dots=0,1,2,3$. In Regge and Teitelboim's approach, the standard Einstein-Hilbert's action

$$S = \int d^3x \sqrt{-g} R \quad (2)$$

is taken as an action of the theory. In this expression, they replaced the metric with the induced metric expressed in terms of the embedding function

$$g_{\mu\nu} = \partial_\mu y^a \partial_\nu y_a. \quad (3)$$

We will call this formulation of gravity *The Embedding Theory* [1]. Formalism convenient for calculations in the Embedding Theory is described in details in the book [3]. In this approach the equations of motion - the Regge-Teitelboim (R-T) equations

$$G^{\mu\nu} b_{\mu\nu}^a = 0 \quad (4)$$

appear to be more general than the Einstein equations which means that they contain extra solutions. To overcome the problem of extra solutions T. Regge and C. Teitelboim suggested imposing additional constraints - Einstein's constraints,

$$G_{\mu\perp} = 0, \quad (5)$$

where $G_{\mu\perp}$ is the Einstein tensor, and the symbol \perp denotes the direction orthogonal to the constant time surface. While constructing the canonical formalism these constraints are considered similarly to the primary constraints, resulting in a system of eight constraints:

$$\Phi_i = \pi_a e_i^a, \quad (6)$$

$$\Psi^i = -\sqrt{-g} D_k \left(\pi^a \alpha_a^{ik} / \sqrt{-g} \right) + \pi^a e_a^i, \quad (7)$$

$$\Psi^4 = \pi_a w^a, \quad (8)$$

$$\mathcal{H}^0 = \frac{1}{4\sqrt{-g}} \pi^a \alpha_a^{ik} L_{ik,lm}^{-1} \alpha_b^{lm} \pi^b - \sqrt{-g} R. \quad (9)$$

We will call the theory arising from such approach the *Regge-Teitelboim formulation of gravity*, in contrast to the embedding theory.

The embedding theory is not free from problems connected with quantization of gravity. *Foliation theory* [4] could be the next step on the way of solving such problems. This theory deals with many 4-dimentional surfaces each of them describes dynamics of 3-dimentional space in the flat ambient space. These 4-dimentional surfaces pass through each point of $R^{1,N-1}$ space, they neither intersect nor interact. We can say that $R^{1,N-1}$ is foliated on a system of surfaces. All disturbances propagate along the surfaces. Geometry of surfaces corresponds to R-T equations. This theory formulates gravity as a field theory in the flat ambient space. Quantization of such type theory is well known. The coordinates on the surfaces are not introduced, the only time there is, is an external time – time of the ambient space. To construct the canonical formalism for foliation theory we have to consider embedding theory with an additional condition (the partial gauge fixing)

$$y_0 = x_0, \quad (10)$$

that matches time of the surface and time of the ambient space. This consideration is the object of this work.

Canonical formulation

The addition of gauge condition into the action can lead to loss of some motion equations. In this case, we have only nine R-T motion equations (instead of ten (4)):

$$G^{\mu\nu} b_{\mu\nu}^A = 0, \quad (11)$$

where $A=1\dots 9$. It was verified that the tenth equation

$$G^{\mu\nu} b_{\mu\nu}^{(0)} = 0 \quad (12)$$

automatically satisfies due to satisfying of nine equations and presence of coordinate condition. Therefore, our gauge condition does not spoil the theory.

The action under satisfied gauge condition takes the following form, with explicitly defined dependence on the time derivatives:

$$S = \int dx \frac{1}{2} \left(\frac{\dot{y}^A B_{AB} \dot{y}^B}{\sqrt{1 + \dot{y}^A \overset{3}{\Pi}_{\perp AB} \dot{y}^B}} + \sqrt{1 + \dot{y}^A \overset{3}{\Pi}_{\perp AB} \dot{y}^B} \overset{3}{B}_D^D \right). \quad (13)$$

The gauge fixing leads to reducing the number of constraints by one. Now there are eight constraints:

$$\Phi_i = \pi_A e_i^A, \quad (14)$$

$$\mathcal{H}^0 = \frac{1}{4\sqrt{-g}} \overset{3}{b}^{-1}{}^A{}_{ik} \pi^A L_{ik,lm}^{-1} \overset{3}{b}^{-1}{}^B{}_{lm} \pi^B - \sqrt{-g} \overset{3}{b}{}^A{}_{ik} \overset{3}{b}{}^B{}_{lm} \eta_{DA} L^{ik,lm}, \quad (15)$$

$$\mathcal{H}^i = -\sqrt{-g} \overset{3}{\nabla}_k \left(\frac{1}{\sqrt{-g}} \overset{3}{b}^{-1}{}^A{}_{ik} \pi_A \right). \quad (16)$$

Constraint algebra

It is convenient to use a linear combination:

$$\Psi^k = \mathcal{H}^k + \Phi_i \xi^{ik}, \quad (17)$$

instead of the constraint (16). In addition, it is convenient to deal with convolution of constraints and arbitrary functions:

$$\Phi_\xi \equiv \int d^3x \Phi_i(x) \xi^i(x), \quad (18)$$

$$\mathcal{H}_\xi^0 \equiv \int d^3x \mathcal{H}^0(x) \xi(x), \quad (19)$$

$$\Psi_\xi = \int d^3x \Psi^k(x) \xi_k(x). \quad (20)$$

It simplifies expressions and leads to laconic form of results.

First, we find a geometrical meaning of three constraints Φ^i . For this purpose, we calculate their action on variables. It is easy to find that

$$\{\Phi_\xi, y^A(x)\} = \xi^i(x) \partial_i y^A(x), \quad (21)$$

$$\left\{ \Phi_\xi, \frac{\pi_A(x)}{\sqrt{-g(x)}} \right\} = \xi^i(x) \partial_i \frac{\pi_A(x)}{\sqrt{-g(x)}}. \quad (22)$$

It means that Φ_ξ generates a transformation $x^i \rightarrow x^i + \xi^i(x)$ of 3-dimensional coordinates on the constant-time surface W^3 (it should be noted that generalized

momentum π^a is a three-dimensional scalar density). Because all constraints are covariant (in three-dimensional meaning) equalities, we can write the action of constraints Φ_i on them:

$$\{\Phi_\xi, \Phi_\zeta\} = -\int d^3x \Phi_k \left(\xi^i \overset{3}{\nabla}_i \zeta^k - \zeta^i \overset{3}{\nabla}_i \xi^k \right), \quad (23)$$

$$\{\Phi_\xi, \Psi_\zeta\} = -\int d^3x \Psi^k \left(\xi^i \overset{3}{\nabla}_i \zeta_k + \zeta_i \overset{3}{\nabla}_k \xi^i \right), \quad (24)$$

$$\{\Phi_\xi, \mathcal{H}_\zeta^0\} = -\int d^3x \mathcal{H}^0 \xi^i \partial_i \zeta. \quad (25)$$

Now we find a geometrical meaning of four constraints Ψ^k . It is easy to verify that

$$\left\{ \Psi_\xi, \overset{3}{g}_{ik}(x) \right\} = 0, \quad (26)$$

so the constraints Ψ^k generate transformations which are an isometric bending of the surface W^3 . After tedious calculations, we get the exact result of the action of constraints Ψ^k on other constraints:

$$\{\Psi_\xi, \Psi_\zeta\} = \int d^3x \left(\Psi^i r_{\xi A}^i \overset{3}{\nabla}_i r_{\zeta A}^A - \Psi^i r_{\zeta A}^i \overset{3}{\nabla}_i r_{\xi A}^A \right), \quad (27)$$

$$\{\Psi_\xi, \mathcal{H}_\zeta^0\} = \int d^3x \left(\Psi^i \overset{3}{\nabla}_i \left(r_{\xi A}^A \pi^B B_{BA}^{-1} \zeta \right) - \Psi^i \left(\overset{3}{\nabla}_i r_{\xi A}^A \right) \pi^B B_{BA}^{-1} \zeta \right), \quad (28)$$

where

$$r_{\xi A}^B = \frac{\delta \Psi_\xi}{\delta \pi_A^B} = b^{-1} \overset{3}{\nabla}_i \xi_k + e^{iB} \xi_i. \quad (29)$$

After another tedious calculation we get:

$$\begin{aligned} \{\mathcal{H}_\xi^0, \mathcal{H}_\zeta^0\} = & \int d^3x \left(- \left(\Psi^l - g^{lm} \Phi_m \right) \left(\xi \overset{3}{\nabla}_l \zeta - \zeta \overset{3}{\nabla}_l \xi \right) + \right. \\ & \left. + \Psi^k \left(\pi^B B_{BA}^{-1} \xi \overset{3}{\nabla}_k \left(\pi^C B_C^{-1A} \zeta \right) - \pi^B B_{BA}^{-1} \zeta \overset{3}{\nabla}_k \left(\pi^C B_C^{-1A} \xi \right) \right) \right). \end{aligned} \quad (30)$$

Formulas (23), (24), (25), (27), (28), (30) give the exact form of the first-class constraint algebra for the Embedding Theory with partial gauge fixing.

Another approach

We can fix the gauge by introducing it as an additional condition $\chi = y^0 - x^0 = 0$ not in the action but in the canonical formalism,

$$\{\Psi^4, \chi\} = \int d^3x \frac{\delta \pi_a w^a}{\delta \pi_b} \frac{\delta}{\delta y^b} (y^0 - x^0) = w^0 \neq 0, \quad (31)$$

therefore, we express a pair of variables $y^0 = x^0$, π_0 . As a result, eight constraints of Regge-Teitelboim formulation of gravity turn into seven constraints of the formulation with a partial gauge fixing, so does the constraint algebra.

This suggests that in the case of the imposition of additional Einstein's constraints, canonical formalism of the theory with respect to the time of the ambient

space (i.e., the partial gauge fixing in action) is equivalent to the canonical description of the theory with respect to the time of the surface.

Conclusion

Canonical formalism for embedding theory with partial gauge fixing that match time of the surface and time of the space has been build. The exact fom of the first class constraint algebra for the embedding theory with the partial gauge fixing has been obtained. The constraint algebra for embedding theory with partial gauge fixing has been compared with one obtained without it. The results obtained will be used for developing the canonical formalism for formulation of gravity as a field theory in the ambient space [4]. It may help to avoid some problems arising in attempts to quantize the gravity.

References

1. Regge T., Teitelboim C. Proceedings of the First Marcel Grossmann Meeting, Trieste, Italy, 1975. Ed.R.Ruffini, North Holland, Amsterdam, 1977. p.77.
2. S.A. Paston, A.S .Semenova // Int. J. Theor. Phys., v.49, № 11, pp. 2648-2658 (2010), arXiv:1003.0172
3. Пастон С.А. Гравитация как теория вложения. – Saarbrucken: LAMBERT Academic Publishing, 2012. - 138 с.
4. S.A. Paston // Theor. Math. Phys., v.169, № 2, pp. 1611-1619 (2011), arXiv:1111.1104

Dynamics of triple asteroids

Timoshenko Vladimir
vladimir.timoshenko7@gmail.com

Scientific supervisor: Prof. Dr. Orlov V.V., Department of Celestial Mechanics, Faculty of Mathematics and Mechanics, Saint-Petersburg State University

Introduction

By virtue of high-precision observations, lately a new class of objects in the Solar System – triple asteroids – was discovered, which are described in terms of Newtonian three-body problem. The first triple asteroids were discovered about ten years ago. At that moment about dozen of such objects are known. The studies of this class of objects will improve the understanding of evolution of the Solar System.

In our research, we have examined five triple asteroids, which are known for all orbital characteristics and masses of the components. We have determined the stability of these systems using analytical stability criterion and studied their dynamic evolution over time by numerical experiments.

Observed triple asteroids and their characteristics

We have used the results of observations of several triple asteroids [1]. Data for these systems are given in Table 1. The Table shows that the central body mass is larger than those of companions by a few orders of magnitude. The eccentricities are close to zero; therefore the orbits are almost circular. The largest mutual inclination belongs to Eugenia, and it is about 20° . As for the periods, they are of a few days. Periods of satellites in the same system are comparable (the maximum difference of nine times is in the system Sn263).

Table 1. Masses of the components and orbital characteristics for triple asteroids under consideration obtained using observation data.

System	$m_0, \text{ kg}$	$m_1, \text{ kg}$	$m_2, \text{ kg}$	$a_1, \text{ km}$	$a_2, \text{ km}$	e_1	e_2	$I_{\text{mut}}, ^\circ$	$P_1, \text{ days}$	$P_2, \text{ days}$
Eugenia	5.63×10^{18}	2.51×10^{14}	2.51×10^{14}	610.8	1165	0.069	0.006	20.5	1.79	4.71
Sylvia	1.48×10^{19}	7.33×10^{14}	9.32×10^{14}	706.5	1357	0.027	0.0055	0.56	1.37	3.65
Haumea	4.01×10^{21}	1.79×10^{18}	1.79×10^{19}	25657	49880	0.249	0.0513	13.4	18.3	49.4
Sn263	917×10^{10}	9.77×10^{10}	24.0×10^{10}	3.804	16.63	0.016	0.015	13.9	0.69	6.22
1994 CC	25.9×10^{10}	0.58×10^{10}	0.09×10^{10}	1.729	6.130	0.002	0.192	15.7	1.24	8.37

Golubev criterion of stability

The first stability criterion for the restricted three-body problem was obtained by George Hill in 1878. In 1967, Valentin Golubev [2] has analytically generalized Hill's criterion for the general problem of three bodies. Golubev has shown that if a triple system has the dimensionless parameter

$$s = \frac{c^2 H}{G^2 \bar{M}^5},$$

that is larger than a certain critical value s_c then the system remains stable, i.e. an exchange of the components is prohibited, otherwise triple system can change its structure [3]. Here c and H are angular momentum and total energy of the triple system; \bar{M} is the average mass of three bodies, G is gravitational constant. The value s_c is determined by the masses.

The use of the Golubev criterion to the analysed triple asteroids shows that they are stable (see table 2).

Table 2. The stability parameters and their critical values.

System	s	s_c
Eugenia	7.40×10^{-13}	7.10×10^{-13}
Sylvia	1.52×10^{-12}	1.42×10^{-12}
Haumea	1.18×10^{-7}	1.17×10^{-7}
Sn263	1.67×10^{-5}	1.55×10^{-5}
1994 CC	5.93×10^{-5}	4.45×10^{-5}

Numerical simulations of dynamical evolution

The main part of our work was devoted to a numerical model construction of the three-body system in order to calculate the trajectories for long times, about 10^6 orbital periods of satellites ($\sim 10^4$ years).

Using the data from Table 1, the initial coordinates and velocities of three bodies were calculated in the reference frame associated with the centre of mass of the triple system. Differential equations of the motion of bodies were integrated numerically by the fourth-order Runge-Kutta method with automatic step choice. The calculations were checked by conservation of the integrals of motion (the energy integral error to the end of calculations was $\sim 10^{-8}$, other integrals were conserved with much better accuracy). The ability to get the quantities of interest at any step of numerical integration was also implemented.

Fig. 1 shows the dependences on time for parameters of the triple asteroid Eugenia. The plots show an absence of secular evolution that confirms the stability of the system. Similar dependences for other asteroids take place.

Next, let's consider in detail a nature of variations in the semi-major axes and eccentricities of the satellite orbits. These dependences are also shown for the system Evgenia (Fig. 2). The graph shows that the semi-major axes oscillate with a period comparable to the orbital periods of satellites. The eccentricities along with fluctuations indicate certain trends. We assume that this phenomenon may be due to the well-known Lidov-Kozai effect [4, 5] that will be studied below.

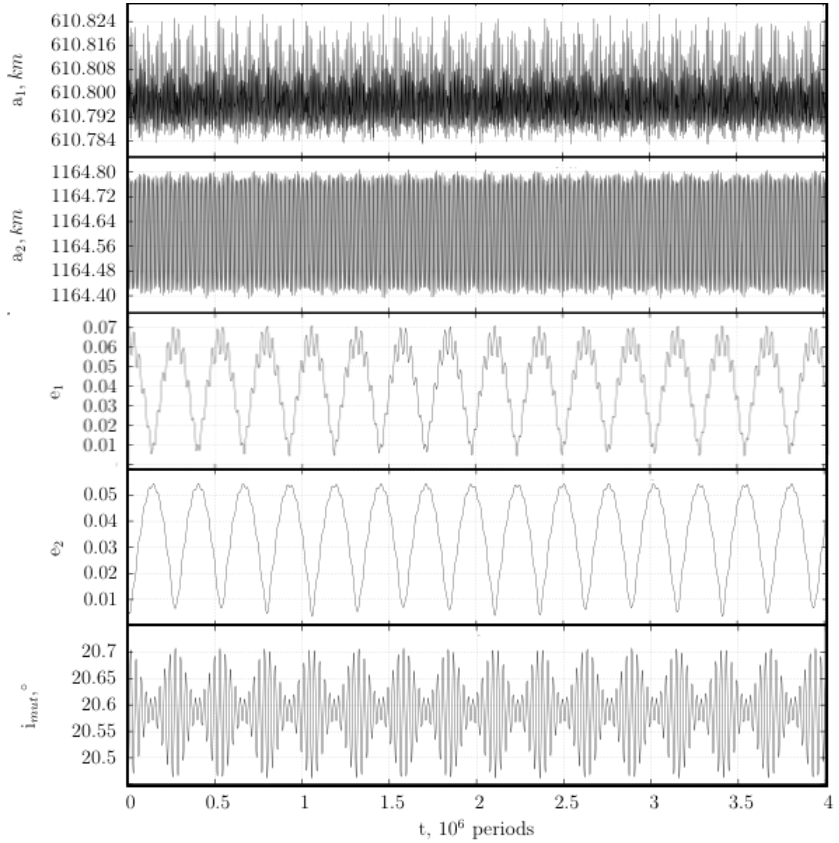


Fig. 1. The time dependences of orbital parameters for triple asteroid Eugenia.

The Lidov-Kozai effect refers to periodic changes of inner binary eccentricity and mutual inclination of binaries orbits in a triple hierarchical system. This mechanism may lead to a strong grow of inner orbit eccentricity with a large mutual inclination. For example, Lidov showed that if the lun0ar orbit inclination to the ecliptic plane had been 90° then the eccentricity of its orbit would increase so rapidly that the Moon falls to the Earth in four years!

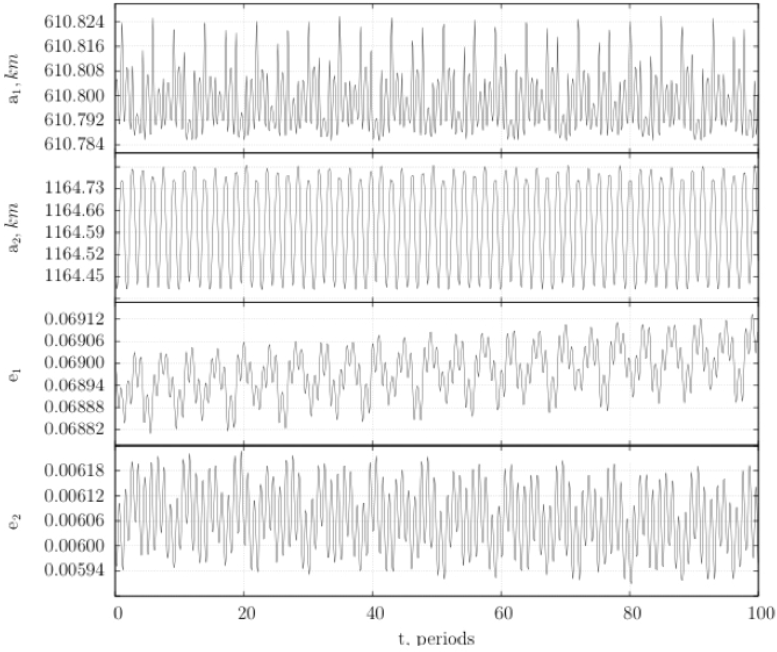


Fig. 2. Dependences of orbital parameters for the asteroid Eugenia during a short time. Similar behavior was observed for the other studied objects too.

The eccentricity e of inner binary and mutual inclination i change simultaneously and are connected by Kozai quasi-integral that also contains the semi-major axis a of inner orbit [6]:

$$H_{Koz} = \sqrt{a(1 - e^2)} \cos i.$$

This value varies cyclically with small amplitude. The formula shows that the inclination increases when the eccentricity decreases and vice versa. The period of that exchange is called the Lidov-Kozai cycle, and it is determined by the following approximate expression:

$$\tau_{Koz} = \frac{2}{3\pi} \frac{P_{ex}^2}{P_{in}} (1 - e_{ex}^2)^{3/2} \frac{M}{m_{ex}}.$$

Here P_{ex} , e_{ex} , m_{ex} are the orbital period, eccentricity and mass of the outer body, which causes a perturbation of the body in an orbit with the period P_{in} ; M is the total mass of all three bodies.

For considered asteroids the assumption that this phenomenon exists was correct. Numerical simulations for the time equals to the Lidov-Kozai cycle show synchronous periodic changes in eccentricity and mutual inclination. Below we show the dependencies which illustrate the Lidov-Kozai effect for Eugenia (Fig. 3).

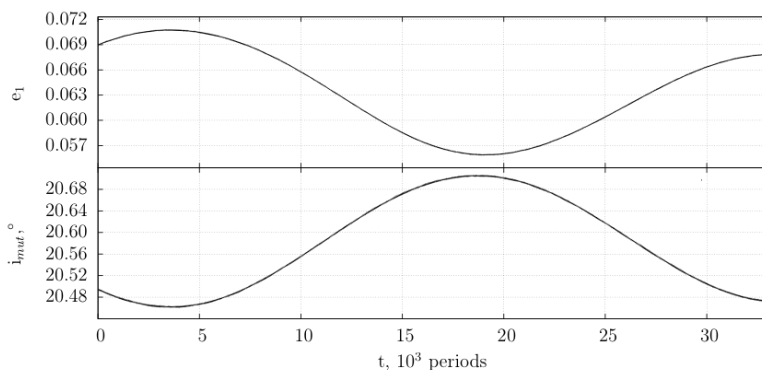


Fig. 3. The Lidov-Kozai effect for the asteroid Eugenia. Integration time is equal to the Lidov-Kozai cycle.

Conclusions

We can make the following conclusions:

- 1) Considered triple asteroids are stable according to the Golubev criterion.
- 2) At large times, the orbital elements of the triple asteroids experience quasi-periodic oscillations. The main conclusion of the numerical simulations is that the stability of the systems during long-term intervals takes place.
- 3) The Lidov-Kozai effect is observed for the system Eugenia. For the rest, it is weaker or at all not evident.

References

1. Liu X. et al. // Mon. Not. R. Astron. Soc. 427, pp. 1034–1042 (2012).
2. Golubev V.G. // Doklady Akad. Nauk SSSR 174, p. 767 (1967) (in Russian).
3. Golubev V.G., Grebenikov E.A. The three-body problem in celestial mechanics (In Russian). – Moscow: Moscow Univ. Press, 1985, – 240 pp.
4. Lidov M. L. // Planetary and Space Sci. 8, pp. 5–45 (1962).
5. Kozai Y. // Astron. J. 67, pp. 591–598 (1962).
6. Verrier P.E., Evans N.W. // Mon. Not. R. Astron. Soc. 394, pp. 1721–1726 (2009).

Sensitivity of Tunneling-Rotational Transitions in Ethylene Glycol to Variation of Electron-to-Proton Mass Ratio

Viatkina Anna
anna.viatkine@gmail.com

**Scientific supervisor: Dr. Kozlov M.G., Petersburg Nuclear Physics
Institute**

In the modern theory fundamental constants are parameters of the Standard model that are considered unchanging over time and space. But since their exact values cannot be calculated within the Standard model, it is natural to question their invariability. There exist multiple theories with those parameters varying. They connect the drift of constants with the existence of additional dimensions in space [1], or the different local density of matter around the Universe (Chameleon theories) [2, 3], or with some global scalar field [4, 5]. Testing these models can lead to deeper understanding of physics.

Molecular spectra can be used to study variation of μ – electron-to-proton mass ratio [6, 7]. In the focus of our work is the tunneling-rotational spectrum of ethylene glycol $\text{HO}-\text{CH}_2-\text{CH}_2-\text{OH}$. It has been observed in the interstellar medium [8, 9] and in the comet C/1995 O1 (Hale-Bopp) [10].

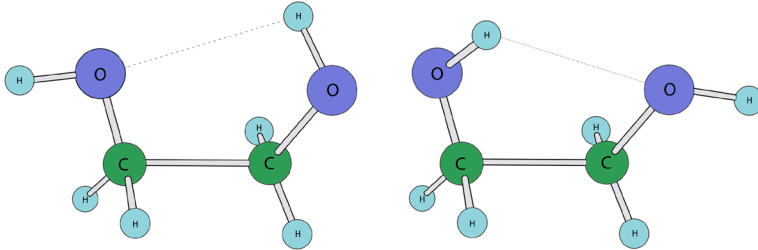


Fig. 1. Schematic molecules of ethylene glycol in two degenerate states of the conformation g' Ga.

Sensitivity coefficients

Let ω be a present-day experimentally observed transition frequency and ω' a frequency shifted due to possible time (and space) change of μ . This shift $\Delta\omega = \omega - \omega'$ is linked to the change $\Delta\mu$ through sensitivity coefficient Q_μ :

$$\frac{\Delta\omega}{\omega} = Q_\mu \frac{\Delta\mu}{\mu} \quad \Delta\mu = \tilde{\mu} - \mu, \quad |\Delta\mu/\mu| \ll 1.$$

Effective Hamiltonian

Ethylene glycol molecule has several conformations, which correspond to the local minima of the potential. The lowest conformation is labeled as g'Ga and is twofold degenerate [11] (see Fig. 1). Tunneling motion between two configurations of the g'Ga conformation lifts degeneracy and causes 7 GHz energy splitting of the ground state. Our main goal is to calculate sensitivity coefficients for the tunneling-rotational transitions. Therefore we need to define how the parameters of the effective Hamiltonian depend on the electron-to-proton mass ratio μ . We found that reasonable accuracy for the tunneling-rotational spectrum is provided by the 14 parameter Hamiltonian (ξ, η, ζ – molecular frame):

$$H_{\text{eff}} = C J_{\xi}^2 + B J_{\eta}^2 + A J_{\zeta}^2 \quad (1)$$

$$- \Delta_J \mathbf{J}^4 - \Delta_K J_{\zeta}^4 - \Delta_{JK} \mathbf{J}^2 J_{\zeta}^2 \quad (2)$$

$$+ d_1 \mathbf{J}^2 (J_+^2 + J_-^2) + d_2 (J_+^4 + J_-^4) \quad (3)$$

$$- \frac{\tau}{2} (F - W_C J_{\xi}^2 - W_B J_{\eta}^2 - W_A J_{\zeta}^2) \quad (4)$$

$$+ [d_3 J_{\zeta} + d_4 (J_+ + J_-)] \delta_{\tau', -\tau}. \quad (5)$$

Rotational constants are $A \gg B \approx C$, so we can use basis set $|J, K_A\rangle$ for prolate top with $K_A \equiv \langle J_{\zeta} \rangle$.

(1) is asymmetric top rotation

$$A, B, C \sim 1/I \sim 1/MR^2$$

(2), (3) are diagonal and non-diagonal in K_A centrifugal corrections

$$\Delta_J, \Delta_K, \Delta_{JK}, d_1, d_2, d_3 \sim \mu^2$$

(4) describes tunneling degree of freedom, $\tau = -1, 1$ is tunneling number, F is tunneling frequency, W_i are centrifugal corrections to the tunneling frequency:

$$F \sim \mu^{4.1}, W_i \sim \mu^{5.1}$$

(5) d_3, d_4 show Coriolis interaction between rotation and tunneling motion.

$$d_3, d_4 \sim \mu^{5.1}$$

Numerical results

We fit 14 parameters of the Hamiltonian to the experimental transition frequencies from [11], so that the *rms* (root-mean-square) deviation of modeled frequency from the measured one is minimal. We use simplex method to obtain *rms* error of 0.3 MHz and the maximum deviation of 1.3 MHz.

We diagonalize the H_{eff} matrix for several sets of parameters, which correspond to different values of μ , to determine the sensitivities q for the energy levels and then the coefficients $Q_{\mu}(\omega) = (q - q')/\omega$ for each transition.

Table I. Predicted low-frequency tunneling-rotational transitions and their sensitivity coefficients Q_μ . Frequencies ω are in MHz, wavelengths λ in cm. Tunneling number $v = 0, 1$ is connected with $\tau = -1, 1$ through $v = (1 - \tau)/2$. Quantum numbers $J_{KA, KC}$, where $K_A \equiv \langle J_\zeta \rangle$. Frequencies from “The Cologne database for Molecular Spectroscopy” are in boldface.

J	K_A	K_C	v	J'	K'_A	K'_C	v'	ω	λ	Q_μ
3	1	3	0	3	0	3	1	882.2	34.0	-16.5(58)
1	1	0	0	1	1	1	0	966.4	31.0	0.9(1)
4	0	4	1	4	1	4	0	978.3	30.6	17.8(38)
4	2	2	0	4	2	3	0	1000.9	30.0	0.95(1)
3	1	3	1	3	1	2	0	1181.6	25.4	17.9(26)
2	1	2	0	2	0	2	1	1957.9	15.3	-9.3(16)
3	3	1	0	4	2	2	1	2641.3	11.4	-6.9(12)
3	1	2	0	2	2	1	0	2653.8	11.3	1.2(2)
3	1	2	1	2	2	1	1	2682.2	11.2	0.98(2)
4	1	3	0	4	1	4	1	2815.2	10.7	-6.2(11)
1	1	1	0	1	0	1	1	2828.6	10.6	-6.3(12)
2	1	1	0	2	1	2	0	2892.1	10.4	0.9(1)
1	0	1	0	0	0	0	1	3243.2	9.2	-5.4(10)
2	0	2	0	1	1	1	1	3598.8	8.3	-4.8(9)
1	1	0	0	1	0	1	1	3795.0	7.9	-4.5(9)
2	1	2	1	2	1	1	0	4043.9	7.4	6.2(8)
2	2	1	1	3	1	2	0	4303.7	7.0	5.8(7)
2	1	1	0	2	0	2	1	4850.0	6.2	-3.2(7)
3	1	2	0	3	1	3	0	5703.3	5.3	0.6(5)
4	2	3	1	4	2	2	0	5938.8	5.0	4.5(5)
1	1	1	1	1	1	0	0	5986.6	5.0	4.5(5)
4	1	4	0	4	0	4	0	6107.3	4.9	1.4(3)
3	1	2	0	3	0	3	1	6585.5	4.6	-1.7(4)
3	2	2	1	3	2	1	0	6611.0	4.5	4.2(5)

Table II. We found out that some of predicted low-frequency transitions are listed in “The Cologne Database for Molecular Spectroscopy”. The agreement is within error of $\Delta\omega = 0.5$ MHz.

J	K_A	K_C	v	J'	K'_A	K'_C	v'	ω_{theor}	ω_{Cologne}	$\Delta\omega_{\text{Cologne}}$	Q_μ
1	0	1	0	0	0	0	1	3243.2	3243.4	0.0011	-5.4(10)
2	1	2	1	2	1	1	0	4043.9	4043.9	0.0011	6.2(8)
1	1	1	1	1	1	0	0	5986.6	5986.6	0.0011	4.5(5)
3	2	2	1	3	2	1	0	6611.0	6611.4	0.001	4.2(5)

Conclusion

Low-frequency transitions with high Q_μ of both signs were found:

$$\omega_1 = 1181.6 \text{ MHz} : Q_{\mu 1} = 17.9(26)$$

$$\omega_1 = 882.2 \text{ MHz} : Q_{\mu 2} = -16.5(58)$$

$Q_{\mu 1} - Q_{\mu 2} \approx 34$ – the big difference is convenient for ruling out the systematic error in the experiment.

Observation of the ethylene glycol spectrum from extragalactic sources can give us new information about the time-drift of μ . Spectral lines from cold molecular clouds in the Milky Way can be very narrow allowing for high precision spectroscopy. This can be used to study possible dependence of μ on the local matter density, which is predicted by models with chameleon scalar fields.

References

1. T. Damour // Class. Quant. Gravity 29 (2012) 184001.
2. J. Khoury, A. Weltman // Phys. Rev. Lett. 93 (2004) 171104.
3. K.A. Olive, M. Pospelov // Phys. Rev. D77 (2008) 043524.
4. J.D. Barrow, S.Z.W. Lip // Phys. Rev. D 85 (2012) 023514.
5. J.-P. Uzan // Liv. Rev. Relat. 14 (2011) 2.
6. M.P. Savedoff // Nature 178 (1956) 688.
7. R.I. Thompson // Astrophys. Lett. 16 (1975) 3.
8. J.M. Hollis, F.J. Lovas et al. // Astrophys. J. 571 (2002) L59.
9. M.A. Requena-Torres, J. Martín-Pintado et al. // Astrophys. J. 672 (2008) 352.
10. J. Crovisier, D. Bockelée-Morvan et al. // Astron. Astrophys. 418 (2004) L35.
11. D. Christen, L.H. Coudert et al. // J. Mol. Spectrosc. 172 (1995) 57.

H. Biophysics

Electro-optical method to study aggregation in aqueous suspensions of SPIONs and SPIONs conjugated with Hsp70

Parr Marina
mparr@mail.ru

Scientific supervisor: Prof. Dr. Vojtylov V.V., Department of Molecular Biophysics, Faculty of Physics, Saint-Petersburg State University

Introduction

Special properties of magnetic nanoparticles (MNPs) open wide opportunities to apply them in clinical diagnostics by MRI methods. Like nanoparticles made of common diamagnetic materials (SiO_2 , ZnO , TiO , CaCO_3), magnetic nanoparticles made of iron oxide possess a surface with high adsorption capacity. However unlike these nanoproducs, magnetic iron oxide nanoparticles have one peculiar property to acquire superparamagnetic state. Due to this state magnetic suspensions of SPIONs (superparamagnetic iron oxide nanoparticles) can be used in magnetic hyperthermia, theranostics [1], drug delivery [2] and in MRI as contrasting agents [3]. Aqueous suspensions of SPIONs have reduced stability due to particle aggregation. The use of surfactants can increase the stability of colloid and slow down coagulation processes. Molecules of dextran on the surface of magnetite particles increase repulsion and partially stabilize the suspension. Binding of proteins to the particle surface usually increases the size of the aggregates, thus decreasing the stability of such systems.

The improvement of stability of MNPs formations for MRI diagnostics based on SPIONs is not possible without the development of rapid and robust techniques of particle aggregation analysis. In the present paper we analyze the possibility of using electro-optical techniques to study aqueous suspensions of magnetite nanoparticles.

Results and Discussion

Systems of two types were prepared for electro-optical study: nonconjugated SPIONs and conjugates of SPIONs with protein Hsp70. SPIONs have been prepared by coprecipitation of water dissolved salts FeCl_3 and FeSO_4 and then were coated with dextran (Sigma-Aldrich Corporation, 9-11 kDa). Before the conjugation of SPIONs with Hsp70, the amination of its dextran coat has been done, using carboxyls of Hsp70 that were activated by water dissolved carbodiimid. Recombinant human heat shock protein Hsp70 was prepared from E. coli transformed with a pMSHsp70 plasmid. Particle size and size distribution of MNPs were studied by transmission electron microscopy (TEM) (Jeol).

The systems prepared by this way were investigated by electro-optical method. The intensity of light scattered magnetite nanoparticles suspended in water is

high and considerably increases with aggregate formation. Electro-optical effects in such systems are related to the peculiarities of light scattered by the particles and are caused by anisotropy induced in the system by the applied electric field. Orientation of particles and their aggregates in electric field influences the intensity of light scattered by the particles and thus causes alterations of the intensity of light transmitted through the suspension. If the intensity of light transmitted through the system under study changes differently for different light polarizations in electric field one calls such effect induced dichroism. The magnitude of dichroism can be defined as

$$N = \ln(J_{\perp}/J_{\parallel}), \quad (1)$$

where J_{\parallel} and J_{\perp} are the intensities of transmitted light beam polarized along and across the orienting electric field. If the system under study is monodisperse, the magnitude of dichroism is proportional to the particle orientation degree Φ :

$$N = N_0 \cdot \Phi, \quad (2)$$

where N_0 is the value of N at saturated orientation of particles in the field. Values N and N_0 in (2) are determined from the experiment using (1).

For weak particle (or aggregate) orientation at certain direction

$$\Phi = \frac{\gamma E^2}{15 k_B T}, \quad (3)$$

where E is the applied electric field strength, γ is the anisotropy polarizability of particle (or aggregate), k_B is the Boltzmann constant, T is absolute temperature. After the electric field causing particle orientation is switched off electro-optical effect can be described by

$$N = N_0 \cdot \Phi \exp(-6Dt), \quad (4)$$

where D is the rotary diffusion coefficient of a particle (or an aggregate) which depends on its size. [4]

Equations (2)-(4) are valid for diluted systems [4] (single light scattering). The studied suspensions of magnetite particles are concentrated, light attenuation is significant, and one should consider light scattering to be multiple. To verify the applicability of these relations to concentrated systems the influence of particle concentration on electro-optical effect N of polydisperse aqueous colloid of diamond at different particle concentration was studied. The average particle size in this suspension is close to 500 nm, and they scatter light strongly. We did not observe formation of aggregates in this colloid while varying particle concentration in a wide range (the turbidity of the suspension changed more than 10^2 times). It was determined that varying particle concentration significantly changes the value of N_0 , and weakly influences the shape of particle orientation degree function Φ . We concluded that relations (2)-(4) can be used for semi-qualitative analysis of electro-optical data.

A principle scheme of the electro-optical setup designed and built for these experiments [5] is presented in Fig. 1.

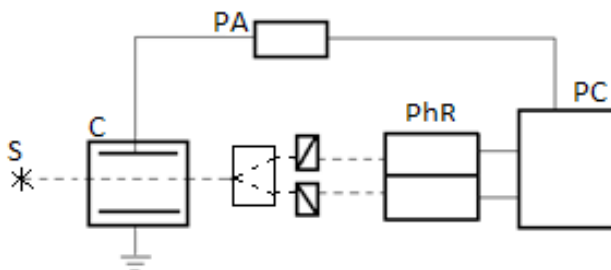


Fig. 1. Principal scheme of electro-optical setup.

Particle orientation in cell C filled with the system under study (0,6 $\mu\text{g/ml}$ of Fe) is induced by pulses of sine-shaped electric field applied to parallel electrodes, which are perpendicular to the incident light beam. Electric field pulses (with magnitude 0-250 V/cm, shape, and frequency 3-70 kHz controlled by the PC) are amplified by power amplifier PA and then are applied to the electrodes in the cell. To study concentrated systems we used a thin cell with optical path length of 4 mm, while for diluted systems where single light scattering occurred a cell with optical path length of 50 mm was used. A narrow beam of unpolarized light from source of light S, after transmitting through the cell is split into two (polarized along and across the electric field) and then measured by the photodetectors PhR. Such setup allows registering intensities J_{\parallel} and J_{\perp} of the split beams simultaneously by the PC and record the value of dichroism N (computed according to (1)), which allows to study rapidly changing systems.

For the prepared systems both the relaxation dependences $N(t)$ and stationary electro-optical effect dependence on electric field strength $N(E^2)$ were measured, which allowed to semi-quantitatively assess the particle aggregate size and electric polarizability. Experimental dependence $N(E^2)$ in the range of electric field strength up to 0.45 kV/cm was measured for all suspensions and corresponded to equation (3), with $\gamma E^2/15kT \ll 1$ and $\gamma \ll 10^{-14} \text{ cm}^3$ for all systems studied. Addition of NaCl (0.6, 1.2, 1.8 $\mu\text{g/ml}$) decreases the magnitude of dichroism and γ in water of magnetite particles coated with dextran. It agrees with the hypothesis that induced dipole moment of magnetite particles decreases in a manner similar to the decrease of induced dipole moment for other hydrophobic particles during adsorption of Na^+ ions. Increasing the frequency of applied electric field applied in the range from 3 to 70 kHz decreases value of γ . It indicates the influence of diffuse part of the double electric layer of magnetite particle on induced dipole moment magnitude.

Electro-optical effect relaxation curves $N(t)$ for SPION suspension and suspension of SPIONs conjugated with Hsp70 are presented in Fig. 2.

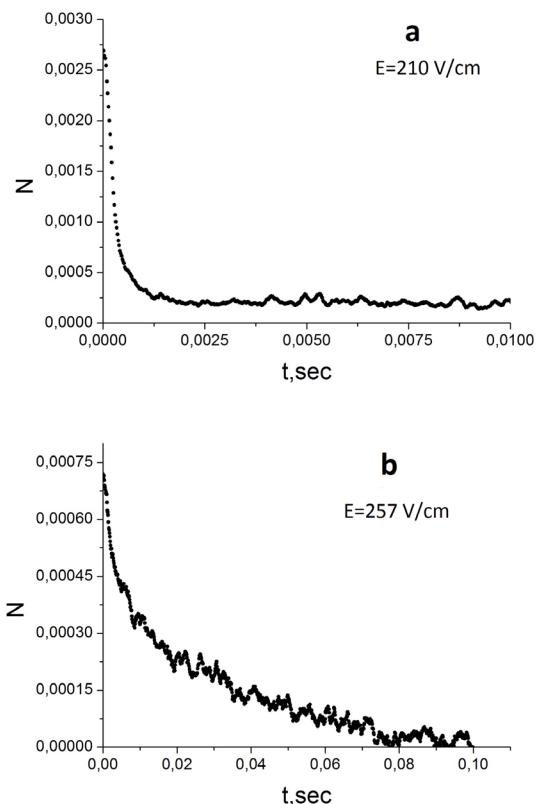


Fig. 2. Relaxation curves of electro-optical effect in SPION suspension (a) and suspension of SPIONs conjugated with Hsp70 (b).

A poly-exponential dependence, with characteristic relaxation time ranging from 1 to 100 μs for aqueous suspension of magnetite particles coated with dextran is presented in Fig. 2a. Using equation (4) we assessed from this experimental data that a considerable part of particles is not aggregated, with size 10-12 nm, but there also are aggregates with size 40-50 nm. As one can see in Fig. 2b the suspension with conjugated Hsp70 has narrower distribution of relaxation times then the suspension without Hsp70. Relaxation time of the electro-optical effect for such system increased to $5 \cdot 10^{-2} \text{ s}$, thus almost all particles in the suspension are aggregated, with aggregate size order of magnitude bigger than the size of individual particles. The observed dichroism also was considerably bigger, and the orientation order of scattering aggregates was also higher for comparable field strengths then that observed in pure SPION suspension. As the size of the aggregates grows, the value of polarizability anisotropy of aggregates grows as well.

Conclusion

Electro-optical study of SPION aqueous suspensions can be used to determine the processes of particle aggregation. These suspensions have observable dichroism in electric fields. Dichroism magnitude in electric field and its relaxation depend on the presence of Hsp70 on the surface of SPIONs.

Acknowledgements

The work was supported by a research grant 11.38.267.2014 of Saint-Petersburg State University.

References

1. Hayashi K. et al. // *Theranostics* V.3, pp. 366-376 (2013).
2. Le Renard P.E. et al. // *Int. J. Hyperthermia*, pp. 229-39 (2009).
3. Shevtsov M. et al. // *Neuro-Oncology* 16(1), pp. 38-49 (2014).
4. Spartakov A.A. et al. // *Molecular and Colloid Electro-Optics* Chap.7, pp. 193-227 (2006).
5. Trusov A. et al., CRC Press, Boca Raton (1993).

IR-investigation of DNA films

Shulenina Olga, Paston Sofia
leka-helga@yandex.ru

Scientific supervisor: Dr. Paston S.V., Department of Molecular Biophysics, Faculty of Physics, St. Petersburg State University

Introduction

Role of water molecules in the DNA environment is very important. Water interacts with soluted molecules. Just water stabilizes secondary and tertiary DNA-structures. It is possible due to its high permittivity, hydration of counterions, decreasing the electrostatic repulsion of phosphate groups and due to the hydrophobic interactions. Degree of the DNA hydration defines conformation of the macromolecule. At the high relative humidity B-form realizes. Decrease of humidity leads to the B-A transition (or B-C depending on DNA type). That transition may be caused by increasing of salt content [1].

The DNA hydration (G) is the number of water molecules per nucleotide. DNA is a polyelectrolyte, and it is highly strong and irregular hydrated. Around the DNA there are two discrete layers of water — primary and secondary hydration shells. Primary hydration shell consists of 11-12 water molecules per nucleotide (in B-form). Water binds with phosphate groups, phosphodiester bonds and with bases. At that phosphate groups are hydrated even by humidity less than 65% (5-6 water molecules per nucleotide) [1, 2].

Fig. 1 [2] shows, that at the relative humidity higher than 80% the primary hydration shell fills with water, $G=20$ and DNA is in the B-form. When G is larger than 20, a saturation effect appears and amount of B-DNA is no longer proportional to G . DNA helices remain in the B-form.

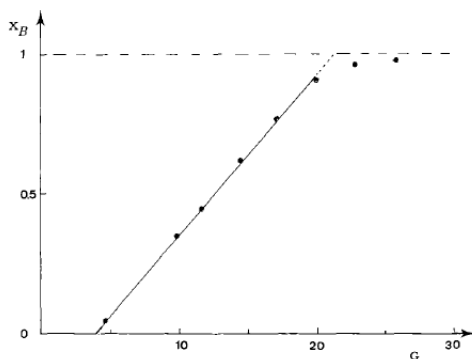


Fig. 1. A-B transition: fraction X_B of nucleotides in the B form versus DNA hydration G [2].

Until $G=20$ (that corresponds to part of B-DNA 92%) linear variations of B-DNA amount are observed. By decreasing of the relative humidity or by rising of

counterions concentration the degree of DNA hydration becomes less and when $G < 20$ the B-A transitions occur. The linear part of the curve intersects the horizontal axis at $G=4$. This value represents the number of water molecules per nucleotide in the A-form. Between these two extreme values of G we have the fraction of B- and A- DNA [1, 2]. The aim of the present study is to observe the changes in DNA hydration and structure during the DNA water-salt solution drop drying.

Results and Discussion

In our experiment we obtained dry DNA-sodium chloride films. In the present study we used chicken erythrocyte DNA. We placed a drop of a sample on the surface of IR-spectrometer diamond (Fig. 2). The drop was dried by pure dry air flow. In this method the attenuated total reflection is applied [7].

We wanted to observe the dynamics of drop drying. Each spectrum was collected during 13 seconds. In the Fig. 3 the dynamics of DNA-NaCl drop drying is shown. In the upper spectrum one can see only water vibrations. Bands, arising due to water deformational vibrations disappear during the drying and bands assigned with valent vibrations in DNA molecule remain. Intensity and form of the wide water band in region $3165\text{--}3400\text{ cm}^{-1}$ change. This band is in particular due to symmetrical and antisymmetrical stretching of O-H groups. Also in this region there are bands due to symmetrical and antisymmetrical stretching of NH_2 - and NH -groups in nitrogenous bases. Intensity and form of spectrum in this region change by decrease of total amount of O-H groups and alterations in ratio of bounded and unbounded water molecules.

During the experiment the humidity of each sample decreased. It is natural that in spectra we observe evidences of B-A transition in DNA (Fig. 4). B-A transition is accompanied by conformational changing of deoxyribose from 2-endo to 3-endo. Distance between neighbour phosphate groups and bases decreases. All that changes tell upon IR spectra. There are well known indicative alterations confirming the transition [2-6]: the blue-shifts (PO_2^-) from 1220 cm^{-1} to 1240 cm^{-1} , the intensity changes of band $1086\text{--}1096\text{ cm}^{-1}$ (PO_2^-), changes in form of peaks 1695 cm^{-1} , 1605 cm^{-1} (C=O bases groups). All spectra are related to the band 963 cm^{-1} , which is used as internal reference. This band is assigned to the deoxyribose-phosphate vibrations and exhibited no significant spectral changes during the experiment.

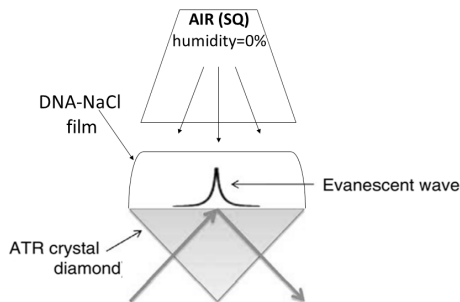


Fig. 2. Schema of the research facility ([7],

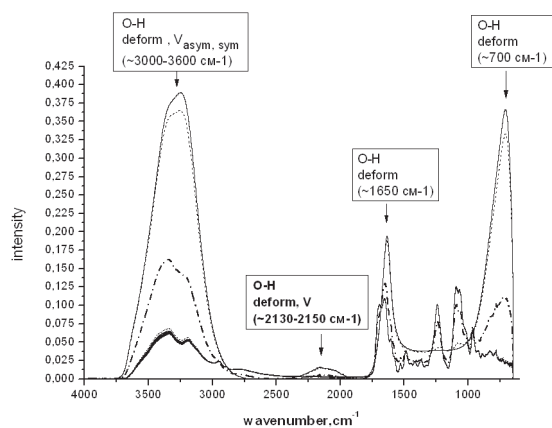


Fig. 3. Dynamics of IR spectra during the DNA-NaCl drop drying.

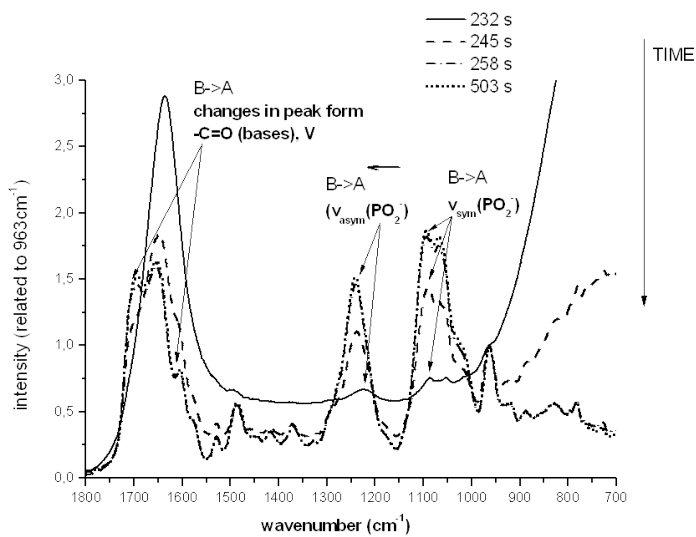


Fig. 4. Indications of B-A transition in DNA.

In the Fig. 5 the intensity changes of band 3353 cm^{-1} in films with different contents of sodium ions are demonstrated. Amount of associated water in a sample can be estimated by intensity of the band. Analysis of the spectra showed that all films have only associated water by the end. Time of full dehydration process and water amount in a sample depend on content of sodium ions. The higher sodium ions content in a film, the longer the ultimate period of drying and the less water amount in an entirely dried sample. Enrichment effect is observed — a minimal amount of water in a film achieves (Fig. 5).

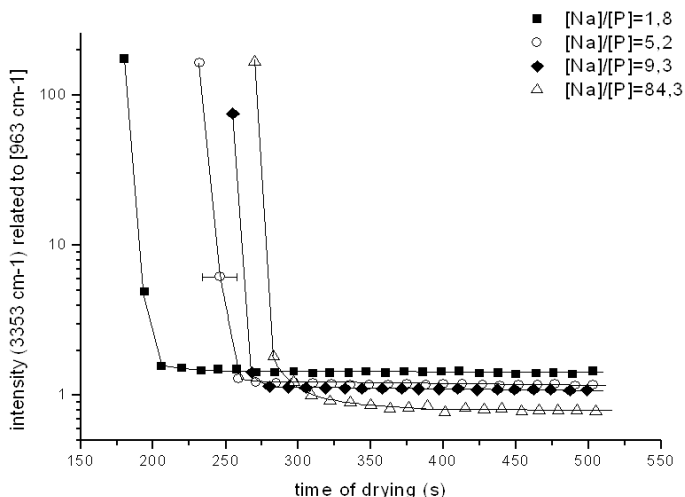


Fig. 5. IR spectra intensity changes in films with different contents of Na ions.

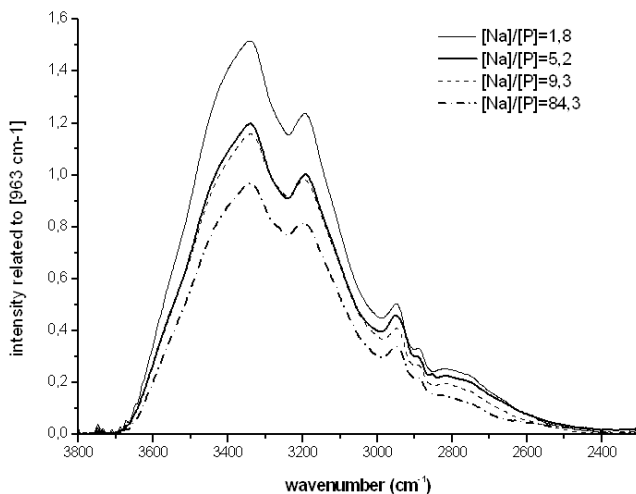


Fig. 6. IR spectra of dry films with different ratio $[Na]/[P]$.

In the Fig. 6 there are spectra of dry films at relative humidity 0%. The intensity of the line around 3335 cm^{-1} decreases with salt content increasing. It shows decreasing of bonded water amount. This fact can be explained by DNA hydration shell destruction by ions. Obtained results confirm with literature data about changes in DNA hydration shell at high contents of metal ions [8].

Conclusions

We can make the following conclusions:

α) We studied the dynamics of DNA solution drop drying and observed well known indicative alterations in IR DNA spectra confirming B-A transition during the film dehydration.

β) The higher sodium ions content in a film, the longer the ultimate period of drying and the less water amount in an entirely dried sample.

χ) The intensity of line around 3353 cm^{-1} decreases with salt content increasing. It shows decreasing of bonded water amount. This fact can be explained by DNA hydration shell destruction by ions.

Acknowledgments

Scientific research were performed at the Center for Optical and Laser Materials Research of Research park of St.Petersburg State University. This work is supported by the Russian Foundation for Basic Research (project No 13-03-01192) and SPbGU (11.38.644.2013).

References

1. Saenger W. Principles of nucleic acid structure. - Springer Verlag, 1984.
2. Harmouchi M., Albiser G., Premilat S. // European Biophysics Journal, 1990, 19, P. 87-92.
3. Hollas J.M. Modern spectroscopy.- John Wiley & Sons, Ltd.
4. Whelan D.R., Thomas J.H., Julian I.R., Keith R.B., McNaughton D., Bayden R.W. // Journal of the royal society, 2014. Interface 11: 20140454.
5. Banyay M., Sarkar M., Graeslund A. // Biophysical Chemistry, 2003. — 104. — P. 477–488.
6. Jijina G.P., Oleynic E.F. // Russian Chemical Reviews, 1972. T. XLI 3. P. 474-500. (in Russian).
7. Baker M.J., Trevisan J., Bassan P., Bhargava R., Butler H.J and other. // Nature Protocols, 2014, 9, 8, P. 1771-1791.
8. Frisman E.V., Kasyanenko N.A. // Molecular biology, 1990. T.24, 2. P. 318-326. (in Russian).

Thermodynamics of the interaction of DNA molecule with papaverine analogue containing indole substitute

Travkina Veronika, Osinnikova Daria
travkinaveronika@gmail.com

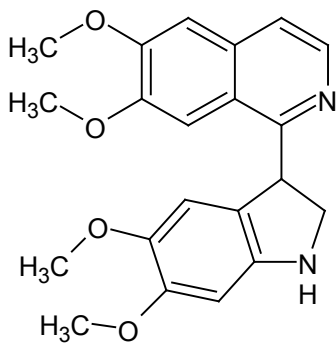
Scientific supervisor: Dr. Moroshkina E.B., Department of Molecular Biophysics, Faculty of Physics, Saint-Petersburg State University

Knowledge of the thermodynamic parameters of the equilibrium DNA complexes with various low molecular weight biological active compounds is necessary for development of new drugs whose mechanism of action is associated with the formation of equilibrium complexes. The main methods of determination the thermodynamic binding parameters, such as the binding constant and the number

of binding sites, are spectrophotometry [1] and microcalorimetry [2]. However, standard methods of titration used in both cases are different, which may affect the results.

In this work the interaction of DNA with the isoquinoline derivative having indole substitute in the first position (Fig. 1), which is similar to the well-known drug papaverine, was studied by the methods of spectrophotometry, microcalorimetry and circular dichroism.

Fig.1. The structure of isoquinoline derivative with indole substitute in the first position.



Materials and Methods

High-molecular-weight calf thymus DNA produced by "Sigma" (USA) has been used. The concentration of DNA was defined by the method of Spirin [3]. Extinction coefficient $\varepsilon_{260} = 6400\text{--}6700 \text{ M}^{-1}\text{cm}^{-1}$. The compounds were synthesized in the Research Institute of Hygiene, Occupational Pathology and Human Ecology FMBA of Russia [4]. The complexes were prepared by mixing the DNA and ligand solutions of the necessary concentrations. The ionic strength of the solution (μ) was 0,001 M and subsequently remained unchanged.

The absorption spectra were measured by the double-beam recording spectrophotometer "Specord UV VIS" and the double-beam spectrophotometer with the splitting of beams "Shimadzu UV-1800". The dichrograph from company Jobin, Yvon Mark-4 was used to receive the spectra of the circular dichroism. The calorimetric data were received from the titration microcalorimeter TA Instruments Nano ITC 2G at Thermogravimetric and Calorimetric Research Centre St. Petersburg State University.

Results and Discussion

The Fig. 2 shows the curves of spectrophotometric titration (SPT) which was made in the region of the ratios of concentrations ligand to DNA ($C_{\text{ligand}}/C_{\text{DNA}}$) from 0,01 to 3,6. We can separate these spectra to the two groups. Each group has its own isosbestic point and we conclude that this ligand interacts with DNA by the two modes. The first group of the spectra including the spectrum of free ligand (Fig. 2, curve 1) corresponds to the condition $C_{\text{ligand}}/C_{\text{DNA}} > 0,8$. In this region it is the equilibrium between free and bound ligand, it allows us to plot the binding curves of the ligand and DNA (Fig. 3, curve 1). The second group of the spectra agrees $0,1 < C_{\text{ligand}}/C_{\text{DNA}} < 0,8$. It includes the limit spectrum (Fig. 2, curve 2) which doesn't change with further rising of DNA concentration. We can assume that the free

ligand absents under this conditions and it is observed the equilibrium between two different ways of the interaction [5].

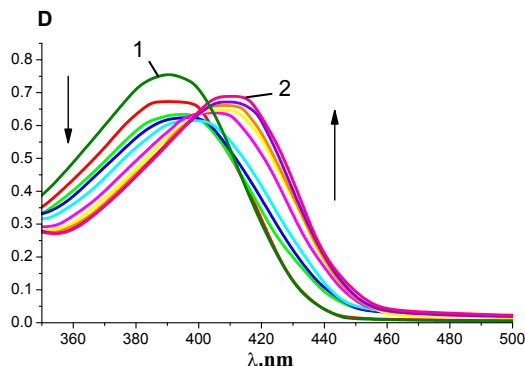


Fig. 2. The absorption spectra. $C_{\text{ligand}} = 1,93 \mu\text{M}$. $5 \cdot 10^{-6} \text{M} < C_{\text{DNA}} < 1,3 \cdot 10^{-4} \text{M}$. The spectrum of free ligand (1), the limit spectrum (2).

It allows us to plot the dependence of the ligand binds by the primarily way from the total amount of the bound ligand (Fig. 3, curve 2). This plot shows that the binding curves are the same until $C_{\text{ligand}}/C_{\text{DNA}} = 0,2$. It means the binding occurs only by the first way in this region. The extinction coefficient of compound equals $\epsilon_{416} = (7400 \pm 300) \text{M}^{-1}\text{sm}^{-1}$.

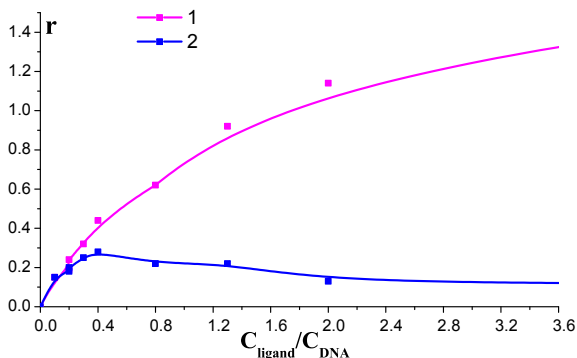


Fig. 3. The dependences of totally binding ligand (1) and ligand binds by the primary mode (2) from $C_{\text{ligand}}/C_{\text{DNA}}$.

The circular dichroism spectroscopic titration was carried out at constant concentration of DNA (Fig. 4). The investigated compound

doesn't have an optical activity. The induced circular dichroism (ICD) of exciton type appears at $C_{\text{ligand}}/C_{\text{DNA}} > 0.5$, this agrees to the secondarily bound ligand.

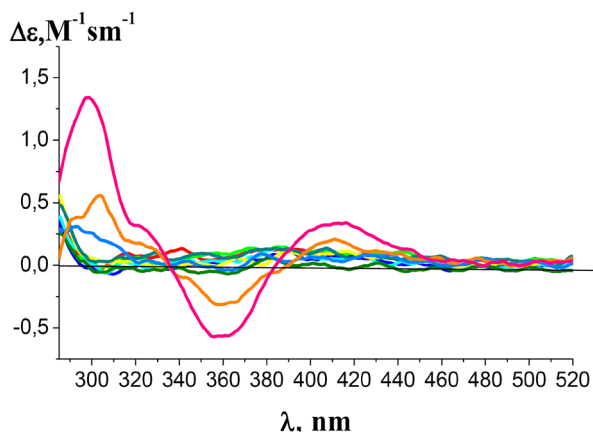


Fig. 4. The spectrum of circular dichroism. $C_{\text{DNA}} = 2 \cdot 10^{-5} \text{ M}$.

The result of isothermal titration calorimetry (ITC) in the wide range of $C_{\text{ligand}}/C_{\text{DNA}}$ is shown in figure 5. As in the case of SPT, in the resulting thermogram we can distinguish two regions of concentration ratios in which the different nature

of the binding enthalpy's change are observed: the region of the increasing enthalpy at $0.1 < C_{\text{ligand}}/C_{\text{DNA}} < 0.8$ and the region of the decreasing enthalpy ($C_{\text{ligand}}/C_{\text{DNA}} > 0.8$).

The comparison of the ITC results with the SPT results allows us to make the following conclusions: 1) the lack of monotony in the enthalpy change is caused by the existence of two binding modes of the ligand with DNA; 2) the increase of the enthalpy at $0.2 < C_{\text{ligand}}/C_{\text{DNA}} < 0.8$ is due to the appearance and the increase of the amount of the compound interacting with DNA by the secondary way; 3) at the range of $C_{\text{ligand}}/C_{\text{DNA}} < 0.8$ the free ligand almost absents, this allows to obtain the binding enthalpy directly from the experimental data [6]; 4) the decrease of the enthalpy

is due to saturation of the macromolecule by the ligand and the appearance of the free ligand in the solution with a further increase of $C_{\text{ligand}}/C_{\text{DNA}}$.

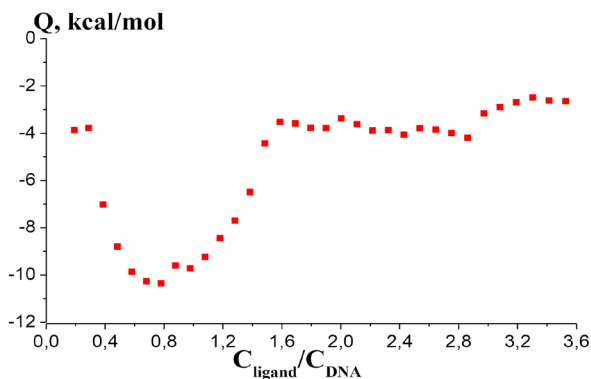


Fig. 5. The ITC thermogram. $C_{\text{DNA}} = 2 \cdot 10^{-5} \text{ M}$.

The ITC experiment at $C_{\text{DNA}} = 2 \cdot 10^{-4} \text{ M}$ was carried out for the determining the binding enthalpy of the first binding mode (Fig.6).

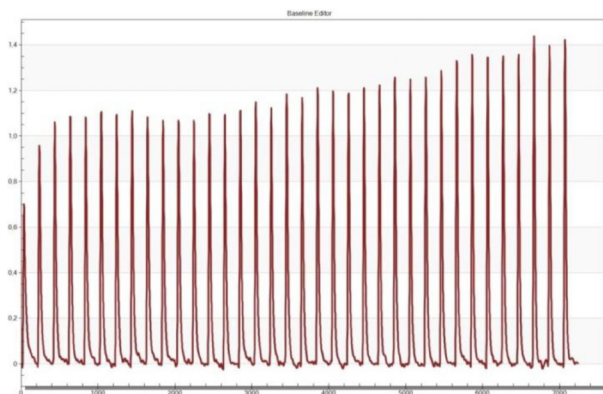


Fig. 6. The ITC data.

The use of model-free method of calculation for this way of interaction gives $\Delta H = (-4,0 \pm 0,5)$ kcal/mol. In the range of $C_{\text{ligand}}/C_{\text{DNA}}$ the binding of the ligand goes

only by the second way. The use of model-free method of calculation for this way of interaction gives $\Delta H = (-10,5 \pm 0,5)$ kcal/mol.

Conclusion

Under the experimental conditions the investigated compound binds to DNA in the two ways. The compound bound by the first way at low degree of saturation doesn't have the optical activity. The extinction coefficient of compound equals $\varepsilon_{416} = (7400 \pm 300) \text{ M}^{-1}\text{sm}^{-1}$. The binding enthalpy of this way of interaction equals $\Delta H = (-4,0 \pm 0,5)$ kcal/mol. The second binding mode appears at $C_{\text{ligand}}/C_{\text{DNA}} > 0,2$. This kind of interaction causes the ICD of exciton type. The binding enthalpy of the secondary way of interaction equals $\Delta H = (-10,5 \pm 0,5)$ kcal/mol. We can assume that the ligand bound by the secondary way forms the dimers at the surface of DNA. The binding constants of interaction of the compound with DNA by the both ways are large enough ($> 10^6 \text{ M}^{-1}$) and they can't be determined by the SPT and the ITC methods.

References

1. Moroshkina E.B., Bogdanov A.A., Kolonistova M.O. et al. // Journal of Structural Chemistry, 2009, 50 (5), pp. 989-995.
2. Puja Paul, Maidul Hossain, Gopinatha Suresh Kumar // J. Chem. Thermodynamics, 2011, 43, pp. 1036-1043.
3. Спирин А.С. // Биохимия, 1981, 23, с. 656-662.
4. Krivorotov D.V., Vorob'ev M.V., Polukeev V.A., Glibin E.N. // J. Organic Chemistry (Rus), 2006, 42, pp. 594-596.
5. Krivtsova M.A., Moroshkina E.B., Glibin E.N. et al. // Molecular Biology, 1982, 16 (1), pp. 121-126.
6. Kenneth J. Breslauer, Ernesto Freire and Martin Straume // Methods in enzymology, 1992, 211, pp. 533-567.

I. Resonance Phenomena in Condensed Matter

The hydration layer around the B1 domain of immunoglobulin-binding protein L. A molecular dynamics simulation study

Krylova Ekaterina
krylovaea2803@mail.ru

Scientific supervisor: Dr. Egorov A.V., Faculty of Physics, Saint-Petersburg State University

Introduction

Understanding the properties of water in biological system is a problem of fundamental interest in chemistry and biology. The water-protein interaction is a major determinant of protein folding and conformational stability [1, 2].

In the present study the structure of the hydration layer that surrounds the B1 domain of immunoglobulin-binding protein L (Protein Data Bank code 1HZ6 [3], protein sequence is shown in Fig. 1) as well as the dynamics of water molecules in the layer has been examined using molecular dynamics computer simulations.

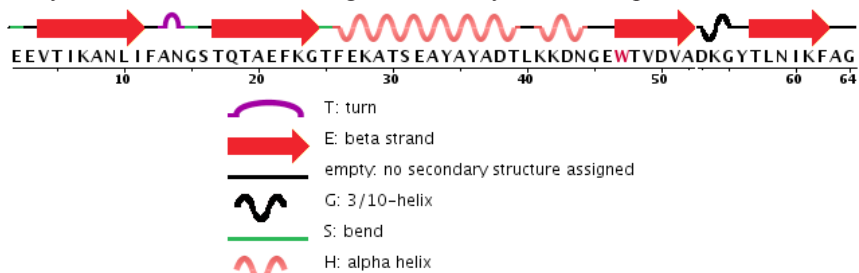


Fig. 1. Sequence of the B1 domain of immunoglobulin-binding protein L from Protein Data Bank [4].

Molecular Dynamics simulations details

A model solution of 1 protein molecule (963 atoms) among 7404 water molecules was considered. Simulations were carried out in an isothermal-isobaric ensemble in a cubic periodic cell at 1 atm and 25°C using the *MDynaMix* package [5]. To describe water molecules the SPC/E model [6] was employed. To describe water interactions with the protein molecule the force field proposed by Cornell et al. [7] was used. The temperature was kept constant by using the Nose-Hoover thermostat [8] and pressure was regulated by the Hoover barostat [9]. The equations of motion were solved using the Verlet algorithm [10] with a time step of 2.0 fs. The Coulomb interactions were calculated using the Ewald summation method [10]. The SHAKE procedure [11] was employed to constrain all the bond lengths. The system was equilibrated during a 30 ps run. Further, a 100 ps simulation run was performed.

Results and conclusions

Radial distribution functions, $g(r)$, contain the most basic information about the solution microstructure. To describe the water structure in the vicinity of the protein surface radial distribution functions (RDFs) between three atom pairs: hydrogen atom of amino group (HN) – oxygen atom of water molecule (Ow), hydrogen atom attached to alpha carbon (HA) – oxygen atom of water molecule, and oxygen atom of carboxyl group (Oc) – oxygen atom of water molecule, were calculated for every protein residue. The positions of the first maximum of corresponding RDFs are given in Table 1. Eight types of distributions were observed. Fig. 2 represents the case of non-hydrated residue then water molecules do not come close to the residue surface. Figs. 3-4 represent the examples of partly hydrated residue then water comes close to alpha-carbon group only (Fig. 3) or both to alpha-carbon and carboxyl groups (Fig. 4). Fig. 5 represents the RDFs for completely hydrated residue.

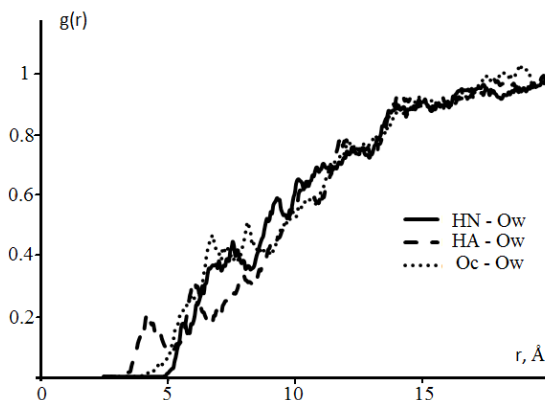


Fig. 2. RDFs between HN-Ow, HA-Ow, and Oc-Ow atom pairs. Residue 6.

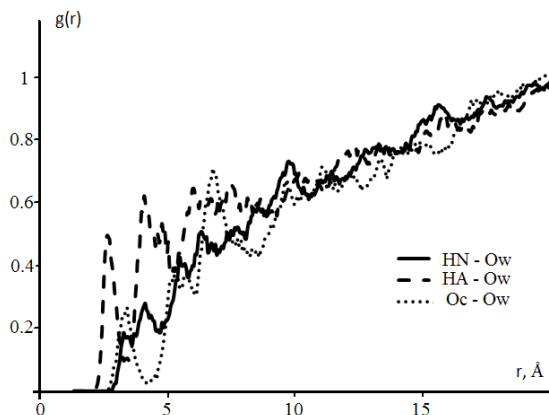


Fig. 3. RDFs between HN-Ow, HA-Ow, and Oc-Ow atom pairs. Residue 32.

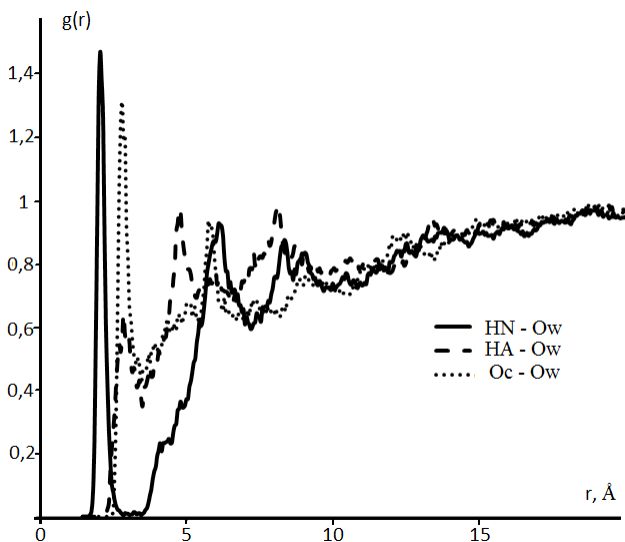


Fig. 4. RDFs between HN-Ow, HA-Ow, and Oc-Ow atom pairs. Residue 63.

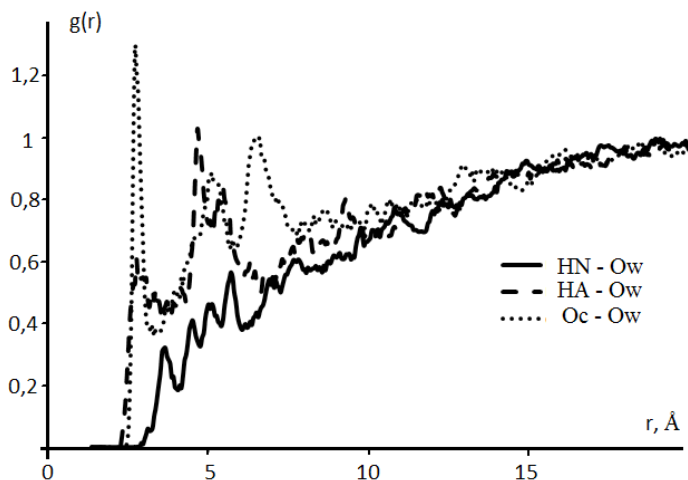


Fig. 5. RDFs between HN-Ow, HA-Ow, and Oc-Ow atom pairs. Residue 43.

According to simulations results 23 residues (about 37%) are not hydrated at all. For the rest of residues the thickness of the protein hydration layer varies from 2.7 Å in the vicinity of amino group to 3.5 Å near alpha-carbon or carboxyl groups.

To describe water dynamics the residence times of water molecules in the protein hydration layer were calculated following the standard procedure described in [12]. The results are collected in Table 1.

Table 1. Residence times of water molecules in the protein hydration layer. The non-hydrated residues are not included.

Secondary structure	Residue	Type of water environment					
		HN – Ow		HA - Ow		Oc - Ow	
		r(Å)	τ_{res} (ps)	r(Å)	τ_{res} (ps)	r(Å)	τ_{res} (ps)
	3	-	-	-	-	2.725	8.93
β -strand	5	2.025	9.54	-	-	-	-
	12	-	-	-	-	2.675	8.19
turn	13	1.925	39.35	-	-	2.725	4.29
	14	-	-	-	-	2.775	4.92
	15	-	-	-	-	2.775	6.50
	16	-	-	-	-	2.725	26.89
β -strand	17	2.075	5.37	-	-	2.725	6.60
	18	-	-	-	-	2.725	14.42
	19	1.975	7.39	-	-	2.675	5.91
	20	-	-	2.725	5.62	-	-
	21	1.975	4.45	-	-	2.675	5.71
	22	-	-	2.725	6.96	-	-
	23	1.975	5.35	-	-	2.725	6.90
	25	2.075	38.64	2.875	8.85	-	-
	26	1.975	5.28	-	-	-	-
	27	1.975	57.37	-	-	-	-
	28	-	-	2.725	12.70	-	-
	32	-	-	2.625	7.40	-	-
	36	-	-	3.025	9.32	-	-
	38	-	-	-	-	2.725	5.27
α -helix	39	-	-	-	-	2.725	8.62
	40	-	-	2.575	15.48	-	-
	42	2.075	3.25	-	-	2.725	7.20
	43	2.075	55.56	2.825	4.21	2.775	4.73
	44	-	-	2.725	7.20	2.825	7.28
	46	1.975	23.61	3.025	38.54	2.775	17.88
	47	-	-	-	-	2.775	12.60
β -strand	48	-	-	2.825	9.20	-	-
	49	1.875	20.28	-	-	2.825	7.50
	50	-	-	2.675	9.04	-	-
	51	1.825	12.94	-	-	2.825	5.8
	52	-	-	2.825	7.09	-	-
	53	2.075	5.08	2.825	7.37	2.725	13.83
3/10 helix	54	-	-	-	-	2.725	7.35
	55	-	-	-	-	2.725	117.96
	61	-	-	-	-	2.725	8.04
β -strand	62	-	-	-	-	2.725	6.65
	63	-	-	2.725	6.17	2.675	5.46
	64	-	-	3.025	7.64	-	-

References

1. B. Bagchi // Chem. Rev., 105, 3197-3219 (2005).
2. B. Halle // Phil. Trans. R. Soc. Lond. B, 359, 1207-1224 (2004).
3. J.W. O'Neill, D.E. Kim, D. Baker, K.Y.J. Zhang // Acta Cryst. D, 57, 480-487 (2001).

4. www.rcsb.org
5. A.P. Lyubartsev, A. Laaksonen // *Comp. Phys. Comm.*, 128, 565-589 (2000).
6. H.J.C. Berendsen, J.R. Grigera, T.P. Straatsma // *J. Phys. Chem.*, 91, 6269-6271 (1987).
7. W.D. Cornell, P. Cieplak, C.I. Bayly, et al. // *J. Am. Chem. Soc.*, 117, 5179-5197 (1995).
8. S. Nose // *Mol. Phys.*, 52, 255-268 (1984).
9. G.J. Martyna, D.J. Tobias, M.L. Klein // *J. Chem. Phys.*, 101, 4177-4189 (1994).
10. M.P. Allen, D.J. Tildesley, *Computer Simulation of Liquids*, Clarendon Press, Oxford, 1986.
11. J.P. Ryckaert, G. Ciccotti, H.J.C. Berendsen // *J. Comp. Phys.*, 23, 327-341 (1977).
12. R.W. Impey, P.A. Madden, I.R. McDonald // *J. Phys. Chem.*, 87, 5071-5083 (1983).

Exchange reactions of hydrogen isotopes below 1K

Sheludiakov Sergei
seshel@utu.fi

*Scientific supervisor: Dr. Vasiliev S.A., Department of Physics and
Astronomy, University of Turku, Finland*

Introduction

Solid hydrogen and deuterium constitute a special type of so-called quantum crystals where due to a large zero-point energy tunneling effects play an important role in the translational motion of particles. Light atomic impurities like H or D introduced into such matrices are able to migrate from one lattice site to another by repetition of exchange tunneling reactions, $H_2+H=H+H_2$ and $D_2+D=D+D_2$ [1]. They travel through the crystal until they finally recombine with another H or D atom. Similar exchange reactions, $H_2+D=H+HD$ and $HD+D=H+D_2$, involving both hydrogen isotopes can also take place in mixtures of H_2 and D_2 . They were first time observed by Gordon et al [2]. Authors detected a high-rate conversion of D atoms into H in a solid mixture of H_2 and D_2 at temperature of 1.8 K using Electron-spin resonance (ESR).

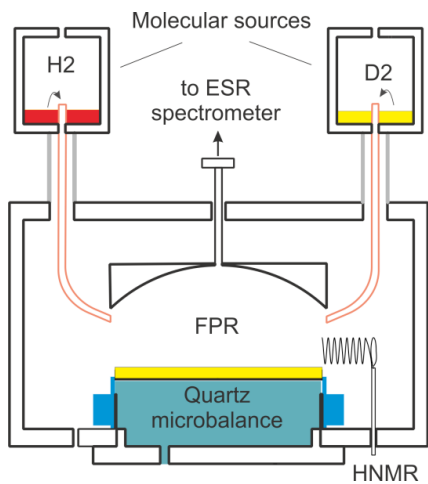
The exchange reactions of hydrogen isotopes have activation energies of about 4600 K and proceed at low temperatures exceptionally via tunneling. It is known that impurities or other crystal irregularities may violate the resonant tunneling mechanism [3]. This diminishes the tunneling probabilities and dramatically reduces the efficiency of the exchange reactions. Therefore it is predicted that H and D atoms should be very stable at densities of the order of $10^{20}cm^{-3}$ [4].

In a present work we report on the first experimental observation of the isotopic exchange reactions in solid D_2 films with a small admixture (about 1%) of H_2 and HD at temperatures far below 1 K. Efficient conversion of D atoms into H was observed in the course of measurement. This resulted in creating high densities of H atoms which remained peculiarly stable towards recombination up to temperatures of a few Kelvin where the film sublimation became a major factor of losing the signal.

Experimental Setup

Experiments were performed in the sample cell (SC) shown in Fig. 1 [5]. It contains a 128 GHz Fabry-Perot type ESR resonator and two molecular sources for performing H_2 and/or D_2 coating. The SC is thermally anchored to the mixing chamber of an Oxford 2000 dilution refrigerator and situated at the center of a 4.6 T superconducting magnet. The main methods of investigation are Electron-spin resonance and mass measurement by a quartz-crystal microbalance (QM) which also plays a role of a flat mirror of the ESR resonator.

The open design of the FPR provides an opportunity to arrange a miniature helical resonator near the QM without distorting the mm-wave field in the ESR



cavity. The helical resonator (HNMR) was tuned to 910 MHz and used for exciting an NMR transition of the H atoms. Moreover, it was also utilized to run rf discharge in the SC for dissociating a fraction of H_2 and D_2 molecules in the film into atoms by electron impact.

The samples were created in two stages. First a D_2 film was deposited onto the QM which was kept below 1 K to assure smooth and homogeneous hydrogen coating [6]. Then rf discharge was activated in the sample cell to accumulate unpaired H and D atoms in the film.

Fig. 1. Schematic drawing of the sample cell.

Results and Discussion

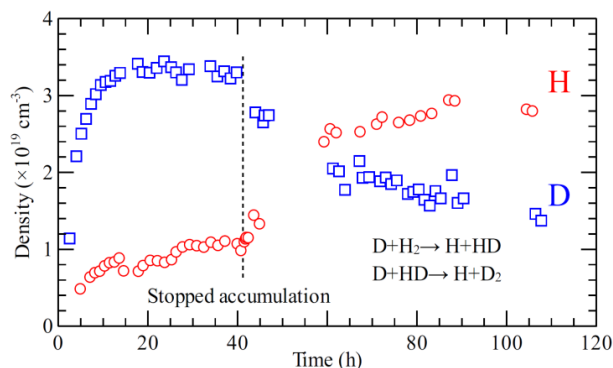


Fig. 2. Evolution of atomic hydrogen and deuterium densities, recorded during the RF dissociation and subsequent exchange reactions at $T=300$ mK.

The dissociation probability is equal for D_2 , H_2 and HD. This means that about 99% of H atoms were created in the course of the exchange reactions.

An increase of H densities and decrease of D densities after stopping the accumulation clearly identifies the isotopic exchange reactions. The steady state concentrations of H and D of $3 \cdot 10^{19} \text{ cm}^{-3}$ and $1.4 \cdot 10^{19} \text{ cm}^{-3}$, respectively, were reached after time period of 120 hours. We found that the isotopic exchange reactions proceed with a high enough rate down to temperatures of 80 mK which is a limit for our dilution refrigerator. Unfortunately we were unable to estimate the reactions' rates due to uncertainty in the H_2 and HD content in our film.

The following studies showed that H atoms produced in the exchange reactions remained very stable towards recombination in a wide temperature range. It can be explained by the fact that the H atoms created from conversion of D atoms

Accumulation was run for several hours for reaching the highest densities of D atoms, about $3 \cdot 10^{19} \text{ cm}^{-3}$ (Fig. 2). Afterwards the discharge was stopped and the sample cell temperature was stabilized at 300 mK. The H concentration obtained during accumulation is spectacularly large assuming that the dis-

become immobilized by a D_2 surrounding [2]. The reverse exchange reaction, $H+D_2=D+HD$, involving H and D_2 is slightly endothermic (about 500 K) due to the difference in the zero-point energies of the reactants and products and cannot proceed at low temperatures.

The sample stability at 300 mK during 2 weeks of measurement is shown in Fig. 3. The recombination remained vanishingly small for both H and D atoms at this temperature. Such behavior is in a

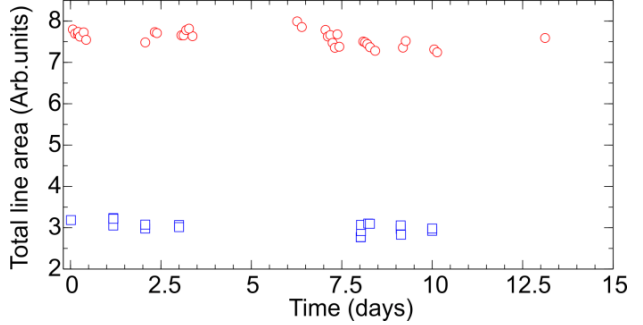


Fig. 3. H (circles) and D (squares) atom stability at temperature of 300 mK.

big contrast to a regular H in H_2 samples [7] of the same H atom density.

High stability of H atoms was also observed at higher temperatures. The recombination of H atoms in H_2 or D_2 solids is known to be a two-body process and can be described by a second order kinetic equation.

$$\frac{dn}{dt} = -2K_r n^2$$

Hence an inverse density, n^{-1} , should have a linear dependence on time with a slope of twice the recombination constant, $2 K_r$. The H atom decay in a temperature range of 1-2.5 K is shown in Fig. 4. The recombination is almost temperature independent within this range unlike

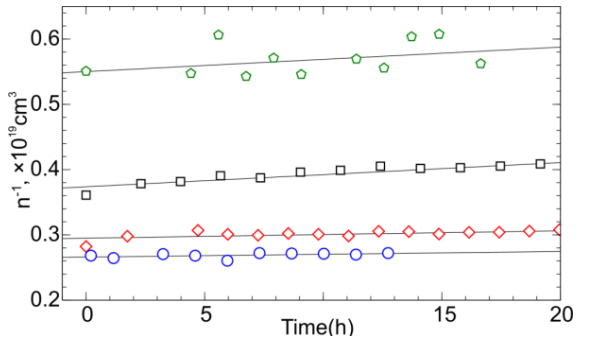


Fig. 4. Time evolution of inverse density of H atoms at different temperatures: rounds-1K, diamonds-1.5 K, squares-2 K, pentagons-2.5 K.

for H atoms in H_2 . An estimate of the recombination constant for H in D_2 at 1 K gives K_r of $2 \cdot 10^{-30} \text{ cm}^3/\text{s}$ which is about 6 orders of magnitude smaller than that for H in H_2 ($2 \cdot 10^{-24} \text{ cm}^3/\text{s}$) measured by Ahokas et al [7]. It is also worth to emphasize that the ratio between H and D atoms was $7:3 \pm 20\%$ during recombination at temperatures up to 4K. This allows us to conclude that the loss rate for D atoms was about 50% smaller than that for H atoms. There are two possible sources of losing D atoms, namely their recombination and the exchange reaction with the remnants of HD and H_2 which converts them into H. If we assume that the main

source is the D-to-H conversion, the recombination constant K_r for H should be about 30% larger than the estimated value.

The sample remained stable even at temperatures higher than 2.5 K. But at these temperatures film sublimation becomes an additional factor of losing the signal.

Conclusion

The exchange reactions of hydrogen isotopes were for the first time observed at temperatures far below 1 K. We found out that these reactions efficiently convert D atoms into H at temperatures down to 80 mK which is a limit for our dilution refrigerator. The H atoms generated in the exchange reactions become localized by the D_2 surrounding which prevents their recombination in a wide temperature range.

References

1. Kumada T. // Phys. Rev. B 68, p. 052301 (2003).
2. Gordon E. B. et al.// JETP Lett. 37, pp. 282-285 (1983).
3. Kagan Yu. and Maksimov L.A. // Sov. Phys. JETP 57, pp. 459-470 (1983).
4. Webeler R.W.H.// J. Chem. Phys., 64, p. 2253 (1976).
5. Sheludiakov S. et al. // Rev. Sci. Instrum., 85, p. 053902 (2014).
6. Albrecht U. et al.// Surf. Sci. 283, p.419 (1993).
7. Ahokas J.M. et al.//Phys. Rev. B, 81, p.104516 (2010).

Table of Content

B.Geo- and Astrophysics	5
Gydra — GPU-based code for astrophysical SPH simulations <i>Korsunov Igor</i>	6
Photometry and polarimetry of supernovae performed on telescopes LX200 and AZT-8 <i>Mokrushina Anna</i>	10
Correlation of radial fluctuations in deep galaxy redshift surveys <i>Shirokov Stanislav</i>	15
C. Mathematics and Mechanics	19
Andronov-Hopf bifurcation of one or more cycles in the Mackey-Glass type delay differential equation <i>Ignatenko Vera</i>	20
Numerical probabilistic approach to solution of the Cauchy problem for quasilinear parabolic equations <i>Nemchenko Ekaterina</i>	25
Monte Carlo Simulation for Stochastic Differential Equations <i>Pogosian Anna</i>	29
Simulations of high-velocity star motions in the Galactic gravitational field <i>Shirokova Kseniia</i>	32
Caratheodory dimension of invariant sets for dynamical systems with multiple time <i>Voynov Dmitriy</i>	37
D. Solid State Physics	41
Magnetic-field induced variation of energy dispersion of exciton in CdTe <i>Bođnar Stanislav</i>	42
Direct numerical solution of Schroedinger equation for excitons in quantum wells <i>Khrantsov Evgeniy, Belov Pavel, Grigoryev Philipp</i>	46

E. Applied Physics.....	51
Research of consequences of the accidents at nuclear power plants and impact on the environment of Leningrad region	
<i>Merzlaya Anastasia.....</i>	<i>52</i>
Velocity spread in quantum hydrodynamics	
<i>Zippa Andrey</i>	<i>57</i>
G. Theoretical, Mathematical and Computational Physics	61
Special splints and their types	
<i>Kakin Polina</i>	<i>62</i>
Anomalous scaling of passive scalar fields advected by the Navier-Stokes velocity ensemble: Effects of strong compressibility and large-scale anisotropy	
<i>Kostenko Mariia.....</i>	<i>67</i>
Constraint algebra for embedding theory with partial gauge fixing	
<i>Semenova Elizaveta</i>	<i>70</i>
Dynamics of triple asteroids	
<i>Timoshenko Vladimir</i>	<i>75</i>
Sensitivity of Tunneling-Rotational Transitions in Ethylene Glycol to Variation of Electron-to-Proton Mass Ratio	
<i>Viatkina Anna.....</i>	<i>80</i>
H. Biophysics	85
Electro-optical method to study aggregation in aqueous suspensions of SPIONs and SPIONs conjugated with Hsp70	
<i>Parr Marina.....</i>	<i>86</i>
IR-investigation of DNA films	
Thermodynamics of the interaction of DNA molecule with papaverine analogue containing indole substitute	
<i>Travkina Veronika, Osinnikova Daria</i>	<i>96</i>

I. Resonance Phenomena in Condensed Matter 101

The hydration layer around the B1 domain of immunoglobulin-binding protein L.
A molecular dynamics simulation study

Krylova Ekaterina 102

Exchange reactions of hydrogen isotopes below 1K

Sheludiakov Sergei 107

